

LARGE-SCALE  
TIGHT-BINDING  
SIMULATIONS  
OF

TWO-DIMENSIONAL  
MATERIALS

AND  
SELF-SIMILAR  
SYSTEMS

EDO VAN VEEN

LARGE-SCALE TIGHT-BINDING SIMULATIONS  
OF TWO-DIMENSIONAL MATERIALS AND  
SELF-SIMILAR SYSTEMS

© Edo van Veen 2019

Large-scale tight-binding simulations of two-dimensional materials and self-similar systems

Thesis, Radboud University Nijmegen

vi + 129 pages

Illustrated, with bibliographic references and summary in Dutch

ISBN 978 · 90 · 9032246 · 9

Printed in the Netherlands by Ipskamp

This work has been financially supported by the European Research Council

LARGE-SCALE TIGHT-BINDING SIMULATIONS  
OF TWO-DIMENSIONAL MATERIALS AND  
SELF-SIMILAR SYSTEMS

PROEFSCHRIFT

ter verkrijging van de graad van doctor  
aan de Radboud Universiteit Nijmegen  
op gezag van de rector magnificus prof. dr. J.H.J.M. van Krieken,  
volgens besluit van het college van decanen  
in het openbaar te verdedigen op woensdag 23 oktober 2019  
om 12.30 uur precies

door

EDO NICOLAAS WILLEM VAN VEEN

geboren 20 februari 1990  
te Eindhoven

PROMOTOREN

Prof. dr. M.I. Katsnelson  
Prof. dr. S. Yuan  
(Wuhan University, China)

MANUSCRIPTCOMMISSIE

Prof. dr. H.M. Cuppen  
Prof. dr. T.O. Wehling  
(Universität Bremen, Duitsland)  
Prof. dr. K. Michielsen  
(RWTH Aachen, Duitsland)

# CONTENTS

<b>1</b>	<b>Introduction</b>	<b>1</b>
1.1	2D materials . . . . .	2
1.2	Quantum mechanics . . . . .	3
1.3	Computational physics . . . . .	5
1.4	Outline of this thesis . . . . .	6
<b>2</b>	<b>Models and methods</b>	<b>7</b>
2.1	Tight-binding . . . . .	8
2.2	Electronic properties . . . . .	9
2.3	Optical properties in momentum description . . . . .	10
2.4	Optical properties in real-space description . . . . .	11
2.5	Transport properties . . . . .	13
2.6	Tight-binding propagation method . . . . .	15
<b>3</b>	<b>Antimonene ribbons under bias</b>	<b>19</b>
3.1	Introduction . . . . .	20
3.2	Model and method . . . . .	22
3.3	Out-of-plane bias . . . . .	28
3.4	In-plane transverse bias . . . . .	31
3.5	Conclusion . . . . .	36
<b>4</b>	<b>Tuning 2D hyperbolic plasmons in black phosphorus</b>	<b>37</b>
4.1	Introduction . . . . .	38
4.2	Optical Conductivity and Band Model . . . . .	39
4.3	Hyperbolic Regions . . . . .	41
4.4	Hyperbolic Plasmons. . . . .	46
4.5	Conclusion . . . . .	49
<b>5</b>	<b>Quantum transport in Sierpinski carpets</b>	<b>51</b>
5.1	Introduction . . . . .	52
5.2	Method . . . . .	54

5.3	Fractal geometry . . . . .	54
5.4	Results . . . . .	60
5.5	Summary . . . . .	72
<b>6</b>	<b>Optical and plasmonic properties of Sierpinski fractals</b>	<b>73</b>
6.1	Introduction . . . . .	74
6.2	Model and methods . . . . .	75
6.3	Optical conductivity of Sierpinski carpets . . . . .	77
6.4	Plasmon confinement in fractal quantum systems . . . . .	86
6.5	Summary . . . . .	91
	<b>Appendix: Tipsi</b>	<b>93</b>
7.1	Installation . . . . .	94
7.2	Sample building . . . . .	94
7.3	Configuration . . . . .	99
7.4	Calculating and analyzing correlation functions . . . . .	100
	<b>Bibliography</b>	<b>103</b>
	<b>Summary</b>	<b>121</b>
	<b>Samenvatting</b>	<b>123</b>
	<b>Publications</b>	<b>125</b>
	<b>Curriculum Vitae</b>	<b>127</b>
	<b>Acknowledgements</b>	<b>129</b>

# CHAPTER 1

## INTRODUCTION



## 1.1 2D materials

Human prehistory is generally subdivided into three ages, defined by the material that was used to make the newest technology at the time: the Stone Age, the Bronze Age and the Iron Age. If we continue that line of thought to the present, we are arguably in the Silicon Age, because the brains of our computers and phones are made of silicon. However, over the next few decades, in the quest to make our gadgets faster, thinner and more efficient, we might enter into a new age: the 2D Material Age. Two-dimensional (2D) materials are materials with a thickness of one atom, or only a few atoms.

It is not yet clear exactly *which* 2D materials will be in our gadgets. Many of these materials have been made in laboratories, the first one being graphene in 2004 by Andre Geim and Konstantin Novoselov, who later won a Nobel prize for their research. Graphene has some amazing properties: it is extremely strong, light and flexible, and it is a great conductor for heat and electricity. Since then, other materials such as the transition metal dichalcogenides and phosphorene have been added to the list. All these materials have different electronic and optical properties.

These basic properties stem from the type of atoms that they are made of, and the geometry of the lattice formed by those atoms. For example, graphene is made of carbon atoms, and its lattice is hexagonal (see Fig. 1.1). These properties can be changed by adding electric or magnetic fields, stretching or compressing the material, or adding disorder, for example by adding other atoms onto the surface. Moreover, these materials can be grown or etched into different shapes, further changing their properties. In this thesis we will look at self-similar shapes – shapes that have repeating patterns when we zoom in or out.

We will be doing calculations on models of different 2D materials (chapters 3 and 4) and structures with self-similar shapes (chapters 5 and 6) to study how electrons behave in these materials and how they interact with light. These calculations are based on the theory of quantum mechanics.

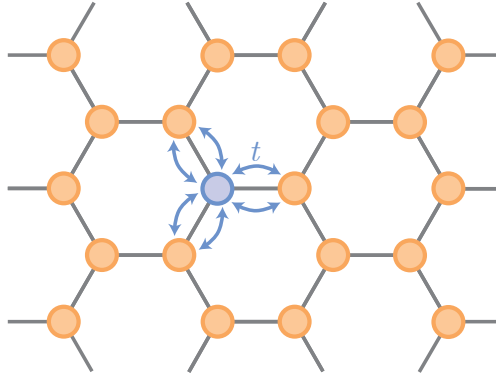


Figure 1.1: A hexagonal graphene lattice, with nearest neighbor hopping  $t$ , to and from the site indicated in blue.

## 1.2 Quantum mechanics

The theory of quantum mechanics describes matter and energy on the scale of atoms. It came about in the early 20th century, starting with Max Planck's postulate that thermal radiation is emitted in quantized energy packets. Albert Einstein then suggested that these packets can be seen as individual light particles called photons, that can be emitted or absorbed by electrons in a material. A few years later Niels Bohr proposed a model of the atom in which electrons have quantized orbits around the nucleus, and Louis de Broglie showed that these electrons can be seen as both particles and waves. This collection of ideas forms the starting point of the theory used in this thesis.

Quantum mechanics has some counterintuitive aspects that mostly have to do with probability and measurement. The state of a quantum system is defined in terms of a wave function, and the absolute square of the wave function gives us probabilities for measurement outcomes. Moreover, any measurement apparatus will interact with the quantum system, changing

its wave function and the corresponding probability distribution. Most famously, when we measure the speed of a quantum particle, its location cannot be exactly known, and vice versa. Luckily, in this thesis we will mostly look at averages over a large number of particles, and there will be no issues with measurement.

In our description of electrons roaming in a lattice of atoms the two most important quantities are the Hamiltonian  $\hat{H}$  and the wave function  $|\psi\rangle$ . The Hamiltonian describes the orbitals present within the model and the interactions between them, and the wave function describes what state the electrons are in. The behavior of electrons is dictated by the Schrödinger equation

$$i\hbar\frac{d}{dt}|\psi(t)\rangle = \hat{H}|\psi(t)\rangle, \quad (1.1)$$

where  $\hbar$  is the reduced Planck constant. If we assume that the Hamiltonian is time-independent, the time-evolution of the wave function is then given by

$$|\psi(t)\rangle = e^{-i\hat{H}t/\hbar}|\psi(0)\rangle. \quad (1.2)$$

For a full quantum description of a material we would have to include all possible interactions between electrons and atomic nuclei, electrons and other electrons, and more. This would make any calculation involving more than a handful of particles extremely complicated.

Instead, we use the tight-binding approximation. This is a simple and computationally efficient way to model solid state systems. However, it is a single-particle model: its main limitation is that we cannot include any correlation effects, i.e., interactions between different electrons. In the tight-binding approximation we assume that the electrons are “tightly bound” to the atoms in the lattice. There is only a limited interaction (“hoppings”) with the potentials on surrounding atoms in the solid. Hence the wave function of the electron is very similar to the atomic orbital of the free atom. Often, a model considering only hoppings to the nearest neighbors surrounding an atom (see Fig. 1.1) is already enough to model the important features of a material.

However, a realistic model can contain many more hoppings than just

nearest neighbor interaction. In general, we obtain these hopping parameters from Density Functional Theory calculations. These are “ab initio” (or “first-principles”) calculations, i.e., calculations based on basic quantum mechanical considerations, without using any higher order parameters such as hopping terms. This method can be used for systems containing up to the order of thousands of atoms. If we want to go beyond that, or simplify our model, we can distill lattice and tight-binding hopping parameters from the results of a DFT calculation. In this thesis we will consider models containing millions of atoms, for which we will probably need a computer.

### 1.3 Computational physics

In the Manhattan project in the 1940s, physicists used analog computers to perform a huge amount of calculations that were needed to study nuclear fission, which ultimately would produce the atomic bomb. It became apparent that computers could revolutionize the way we do science. When in the late 40s and early 50s the first digital computers were developed, they attracted the interest of many influential physicists such as Enrico Fermi and John von Neumann.

In the early 50s, Enrico Fermi, John Pasta, Stanislaw Ulam and Mary Tsingou studied the time evolution of vibrations in a system of nonlinear springs using a computer. They found a surprising result, namely that a complicated nonlinear system can exhibit periodic behavior. This famous paper is an early example of a “numerical experiment”: a computer simulation of a toy model, a tiny universe in which the programmer sets the rules of physics, that can give us insight into real world phenomena. We will look at toy models in the two chapters of this thesis about self-similar quantum systems (chapters 5 and 6). Looking at it this way, computational physics is of course a theoretical exercise, but it has an experimental element as well.

The computer has come a long way since the 50s. We now do our scientific calculations on cluster nodes that are capable of simulating systems containing more than  $10^8$  atoms. Moreover, the internet has made it

possible to share programming code so that everyone can use it for their research projects. For most of the calculations performed in this thesis we have made our own code that is available on the internet for others to use, as described in chapter 7.

## 1.4 Outline of this thesis

First, we will look at the models and methods used in this thesis. There will be a short description of tight-binding, and an overview of the electronic and optical properties we are interested in. Then we will summarize the tight-binding propagation method (TBPM), a method for calculating properties of large-scale tight-binding systems.

Then we move on to the first application. We study how the electronic properties of antimonene ribbons change if we place them in an electric field. It turns out that the direction in which the field is applied has large consequences for the electronic structure of the material.

In chapter 4 we study the optical properties of black phosphorus. This material behaves differently in two directions, which leads to interesting properties.

In chapters 5 and 6 we look at self-similar systems. It will turn out that their self-similarity leaves a footprint in the way they conduct electrons. Then, we take a look at their optical properties. Again, the self-similarity has large consequences for interaction with light.

Finally, in the appendix, we take a look at the open-source software Tipsi. Tipsi provides an easy way to perform TBPM calculations on any tight-binding system. We discuss how to install it, how to build a Hamiltonian, and how to run the calculations.

## CHAPTER 2

# MODELS AND METHODS

## 2.1 Tight-binding

A tight-binding Hamiltonian can generally be written as

$$\hat{H} = \sum_i \epsilon_i \hat{c}_i^\dagger \hat{c}_i + \sum_{i \neq j} t_{ij} \hat{c}_i^\dagger \hat{c}_j, \quad (2.1)$$

where  $\epsilon_i$  denotes the on-site potential on a local orbital  $i$ ,  $t_{ij}$  (the ‘‘hopping’’ parameter) quantifies the interorbital interaction between orbitals  $i$  and  $j$ , and  $\hat{c}_i^\dagger$  ( $\hat{c}_i$ ) is the electron creation (annihilation) operator on orbital  $i$ . A wave function is written as

$$|\psi\rangle = \sum_i a_i |i\rangle, \quad (2.2)$$

where  $a_i$  is a complex number giving the value of the wave function  $|i\rangle$  on each site  $i$ . From now on, we will omit the hats on operators.

Within a tight-binding model we can incorporate strain, external electric and magnetic fields, and disorder.

The application of external strain changes the interatomic bond lengths, and modifies the hopping terms as [1]

$$\tilde{t}_{ij} = t_{ij} \left( 1 - \beta_{ij} \frac{|\tilde{\mathbf{r}}_{ij} - \mathbf{r}_{ij}|}{|\mathbf{r}_{ij}|} \right), \quad (2.3)$$

where  $\mathbf{r}_{ij}$  is the vector between sites  $i$  and  $j$  in the equilibrium positions between two atoms  $i$  and  $j$ ,  $\tilde{\mathbf{r}}_{ij}$  is this vector in the presence of strain, and  $\beta_{ij}$  is the dimensionless local electron-phonon coupling.

A uniform electric field is applied in the  $z$ -direction by modifying the on-site potentials with

$$\tilde{\epsilon}_i = \epsilon_i + e \times \Delta U \times z_i, \quad (2.4)$$

where  $e$  is the elementary charge,  $\Delta U$  is the bias voltage (with units V/nm) and  $z_i$  is the  $z$ -coordinate of site  $i$ .

We can incorporate a uniform magnetic field  $\mathbf{B} = \nabla \times \mathbf{A}$  using a Peierls-substitution:

$$\tilde{t}_{ij} = t_{ij} \times e^{-i\frac{e}{\hbar} \int_{\mathbf{r}_i}^{\mathbf{r}_j} \mathbf{A}(\mathbf{r}) \cdot d\mathbf{r}}. \quad (2.5)$$

In the Landau gauge  $\mathbf{B} = B\hat{z}$ ,  $\mathbf{A} = -By\hat{x}$ , this becomes

$$\tilde{t}_{ij} = t_{ij} e^{-i\pi\frac{e}{\hbar} B(y_i+y_j)(x_i-x_j)}. \quad (2.6)$$

Finally, in large samples we can study the effect of many types of disorder. For example, vacancies can be simulated by simply leaving out a site from the sample, although in some systems this is actually closer to a model for adsorption of an adatom or admolecule.

## 2.2 Electronic properties

Once we have built our Hamiltonian, and impose periodic boundary conditions, we can perform a Fourier transform and calculate all eigenstates  $|\mathbf{k}i\rangle$  and eigenvalues  $E_i(\mathbf{k})$  for a momentum  $\mathbf{k}$ . In practice, such exact diagonalization has computational complexity  $\mathcal{O}(N^3)$  for  $N$  orbitals.

The band structure of a material is given by the eigenvalues at different momenta and shows the electronic structure around the symmetry points of the crystal. Most importantly, this shows us at which energies the material is conductive, how large the band gap is, and which optical excitations could be possible.

The density of states (DOS) is a histogram of energy levels in the system. It is calculated with

$$D(E) = \frac{1}{2\pi} \int_{BZ} \sum_i \delta(E - E_i(\mathbf{k})) d\mathbf{k}, \quad (2.7)$$

where  $i$  labels the different energy bands, and the momentum  $\mathbf{k}$  is integrated over the Brillouin zone.



### 2.3 Optical properties in momentum description

Linear response theory describes the first-order response of a system to a perturbation [2]. The optical conductivity in the  $\alpha$ -direction, or in other words, the current-current response in the  $\alpha$ -direction from applying an alternating electromagnetic field in the  $\alpha$  direction, is given by the Kubo formula

$$\begin{aligned} \text{Re}(\sigma_{\alpha\alpha}(\omega)) = & -\frac{gs}{\Omega\omega} \int_{BZ} \text{Im} \left[ \sum_{i,j} |\langle \mathbf{k}i | J_{\mathbf{k}\alpha} | \mathbf{k}j \rangle|^2 \right. \\ & \left. \times \frac{f(E_{\mathbf{k}i} - \mu) - f(E_{\mathbf{k}j} - \mu)}{E_{\mathbf{k}i} - E_{\mathbf{k}j} + \omega + i\delta} \right] d^2\mathbf{k}. \end{aligned} \quad (2.8)$$

Here,  $|\mathbf{k}i\rangle$  and  $E_{\mathbf{k}i}$  are the eigenstates and eigenenergies for momentum  $\mathbf{k}$ .  $gs = 2$  is the spin degeneracy,  $\Omega$  is the unit cell surface, and  $\delta$  (usually taken  $\delta = 5$ , unless otherwise specified) meV is a small damping parameter.  $J_{\mathbf{k}\alpha}$  is the momentum-space current operator in the  $\alpha$ -direction

$$J_{\mathbf{k}\alpha} = -\frac{ie}{\hbar} \sum_{i,j} e^{i(\mathbf{r}_j - \mathbf{r}_i)\alpha \cdot \mathbf{k}} t_{ij}(\mathbf{r}_j - \mathbf{r}_i)_\alpha c_{\mathbf{k}i}^\dagger c_{\mathbf{k}j}. \quad (2.9)$$

Moreover,  $f(E - \mu)$  is the Fermi-Dirac distribution with Fermi level  $\mu$ :

$$f(E - \mu) = \frac{1}{e^{(E-\mu)/kT} + 1}. \quad (2.10)$$

Using the Kramers-Kronig relations, we can also obtain the imaginary part

$$\text{Im}(\sigma_{\alpha\alpha}(\omega)) = -\frac{2\omega}{\pi} \mathcal{P} \int_0^\infty \frac{\text{Re}(\sigma_{\alpha\alpha}(\omega'))}{\omega'^2 - \omega^2} d\omega'. \quad (2.11)$$

We use the units  $\sigma_0 = \frac{\pi e^2}{2h}$  for graphene or graphene related structures.

If we want to calculate the full dielectric function of the material, we first need to calculate the dynamical polarization

$$\begin{aligned} \text{Re}(\Pi(\mathbf{q}, \omega)) = & -\frac{g_S}{(2\pi)^2} \int_{BZ} \sum_{i,j} |\langle \mathbf{k}_i | e^{i\mathbf{q}\cdot\mathbf{r}} | \mathbf{k}_j \rangle|^2 \\ & \times \frac{f(E_{\mathbf{k}_i} - \mu) - f(E_{\mathbf{k}_j} - \mu)}{E_{\mathbf{k}_i} - E_{\mathbf{k}_j} + \omega + i\delta} d^2\mathbf{k}, \end{aligned} \quad (2.12)$$

Then, using the random phase approximation (RPA), the dielectric function is given by

$$\epsilon(\mathbf{q}, \omega) = \mathbf{1} - V(\mathbf{q})\Pi(\mathbf{q}, \omega), \quad (2.13)$$

where

$$V(\mathbf{q}) = \frac{2\pi e^2}{\kappa|\mathbf{q}|} \quad (2.14)$$

is the Fourier component of the Coulomb interaction in two dimensions, and  $\kappa$  is the background dielectric constant.

The loss function can then be written as

$$-\text{Im} \frac{1}{\epsilon(\mathbf{q}, \omega)}. \quad (2.15)$$

## 2.4 Optical properties in real-space description

For systems without translational invariance, we cannot compute momentum eigenstates, and we need a different way to calculate optical properties.

First, let us take a look at the joint density of states (JDOS), which is given by:

$$\text{Im}\chi_{\text{JDOS}}(\omega) = \frac{1}{\hbar} \text{Im} \sum_{nm} \frac{f(E_m - \mu) - f(E_n - \mu)}{\hbar\omega + E_m - E_n + i\delta}. \quad (2.16)$$

Using the JDOS, we can calculate an effective conductivity-like function

$$\text{Re}\sigma_{\text{JDOS}}(\omega) = -\frac{1}{\omega} \text{Im}\chi_{\text{JDOS}}(\omega) , \quad (2.17)$$

which quantifies the density of available electronic transitions with energy  $\hbar\omega$  between state-pairs. However, in general there are selection rules for optical transitions, and not every available transition is allowed.

To get the optical spectrum, we write the current-current response function [2] in the form

$$\chi_{J_\alpha J_\beta}(\omega) = \sum_{nm} Q_{mn}(\omega) , \quad (2.18)$$

where

$$Q_{mn}(\omega) = \frac{1}{\hbar A} \frac{f(E_m - \mu) - f(E_n - \mu)}{\hbar\omega + E_m - E_n + i\delta} (J_\alpha)_{mn} (J_\beta)_{nm} \quad (2.19)$$

and  $(J_\alpha)_{mn}$  are the matrix elements of the current operator

$$(J_\alpha)_{mn} = \langle \psi_m | J_\alpha | \psi_n \rangle , \quad (2.20)$$

$$J_\alpha = -\frac{ie}{\hbar} \sum_{i,j} t_{ij} (\mathbf{r}_j - \mathbf{r}_i)_\alpha c_i^\dagger c_j . \quad (2.21)$$

Here,  $|\psi_m\rangle$  are the eigenstates of the Hamiltonian.

The dielectric function operator  $\varepsilon(\omega)$ , by definition, relates the external potential  $V_{\text{ext}}(\omega)$  to the total potential  $V$ :

$$\langle \mathbf{r} | V_{\text{ext}}(\omega) | \mathbf{r} \rangle = \int d\mathbf{r}' \langle \mathbf{r} | \varepsilon(\omega) | \mathbf{r}' \rangle \langle \mathbf{r}' | V | \mathbf{r}' \rangle . \quad (2.22)$$

Treating  $V$  as a perturbation, within RPA, the dielectric function may be

expressed as follows [3]:

$$\begin{aligned}
 \langle \mathbf{r} | \varepsilon(\omega) | \mathbf{r}' \rangle &= \langle \mathbf{r} | \mathbf{r}' \rangle - \int d\mathbf{r}'' \langle \mathbf{r} | V_C | \mathbf{r}'' \rangle \langle \mathbf{r}'' | \chi(\omega) | \mathbf{r}' \rangle, \\
 \langle \mathbf{r} | V_C | \mathbf{r}'' \rangle &\equiv \frac{e^2}{\|\mathbf{r} - \mathbf{r}''\|}, \\
 \langle \mathbf{r}'' | \chi(\omega) | \mathbf{r}' \rangle &= g_S \cdot \lim_{\delta \rightarrow 0^+} \sum_{m,n} G_{mn} \langle \psi_n | \mathbf{r}'' \rangle \langle \mathbf{r}'' | \psi_m \rangle \langle \psi_m | \mathbf{r}' \rangle \langle \mathbf{r}' | \psi_n \rangle, \\
 G_{mn} &\equiv \frac{f(E_m - \mu) - f(E_n - \mu)}{E_m - E_n - \hbar(\omega + i\delta)}.
 \end{aligned} \tag{2.23}$$

$|\mathbf{r}\rangle$  denotes a position eigenvector;  $V_C$  is the Coulomb interaction potential;  $\chi(\omega)$  is the polarizability function.

Eqs. (2.23) allow us to exactly calculate the full dielectric function  $\varepsilon(\omega)$  of any tight-binding system without translational invariance. Tom Westerhout wrote code for calculating these quantities, available as an open source project [4]. Despite the  $\mathcal{O}(N^4)$  algorithmic complexity, it makes calculations possible for systems of up to several thousands of sites.

## 2.5 Transport properties

Following Landauer theory [5], the electronic conductance  $G$  in the scattering-free limit is obtained by counting modes:

$$G(E) = \frac{2e^2}{h} \sum_k N_k(E), \tag{2.24}$$

where  $N_k(E)$  is the number of bands that cross the energy  $E$  for a given wave-vector  $k$ .

However, if there is scattering, we need to use a method called wave function matching. We attach semi-infinite leads to either side of the scattering region (Fig. 2.1) and model incoming electrons as Bloch waves

in one of those leads. The Hamiltonian is given by

$$H = \begin{pmatrix} \ddots & V_L & & \\ V_L^\dagger & H_L & V_L & \\ & V_L^\dagger & H_L & V_{LS} \\ & & V_{LS}^\dagger & H_S \end{pmatrix}, \quad (2.25)$$

where  $H_L$  is the Hamiltonian of the leads and  $H_S$  is the Hamiltonian of the scattering region;  $V_i$  connects those Hamiltonians. The scattering states in the leads take the form

$$\psi_n(i) = \phi_n^{\text{in}}(i) + \sum_n S_{mn} \phi_m^{\text{out}}(i) + \sum_p \tilde{S}_{pn} \phi_p^{\text{ev}}(i), \quad (2.26)$$

where  $\phi_n^{\text{in, out}}(i)$  are normalized incoming and outgoing propagating modes in the  $i$ -th unit cell away from the scattering center, and  $\phi_p^{\text{ev}}(i)$  are evanescent modes that do not contribute to the conductance. These modes have the form

$$\psi_n(i) = (\lambda_n)^i \chi_n, \quad (2.27)$$

and obey the Schrödinger equation

$$(H_L + V_L \lambda_n^{-1} + V_L^\dagger \lambda_n) \chi_n = E \chi_n. \quad (2.28)$$

Then we can compute the wave functions in the scattering region  $\phi_n^S$  and the scattering matrix  $S_{mn}$  for each incoming propagating mode  $n$  and an outgoing mode  $m$ . The conductance  $G$  between the left lead A and the right lead B is then given by the Landauer formula

$$G(E) = \frac{2e^2}{h} \sum_{n \in A, m \in B} |S_{mn}(E)|^2. \quad (2.29)$$

This method is implemented in the KWANT package [6] for python.

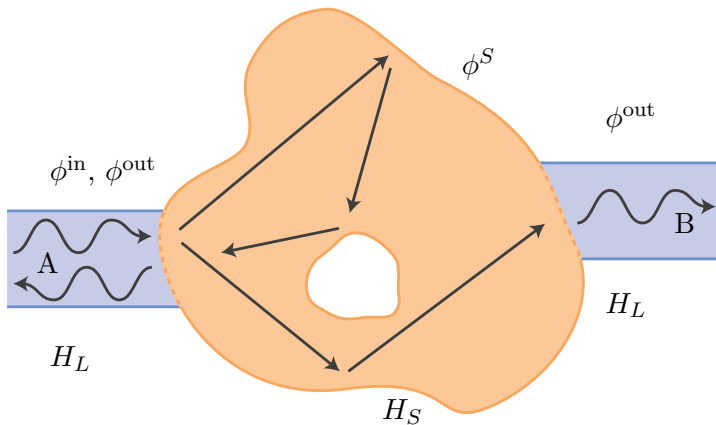


Figure 2.1: An illustration of the conductance calculation using wave function matching.

## 2.6 Tight-binding propagation method

If our model is too big to diagonalize the Hamiltonian, so that we cannot use the methods in the previous sections, we can revert to stochastic methods. We employ a method named the Tight-Binding Propagation Method (TBPM), which computes the time propagation of a set of random wave functions, and extracts physical quantities from the resulting correlation functions [7, 8]. The computational cost of this method is only  $\mathcal{O}(N)$ , which makes it possible to do computations on systems up to the order of  $N = 10^8$  orbitals.

For rigorous mathematical proofs on the formulas in this section, we refer to Yuan et al. (2010) and Hams et al. (2000) [7, 8].

We start our TBPM computation by taking a random state

$$|\psi(0)\rangle = \sum_i a_i |i\rangle, \quad (2.30)$$

where  $a_i$  are random complex numbers with  $\sum_i |a_i|^2 = 1$ . Then we calculate its time evolution

$$|\psi(t)\rangle = e^{-iHt}|\psi(0)\rangle. \quad (2.31)$$

We use the Chebyshev polynomial decomposition of the Hamiltonian to compute  $|\psi(t)\rangle$ . First, we normalize  $H$  so that  $\tilde{H} = H/\|H\|$  has eigenvalues in the range  $[-1, 1]$  and define  $\tilde{t} = \|H\|t$ . Then, the time evolution can be represented as

$$|\psi(\tilde{t})\rangle = \left[ J_0(\tilde{t})T_0(\tilde{H}) + 2 \sum_{m=1}^{\infty} J_m(\tilde{t})T_m(\tilde{H}) \right] |\psi(0)\rangle, \quad (2.32)$$

where  $J_m(x)$  is the Bessel function of the first kind of order  $m$ . The modified Chebyshev polynomials  $T_m$  can be calculated up to machine precision by using the recurrence relation

$$T_{m+1}(\tilde{H})|\psi\rangle = -2i\tilde{H}T_m(\tilde{t})|\psi\rangle + T_{m-1}(\tilde{H})|\psi\rangle, \quad (2.33)$$

$$T_0(\tilde{H})|\psi\rangle = |\psi\rangle, \quad T_1(\tilde{H})|\psi\rangle = -i\tilde{H}|\psi\rangle. \quad (2.34)$$

### 2.6.1 DOS

The density of states can be calculated with

$$D(E) = \frac{1}{2\pi} \int_{-\infty}^{\infty} e^{iEt} C_{\text{DOS}}(t) dt, \quad (2.35)$$

where the DOS correlation function is

$$C_{\text{DOS}}(t) = \langle \psi(0) | \psi(t) \rangle \quad (2.36)$$

The calculation of the correlation function can be improved using an average over many random initial states. In practice, for a large enough system, the random initial state is already a superposition of all eigenstates, which makes sure that the result is correct. The same argument holds for the calculation of other quantities, where we can also average over multiple random initial states, which becomes less necessary for larger systems.

### 2.6.2 Quasi-eigenstates

An approximation of an eigenstate (or a superposition of degenerate eigenstates) at a certain energy  $E$  can be calculated using the spectrum method:

$$|\psi(E)\rangle = \frac{1}{2\pi} \int_{-\infty}^{\infty} e^{iEt} |\psi(t)\rangle dt, \quad (2.37)$$

after which  $|\psi(E)\rangle$  is normalized.

### 2.6.3 DC conductivity

By using the DOS and quasi-eigenstates obtained earlier, as well as the Kubo formula [9] we can calculate the DC conductivity  $\sigma_\alpha$  in direction  $\alpha$  at zero temperature with [10, 7]

$$\sigma_\alpha(E) = \frac{d(E)}{A} \int_0^\infty \text{Re} [e^{-iEt} C_{\text{DC}}(t)] dt, \quad (2.38)$$

$$C_{\text{DC}}(t) = \frac{\langle \psi(0) | J_\alpha e^{iHt} J_\alpha | \psi(E) \rangle}{|\langle \psi(0) | \psi(E) \rangle|}, \quad (2.39)$$

where  $A$  is the area of the unit cell, divided by the total number of orbitals. Here, it is important to note that  $|\psi(0)\rangle$  must be the same random initial state used in the calculation of  $|\psi(E)\rangle$ . Moreover, for this calculation we again need the real-space current operator

$$J_\alpha = -\frac{ie}{\hbar} \sum_{i,j} t_{ij} (\mathbf{r}_j - \mathbf{r}_i)_\alpha c_i^\dagger c_j, \quad (2.40)$$

### 2.6.4 AC conductivity

Using Kubo's formula, we can write for the optical conductivity in direction  $\alpha$  due to a field in direction  $\beta$  [10, 7]:

$$\text{Re}\sigma_{\alpha\beta}(\omega) = \lim_{\epsilon \rightarrow 0^+} \frac{e^{-\hbar\omega/k_B T}}{\hbar\omega A} \int_0^\infty e^{-\epsilon t} \sin(\omega t) 2C_{\text{AC}}(t) dt, \quad (2.41)$$



$$C_{AC}(t) = \text{Im}\langle\psi_2(t)|J_\alpha|\psi_1(t)\rangle_\beta. \quad (2.42)$$

Here, we use the Fermi-Dirac distribution operator

$$f(H - \mu) = \frac{1}{e^{\beta(H-\mu)} + 1}, \quad (2.43)$$

and the wave functions

$$|\psi_1(t)\rangle_\beta = e^{-iHt}[1 - f(H - \mu)]J_\beta|\psi(0)\rangle, \quad (2.44)$$

$$|\psi_2(t)\rangle = e^{-iHt}f(H - \mu)|\psi(0)\rangle. \quad (2.45)$$

### 2.6.5 Dynamical polarization

Finally, we can express the dynamical polarization as [11]

$$\Pi(\mathbf{q}, \omega) = -\frac{2}{A} \int_0^\infty e^{i\omega t} C_{DP}(t) dt, \quad (2.46)$$

$$C_{DP}(t) = \text{Im}\langle\psi_2(t)|\rho(\mathbf{q})|\tilde{\psi}_1\mathbf{q}, (t)\rangle, \quad (2.47)$$

where the density operator is given by

$$\rho(\mathbf{q}) = \sum_i e^{i\mathbf{q}\cdot\mathbf{r}_i} c_i^\dagger c_i \quad (2.48)$$

and

$$|\tilde{\psi}_1(\mathbf{q}, t)\rangle_\beta = e^{-iHt}[1 - f(H - \mu)]\rho(-\mathbf{q})|\psi(0)\rangle, \quad (2.49)$$

$$|\psi_2(t)\rangle = e^{-iHt}f(H - \mu)|\psi(0)\rangle. \quad (2.50)$$

## CHAPTER 3

# ANTIMONENE RIBBONS UNDER BIAS

A systematic study of the electronic properties of single layer Sb (antimonene) nanoribbons is presented. By using a 6-orbital tight-binding Hamiltonian, we study the electronic band structure of ribbons with zigzag and armchair termination. We show that there is good agreement between *ab initio* calculations and the tight-binding model. We study how the size of the gap can be controlled by applying an external bias potential. An electric field applied perpendicular to the antimonene layer is found to increase the band gap, while a transverse bias potential leads to a position dependent reduction of the band gap. Both kinds of bias potential break inversion symmetry of the crystal. This, together with the strong intrinsic spin-orbit coupling of antimonene, leads to spin-splitting of the valence band states.

*This chapter is published as: E. van Veen, J. Yu, M.I. Katsnelson, R. Roldán, S. Yuan “Electronic structure of monolayer antimonene nanoribbons under out-of-plane and transverse bias,” Phys. Rev. Materials 2, 114011 (2018).*

### 3.1 Introduction

Two dimensional (2D) materials [12], such as graphene, transition metal dichalcogenides and hexagonal boron nitride, are attracting tremendous interest due to their unique electronic, optical and mechanical properties, remarkably different from their three-dimensional counterparts [13]. Recently, the family of 2D materials derived from the group-VA layered crystals (P, As, Sb, Bi) has been the focus of great attention [14, 15], black phosphorus being the most well studied among them. In 2015 Zhang *et al.* predicted that, contrary to bulk antimony which is a semimetal, single-layer Sb (antimonene) is an indirect band gap semiconductor [16]. Soon after, it was demonstrated that atomically thin antimonene can be obtained by different means, including van der Waals epitaxy [17], micromechanical exfoliation [18], liquid phase exfoliation [19], molecular beam epitaxy [20] or electrochemical exfoliation [21]. Theoretical calculations have studied in detail the electronic properties of this material [22, 23, 24, 25, 26]. Strong spin-orbit coupling was also reported, with a coupling strength of  $\lambda \approx 0.34$  eV [27]. *Ab initio* quantum transport calculations have shown that antimonene field effect transistors (FETs) can satisfy both the low power and high performance requirements for usage in nanoscale electronic and optoelectronic devices [28]. Previous experience with graphene and other 2D materials has further motivated theoretical studies of the electronic properties of nanoribbons of group-VA semiconductors [29, 30, 31, 32, 33]. Recently, experimental fabrication of antimonene nanoribbons has been reported [34], demonstrating band gap opening due to quantum confinement.

In this chapter we study the band structure and electronic properties of Sb nanoribbons in the presence of out-of-plane and in-plane electric fields. We find that edge states are present in nanoribbons with both zigzag and armchair termination. We find good agreement between *ab initio* numerical simulations and tight-binding calculations. We further demonstrate that the size of the band gap can be controlled by the presence of an external bias field. Application of a bias field breaks inversion symmetry which, together with the strong spin-orbit coupling in antimonene, leads to splitting of the valence band edges, with corresponding spin-valley coupling due to the

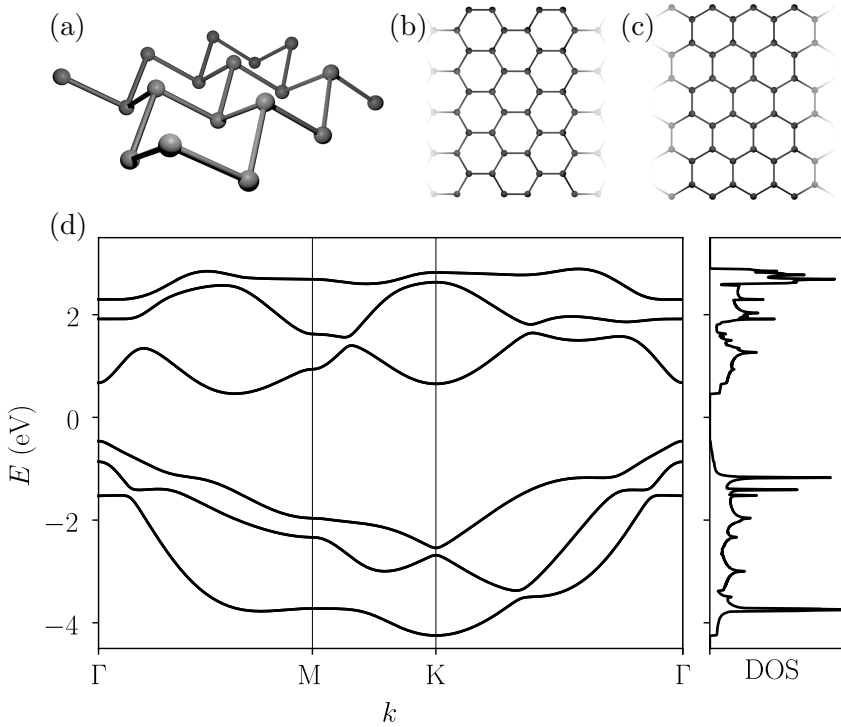


Figure 3.1: (a) The buckled honeycomb lattice structure of antimony, (b) an armchair SbNR and (c) a zigzag SbNR. (d) Band structure and DOS for pristine Sb calculated with the tight-binding Hamiltonian (3.1), with the hopping parameters given in Table 3.1.

Rashba effect.

The chapter is organized as follows. In Sec. 3.2 we describe the tight-binding model and the details of the calculations. We also show results for unbiased nanoribbons. In Sec. 3.3 we study the effect of a perpendicular electric field on the electronic properties and the band structure of Sb-nanoribbons, and the effect of an in-plane bias field is studied in Sec. 3.4.

Our main results are summarised in Sec. 3.5.

## 3.2 Model and method

Single layer antimonene consists on a buckled honeycomb lattice of Sb atoms (Fig. 3.1), with the two sublattices vertically displaced by  $b = 1.65 \text{ \AA}$ , and with an in-plane lattice constant of  $a = 4.12 \text{ \AA}$ . The relevant energy bands of the electronic structure, including SOC effects, are very well captured by a 6-orbitals tight-binding Hamiltonian developed by Rudenko *et al.* [27], which includes the 3  $p$ -orbitals of each of the two Sb atoms of the unit cell:

$$\begin{aligned}
 H = & \sum_m \sum_i \sum_\sigma \epsilon_{mi\sigma} c_{mi\sigma}^\dagger c_{mi\sigma} \\
 & + \sum_{mn} \sum_{ij} \sum_\sigma t_{mi\sigma;nj\sigma} c_{mi\sigma}^\dagger c_{nj\sigma} \\
 & + \sum_{mn} \sum_i \sum_{\sigma\sigma'} h_{mi\sigma;ni\sigma'} c_{mi\sigma}^\dagger c_{ni\sigma'}
 \end{aligned} \tag{3.1}$$

where  $m, n$  run over orbitals,  $i, j$  run over sites and  $\sigma, \sigma'$  run over spins;  $c_{mi\sigma}^\dagger$  ( $c_{mi\sigma}$ ) is the creation (annihilation) operator on orbital  $m$  at site  $i$  with spin  $\sigma$ . The parameters  $\epsilon_{mi\sigma}$  account for on-site potentials,  $t_{mi\sigma;nj\sigma}$  are inter-orbital hopping terms, and intra-atomic SOC is accounted by  $h_{mi\sigma;ni\sigma'}$ . The intra-atomic SOC constant is  $\lambda = 0.34 \text{ eV}$  and the hopping parameters are given in Table 3.1 [27] and schematically shown in Fig. 3.2.

The corresponding DOS is calculated from Eq. 2.7. The band structure and DOS obtained with this model for bulk antimonene are shown in Fig. 3.1. Single layer antimonene is an indirect gap semiconductor with a band gap of 0.92 eV. The edge of the valence band is located at the  $\Gamma$  point of the BZ, with main contributions from  $p_x$  and  $p_y$  orbitals, while the edge of the conduction band is placed at a non high-symmetry point of the BZ, with relevant contributions from all 3  $p$ -orbitals of Sb.

Since we are interested in electronic properties of semi-infinite ribbons, the momentum parallel to the infinite edge is a good quantum number and we can Fourier-transform Hamiltonian (3.1) along that direction. The

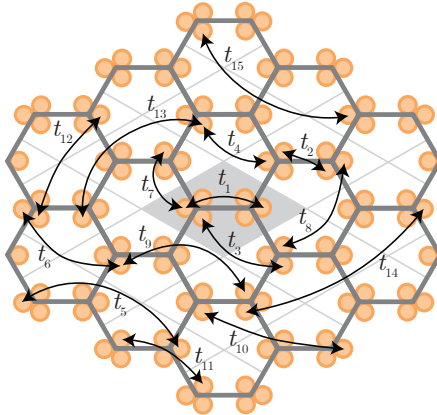


Figure 3.2: Top view of the antimonene crystal structure with the hopping parameters ( $t_i$ ) included in the TB model. Their corresponding values are given in Table 3.1. The orange circles represent  $p$ -orbitals.

band structure of finite nanoribbons (we impose periodic boundary conditions along the direction parallel to the edge) with zigzag and armchair termination are shown in Fig. 3.3. Firstly, the finite width of the antimonene ribbon leads to a reconstruction of the band structure with the formation of electronic bands composed by the accumulation of  $N$  subbands, where  $N$  is the number of unit cells along the width of the ribbon. Secondly, midgap edge states appear in both armchair and zigzag nanoribbons (Fig. 3.3), originating from the unsaturated bond on the edge of the ribbon. This is different from graphene and black phosphorus ribbons, for which edge states are absent for armchair termination [35, 32]. The energy bands associated to the edge states are flat and weakly dispersing, leading to prominent peaks in the DOS associated to saddle points in the band structure.

In this work, we only consider chemically unsaturated edges, i.e., we

Table 3.1: Hopping amplitudes  $t_i$  (in eV) entering in the TB Hamiltonian Eq. (3.1), as obtained in [27].  $d$  denotes the distance between the lattice sites on which the interacting orbitals are centered.  $N_c$  is the corresponding coordination number. The hoppings are schematically shown in Fig. 3.2.

$i$	$t_i$ (eV)	$d$ (Å)	$N_c$	$i$	$t_i$ (eV)	$d$ (Å)	$N_c$	$i$	$t_i$ (eV)	$d$ (Å)	$N_c$
1	-2.09	2.89	1	6	0.21	4.12	1	11	-0.06	4.12	2
2	0.47	2.89	2	7	0.08	2.89	2	12	-0.06	5.03	1
3	0.18	4.12	4	8	-0.07	5.03	2	13	-0.03	6.50	2
4	-0.50	4.12	1	9	0.07	6.50	2	14	-0.04	8.24	1
5	-0.11	6.50	2	10	0.07	6.50	2	15	-0.03	8.24	1

do not take edge chemistry into account. Attaching different atoms to the edge could significantly alter the electronic structure around the Fermi level [36].

To check whether our bulk TB model agrees with *ab initio* calculations also for finite ribbons, we performed first-principles calculations on the electronic structure of antimony nanoribbons, including SOC, using the Vienna *ab initio* simulation package (VASP) [37, 38]. Electron exchange and correlation interactions were described using the Perdew-Burke-Ernzerhof (PBE) pseudopotentials within the projector augmented-wave method [39]. The Brillouin zone sampling was done using a  $35 \times 1 \times 1$  Monkhorst-Pack grid for static calculation. The atomic structure of the nanoribbons are obtained from the 2D nanosheet without structure relaxation, and the vacuum region between two adjacent images is set to be 100 Å. The results are shown in Fig. 3.4, in comparison to tight-binding calculations. We can see that the agreement between the two methods is reasonable. Apart from some slight shifts in energies, the contours of the conduction band minimum (CBM), valence band maximum (VBM) and edge states in the TB model are very similar to the DFT result. We notice that previous first-principles calculations for narrow nanoribbons, of up to  $\sim 3.4$  nm, predicted a direct band gap for zigzag termination [31], which is also in agreement with our own TB calculations. By systematically studying the evolution of the bandgap

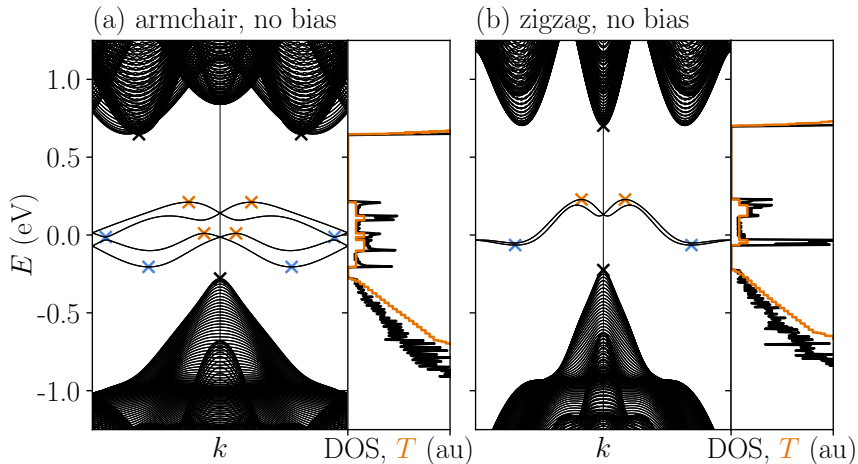


Figure 3.3: Band structure, DOS and transmission for (a) an armchair ribbon of width 41 nm and (b) a zigzag ribbon of width 36 nm. The conduction and valence band edges are indicated with black crosses, the edge band maxima are orange and the edge band minima are blue. The midgap bands correspond to edge states.

with nanoribbon size, we conclude that the two secondary CBMs around  $k = \pm 0.63 \frac{\pi}{W}$  get closer to the the CBM at  $k = 0$  for increasing size. For a ribbon width of 175 nm, the difference between their energy values is only on the order of  $10^{-5}$  eV.

The midgap states are highly localized at the edges, as can be seen in Fig. 3.5. For zero bias, each  $\mathbf{k}$  presents two degenerate states with opposite spin in opposite sides of the ribbon. Since time-reversal symmetry must be preserved, the spin polarization of one edge associated with one state of a given wave-vector  $\mathbf{k}$ , is compensated by the opposite spin polarization of the degenerate state with momentum  $-\mathbf{k}$ .

In the following, we calculate the electronic transmission  $T(E)$  in the scattering-free limit, which is obtained by counting modes (Eq. 2.24). The



Table 3.2: Effective masses for antimonene nanoribbons.

edge	$m_e^* (m_0)$	$m_h^* (m_0)$
armchair	0.2	0.13
zigzag	0.13	0.09

results for each termination are shown in Fig. 3.3 (solid orange lines), together with the DOS (solid black lines).

The main difference between the transmission in zigzag and armchair nanoribbons occurs for energies within the bulk bandgap. At these energies  $T(E)$  is dominated by edge states which, as we have seen, are different for zigzag and armchair terminations. As the ribbon width increases, the transmission function corresponding to the bulk states increases, accompanied by a reduction of the energy gap, while the transmission of the edge states remains the same.

We have further calculated the effective mass of electrons  $m_e^*$  and holes  $m_h^*$  from the nanoribbon band structure (table 3.2). Electrons are heavier than holes for both edge terminations. We also find that carriers in zigzag nanoribbons are expected to have lower effective masses than in armchair nanoribbons. These results can be useful for calculations based on low energy  $\mathbf{k} \cdot \mathbf{p}$  analytical models.

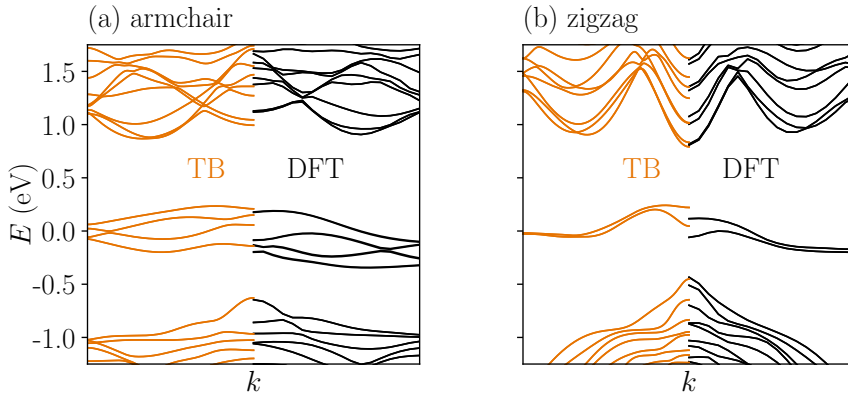


Figure 3.4: Comparison of the band structure of nanoribbons as obtained from tight-binding and DFT methods: (a) a 2.3 nm width ribbon with armchair termination, and (b) a 2.9 nm width ribbon with zigzag termination. Orange corresponds to TB method and black to DFT calculations.

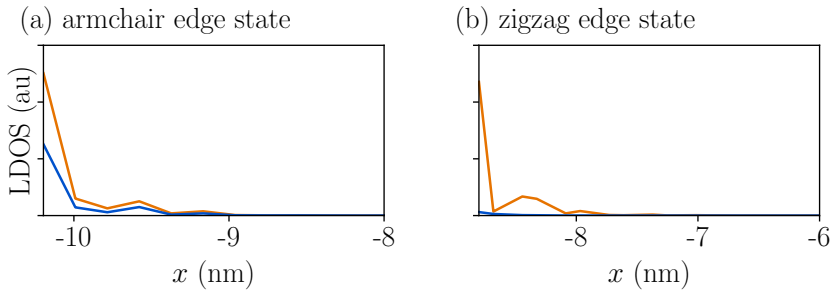


Figure 3.5: LDOS of edge states at  $k = \frac{\pi}{2W}$  for (a) an armchair ribbon of width 20 nm and (b) a zigzag ribbon of width 18 nm. The orange and blue lines correspond to spin up and down, respectively. Notice that these states are degenerate with the corresponding states for  $k = -\frac{\pi}{2W}$ , which have opposite spin.

### 3.3 Out-of-plane bias

Application of external gate voltages is a powerful tool to control and tune the electronic and optical properties of layered 2D materials [40]. In this section we study the effect of a perpendicular bias voltage on antimonene. Since monolayer Sb is buckled, the application of an electric field perpendicular to the sample leads to a potential difference between atoms in different planes. Therefore we introduce an out-of-plane bias  $\Delta V_P$  (without considering screening) by setting the on-site potential on the two sublattices in Hamiltonian (3.1) to different values:

$$\epsilon_{mi\sigma} = \Delta V_P \times z_i, \quad (3.2)$$

where  $z_i$  is the  $z$ -coordinate of site  $i$  in the buckled structure, which is plus or minus  $0.82 \text{ \AA}$  on sublattice A or B, respectively. Our results for the zigzag and armchair nanoribbon band structure, with the corresponding DOS and electronic transmission, are given in Fig. 3.6. First, we notice that for both types of ribbon, we obtain a bandgap widening under the application of the electric field. The evolution with the applied bias of the valence and conduction bands, as well as the edge states, are shown in Fig. 3.7. Opening of the bandgap with electric field was also predicted for single-layer black phosphorus [41]. Interestingly, application of a bias voltage breaks inversion symmetry (sublattices A and B are no longer equivalent). This, together with the strong spin-orbit coupling leads, due to the Rashba effect, to splitting of the edge states, and of the valence and conduction bands. Notice that, because of the latter, the zigzag ribbon band gap becomes indirect when a bias is applied (see insets of Fig. 3.6 for a close-up of the valence band edge). Application of a perpendicular bias field opens, therefore, the possibility to dynamically tune the Rashba energy [42], or to study unconventional transport properties associated with entanglement between spin and charge degrees of freedom [43].

The local distribution of the eigenstates can be investigated by calculating the Local Density of States (LDOS) [44], which is the probability amplitude as a function of location, in the transverse direction of the ribbon. Our results for the LDOS corresponding to the valence band are

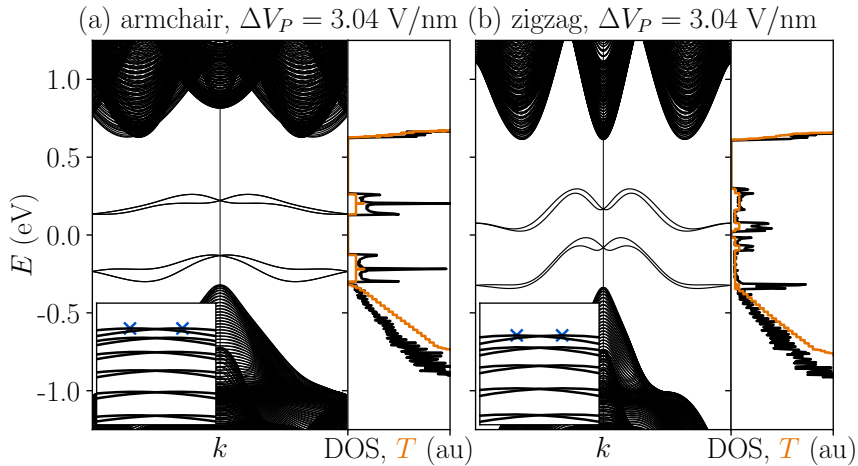


Figure 3.6: Top: band structure, DOS and transmission with  $\Delta V_P = 3.04$  V/nm for (a) an armchair ribbon of width 41 nm and (b) a zigzag ribbon of width 36 nm. Insets: close up of the edge of the valence band, with blue crosses to indicate the maxima.

shown in Fig. 3.8. First, we notice that in the absence of a bias field, the maximum of the valence band is doubly degenerate (due to spin). The local distribution of the VB states is maximum at the center of the ribbon, and decays as we approach the ribbon edges (panels (a) and (b)). The situation is different when an out-of-plane electric field is applied: as discussed above, due to Rashba coupling the edge of the VB is split into two maxima around  $\Gamma$  (see insets of Fig. 3.6) and the spin degeneracy is broken. The consequence of this on the LDOS is seen in Fig. 3.8 (c) and (d). The states corresponding to the left maximum (panel (c)) present a major contribution of spin down (up) at the left (right) side of the center of the ribbon. Of course, since time-reversal symmetry must be conserved, the opposite happens for the states associated with the right VBM (panel (d)).

For the armchair ribbon, for nonzero out-of-plane bias, the two lower

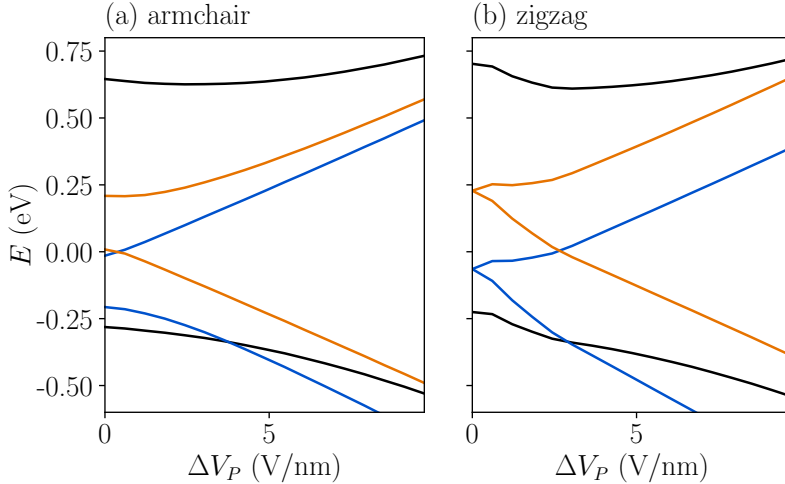


Figure 3.7: Band edges as function of  $\Delta V_P$  for an armchair ribbon of width 41 nm (left) and a zigzag ribbon of width 36 nm (right). Black lines correspond to the conduction and valence band edges, and orange (blue) corresponds to the maxima (minima) of the edge states, corresponding to the crosses in Figure 3.3.

midgap bands move down and the two upper bands move up. For the zigzag case, however, the two midgap bands that were originally doubly degenerate, split into two pairs of non-degenerate bands. The edge states on one side of the ribbon move up in energy, while the states on the other side move down. This is due to the fact that the sites on one edge of the ribbon have  $z$ -coordinate of  $+0.82 \text{ \AA}$  and on the other edge  $-0.82 \text{ \AA}$ , because of the buckled structure.

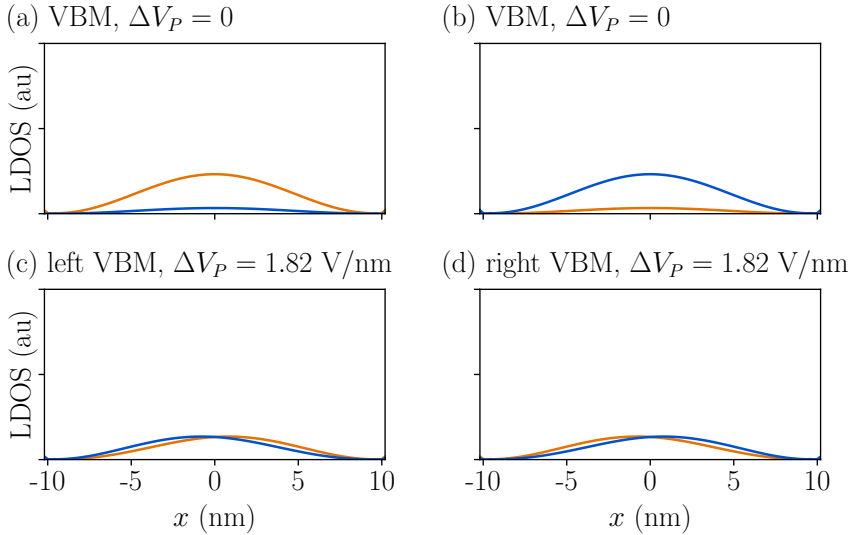


Figure 3.8: LDOS of the valence band maxima for an armchair ribbon of width 20 nm, under out-of-plane bias. The orange and blue lines correspond to spin up and down, respectively.

### 3.4 In-plane transverse bias

Another way to tune the band structure is by applying an in-plane electric field. This way, we create a transverse bias potential along the ribbon. To account for a transverse bias  $\Delta V_T$ , we set in the Hamiltonian (3.1) the on-site energy to

$$\epsilon_{mi\sigma} = \Delta V_T \times x_i, \quad (3.3)$$

where  $x_i$  is the coordinate of site  $i$  in the transverse direction. Our results for two different values of bias field are given in Fig. 3.9. First, we observe a band gap reduction for both types of edge termination. The evolution of the valence and conduction band edges, as well as the position of the extrema of the edge states, are shown in Fig. 3.10. Notice that the colored lines,

corresponding to the edge states, are cut when such states can no longer be distinguished from the conduction or valence band states in the band structure. Similar to the case of an out-of-plane field, inversion symmetry is broken along the ribbon, and the edge states are split (see insets of Fig. 3.9).

The main difference with respect to the case of out-of-plane bias is that the edges of the valence and conduction bands correspond to states that are located at the edges of the ribbon. This is clearly seen in the LDOS calculations (Fig. 3.11). While the states that form the valence band edge are placed at the right edge (see Fig. 3.11 (a) and (b)), the conduction band edge is located at the left edge of the ribbon, as can be seen in Fig. 3.11 (c) and (d).

As the sites on the edges gain an on-site potential  $\pm\Delta V_T \frac{W}{2}$ , the edge states on one side of the ribbon move up in energy, while on the other side they move down. Otherwise, the shape of the edge states stays the same.

These results are similar to those obtained for a black phosphorus nanoribbon in the presence of a transverse electric field [30]. The local separation between the conduction and valence bands states can be quantified by calculating the polarization [7]  $P = e \sum_{mi\sigma} \mathbf{r}_i c_{mi\sigma}^\dagger c_{mi\sigma}$ , which yields  $\langle P \rangle_{\text{VBM}} = 5.61e \text{ nm}$  and  $\langle P \rangle_{\text{CBM}} = -7.25e \text{ nm}$  for this configuration.

Moreover, applying a transverse bias causes the valence band to split, lifting the degeneracy of the predominantly spin up and spin down states at the VBM. This is due to the fact that Rashba coupling is also present in this case (see insets in Fig. 3.9), which leads to different spin polarization of the two extrema of the valence band, represented by different color of the two VBM (panels (a) and (b) of Fig. 3.11). The armchair CBM also becomes spin-polarized. For the zigzag case, and for ribbons with  $W < 62 \text{ nm}$ , the CBM is at  $k = 0$ , where there is no spin-polarization.

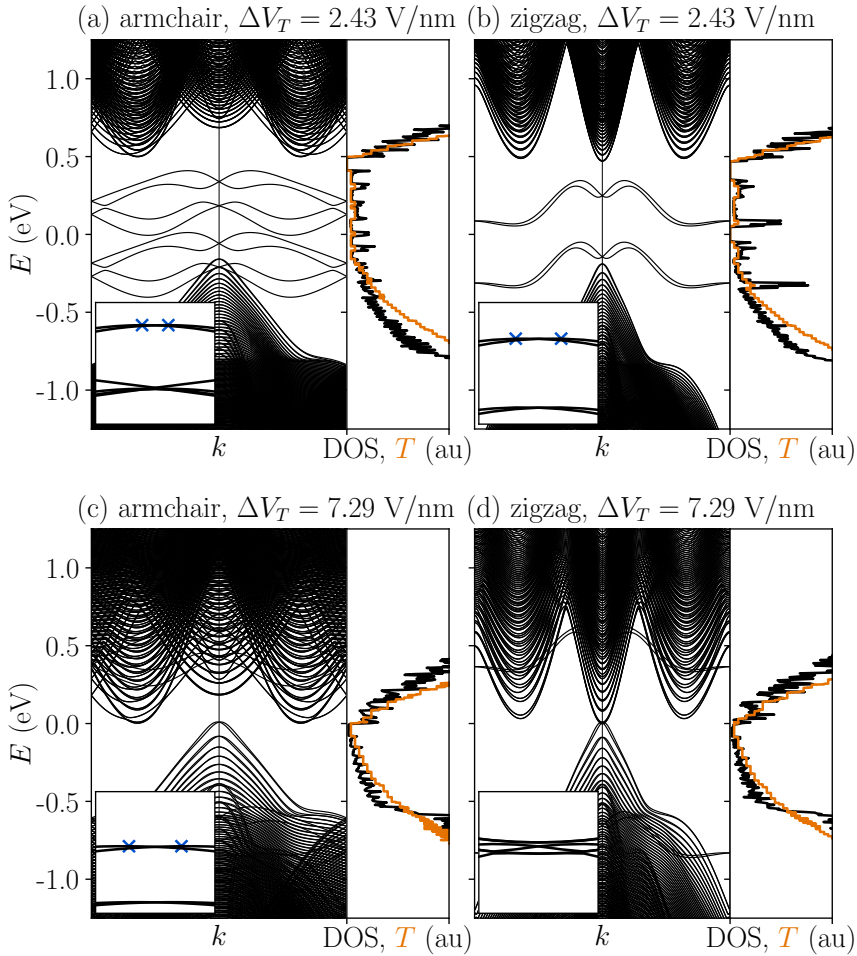


Figure 3.9: Top: band structure, DOS and transmission for (a) an armchair ribbon of width 41 nm with  $\Delta V_P = 2.43$  V/nm; (b) a zigzag ribbon of width 36 nm with  $\Delta V_P = 2.43$  V/nm; (c) an armchair ribbon of width 41 nm with  $\Delta V_P = 7.29$  V/nm and (d) a zigzag ribbon of width 36 nm with  $\Delta V_P = 7.29$  V/nm. Insets: close up of the edge of the valence band.



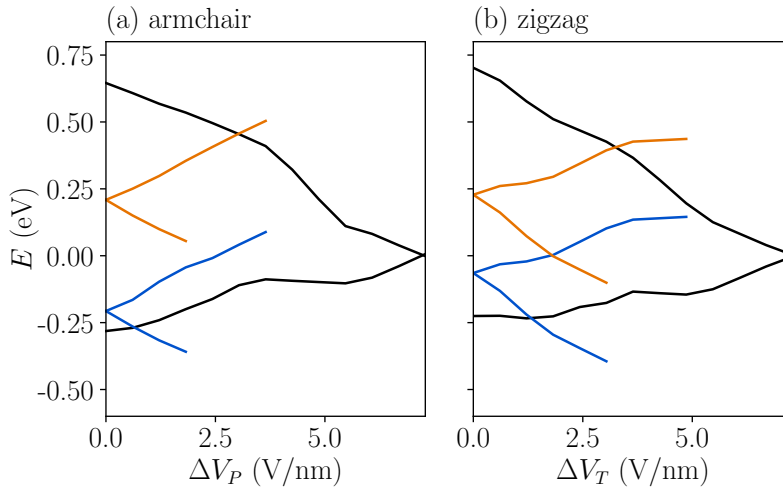


Figure 3.10: Band edges as function of  $V_T$  for (a) an armchair ribbon of width 41 nm and (b) a zigzag ribbon of width 36 nm. Black lines correspond to the conduction and valence band edges, and orange (blue) corresponds to the maxima (minima) of the edge states. The curves corresponding to edge states are cut when such states can no longer be distinguished from the conduction or valence band states in the band structure.

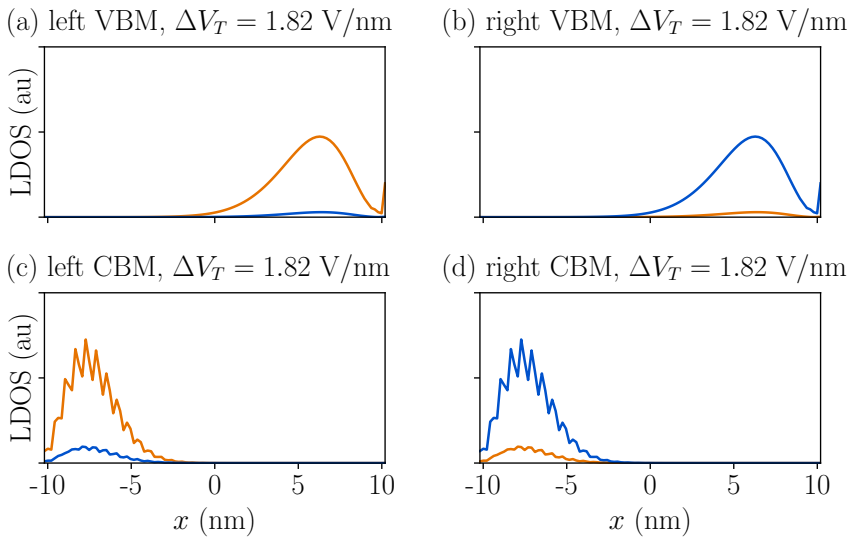


Figure 3.11: LDOS of the valence band maxima for an armchair ribbon of width 20 nm, under transverse bias. The orange and blue lines correspond to spin up and down, respectively.

### 3.5 Conclusion

In summary, we have studied the electronic properties of antimonene nanoribbons, in the presence of out-of-plane and in-plane electric fields, using a tight-binding model. We have shown that there is good agreement between *ab initio* results and the tight-binding model. Our calculations show that antimonene nanoribbons are semiconducting in their bulk, i.e., not taking edge states into account. We have found that, contrary to phosphorene, both kinds of termination, zigzag and armchair, present edge states inside the gap. Under the application of external bias fields, we have demonstrated that the gap can be enhanced by applying an out-of-plane bias. Under a transverse in-plane electric field, the gap decreases. Furthermore, a transverse bias leads to spatial separation between the states forming the edges of the valence and conduction bands. Both types of bias cause valence band splitting, due to Rashba coupling induced by lack of inversion symmetry. Such splitting is accompanied by a different spin polarization of the two mini-valleys at both sides of  $\Gamma$  point.

## CHAPTER 4

# TUNING 2D HYPERBOLIC PLASMONS IN BLACK PHOSPHORUS

Black phosphorus presents a very anisotropic crystal structure, making it a potential candidate for hyperbolic plasmonics, characterized by a permittivity tensor where one of the principal components is metallic and the other dielectric. Here we demonstrate that atomically thin black phosphorus can be engineered to be a hyperbolic material operating in a broad range of the electromagnetic spectrum from the entire visible spectrum to ultraviolet. With the introduction of an optical gain, a new hyperbolic region emerges in the infrared. The character of this hyperbolic plasmon depends on the interplay between gain and loss along the two crystalline directions.

*This chapter is published as: E. van Veen, A. Nemilentsau, A. Kumar, R. Roldán, M.I. Katsnelson, T. Low, S. Yuan, “Tuning Two-Dimensional Hyperbolic Plasmons in Black Phosphorus,” *Physical Review Applied* 12(1), 014011 (2019).*

## 4.1 Introduction

Semiconducting two dimensional (2D) crystals are excellent platforms for tuneable optoelectronics, thanks to their remarkable response to external electrical and mechanical stimuli [45, 13]. In particular, atomically thin black phosphorus [46, 47, 48, 49] (BP) has shown extraordinary tuneability of its optical and electronic properties by several methods [40], like electrostatic gating [50, 51, 52, 53, 54], chemical functionalization [55], quantum confinement (number of layers) [56], external strain [57] or high pressure [58, 59]. This allows the control of light-matter interaction in these materials, in particular the dispersion of collective polaritonic excitations [60].

Apart from being a highly tuneable optoelectronic crystal, the lattice structure of BP is very anisotropic [45, 61]. The in-plane anisotropy implies optical birefringence, of which the extreme limit would be hyperbolicity, where the permittivity tensor has principal components of opposite sign [62, 63, 64, 65]. Recently, in-plane hyperbolicity was implemented experimentally in the GHz frequency range using a metallic metasurface [66]. Moreover, in-plane hyperbolicity in natural van der Waals material  $\alpha$ -MoO<sub>3</sub> was reported and existence of hyperbolic surface polaritons was experimentally verified [67, 68]. The strong anisotropy of BP suggests it has potential as a natural hyperbolic material, offering new possibilities for actively manipulating polaritons in 2D, such as directional plasmons, light emitters, superlensing effects, [65, 69] etc. In this chapter, we demonstrate that atomically thin BP can be tuned to become hyperbolic in a broad spectral range from the entire visible spectrum to the ultraviolet, using electrostatic tuning, strain or thickness. In addition, the presence of a bandgap in excess of the optical phonon energy enables using BP as a possible 2D semiconductor gain medium [70, 71]. With the introduction of population inversion, we show that optical gain results in a new hyperbolic region in the infrared. Finally, we study the behavior of plasmons in both of these hyperbolic regions.

## 4.2 Optical Conductivity and Band Model

We describe BP by means of a  $p_z$ -orbitals tight-binding model fitted to *ab initio* GW methods [72, 73], using the Hamiltonian:

$$H = \sum_{i \neq j} t_{ij} c_i^\dagger c_j + \sum_{i \neq j} t_{p,ij} c_i^\dagger c_j. \quad (4.1)$$

Ten intra-layer  $t_{ij}$  and five inter-layer  $t_{p,ij}$  hopping terms are considered in the model. The obtained band structure corresponds to an anisotropic direct band gap semiconductor, with the gap at the  $\Gamma$  point of the Brillouin zone.

The model can be straightforwardly extended to incorporate electrostatic fields. (Eq. 2.4). Strain (Eq. 2.3) can be incorporated using the dimensionless local electron-phonon coupling  $\beta \approx 4.5$  because this value was proven to give a matching between *ab initio* and tight-binding calculations for the direct-to-indirect bandgap transition under uniaxial strain [74]. The mechanical properties of BP are highly anisotropic, with the zigzag direction being about four times stiffer than the armchair direction [75, 57]. Therefore we use uniaxial strain along the armchair direction for our calculations, accounted for by the strain tensor  $\epsilon_{AC} = \epsilon_{yy} \text{diag}(\nu_z^{AC}, 1, -\nu_z^{AC})$ , where the Poisson ratios  $\nu$  are estimated to be  $\nu_x^{AC} \approx 0.2$ , and  $\nu_z^{AC} \approx 0.2$  [75]. We note the importance to consider the out-of-plane Poisson ratio  $\nu_z$  in our calculations, that accounts for the widening (flattening) of the lattice under compressive (tensile) strain.

The optical conductivity in the zigzag ( $\sigma_{xx}$ ) and armchair ( $\sigma_{yy}$ ) directions is given by the Kubo formula (Eq. 2.8). In that equation, we can replace the Fermi distribution  $f(E)$  with a quasi-equilibrium distribution  $n_F(E, \Delta\mu)$  to introduce population inversion, which will produce optical gain [76, 77]:

$$n_F(E, \Delta\mu) = \theta(E) f\left(E + \frac{E_g}{2} + \Delta\mu\right) + \theta(-E) f\left(E - \frac{E_g}{2} - \Delta\mu\right), \quad (4.2)$$

where  $E_g$  is the band gap and  $\Delta\mu$  is the photo-doping value.

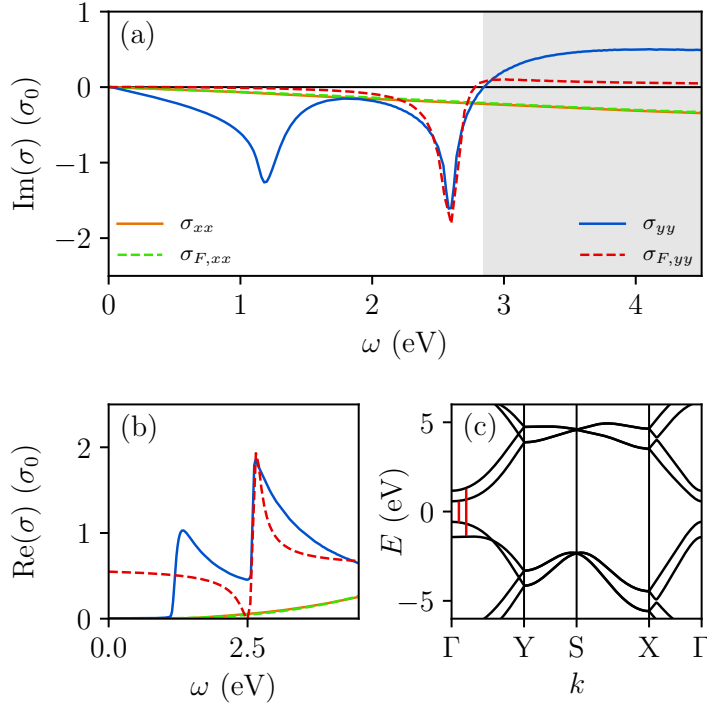


Figure 4.1: (a) The imaginary part of the optical conductivity of bilayer black phosphorus in units of  $\sigma_0 = \frac{\pi e^2}{2h}$ , showing a hyperbolic region (shaded) where  $\text{Im}(\sigma_{xx}) \times \text{Im}(\sigma_{yy}) < 0$ , starting at  $\omega = 2.8$  eV. (b) The real part of the conductivity corresponding to (a). The dashed lines show a fit of the conductivity around the second peak, using the Fano model as described in the text, with resonance width  $\Gamma_{res} = 0.1$  eV, Fano parameter  $q_F = 1.5$  eV $^{-1}$  and  $n = 3$ . (c) The corresponding band structure, with optical excitations indicated in red, causing the two optical peaks at  $\omega = 1.2$  eV and  $\omega = 2.6$  eV.

### 4.3 Hyperbolic Regions

We first define the condition for hyperbolicity. We note that the real part of the dielectric permittivity is proportional to  $\text{Im}(\sigma)$ , a consequence of current continuity. Then, a hyperbolic region appears when

$$\text{Im}(\sigma_{xx}(\omega)) \times \text{Im}(\sigma_{yy}(\omega)) < 0. \quad (4.3)$$

On the other hand,  $\text{Re}(\sigma)$ , is directly proportional to the optical absorption of the free-standing 2D layer. For pristine bilayer BP, the optical conductivity components are plotted in Fig. 4.1. The first thing we observe is that the peculiar puckered structure of BP leads to a strong linear dichroism, i.e., a large difference in optical conductivity for incident polarized light along armchair and zigzag directions [78]. For a bilayer sample, its optical absorption revealed two sharp peaks along the armchair direction, due to the two interband excitations indicated in red in the band structure. These resonant-like features, for light polarized along the armchair direction, has also been observed experimentally [79]. On the contrary, light polarized along the zigzag direction shows a featureless monotonically increasing optical absorption instead. Whereas  $\text{Im}(\sigma_{xx})$  is negative throughout the spectrum,  $\text{Im}(\sigma_{yy})$  goes from negative to positive around  $\omega_h = 2.8$  eV, which results in a hyperbolic region starting at that frequency.

The sign change in  $\text{Im}(\sigma_{yy})$  along the armchair direction is key to the appearance of the hyperbolic region as indicated in Fig. 4.1. This can be traced to the resonant-like feature in the optical absorption  $\text{Re}(\sigma_{yy})$  at  $\omega_{res} = 2.6$  eV. The spectral shape of  $\text{Re}(\sigma_{yy})$  can be described by a Fano resonance curve

$$\sigma_{F,yy} \sim \frac{(q_F \Gamma_{res}/2 + \omega - \omega_{res})^2}{(\Gamma_{res}/2)^2 + (\omega - \omega_{res})^2} \quad (4.4)$$

and setting  $\sigma_{F,xx} \sim \omega^n$ . A fit of these curves to the region around the second peak in the optical conductivity of bilayer BP is shown by the dashed lines in Fig. 4.1. Its Kramers-Kronig pair, which corresponds to  $\text{Im}(\sigma_{yy})$ , reveals a sign change after  $\omega_{res}$ . Hence, we can attribute the origin of hyperbolicity to the strong and anisotropic resonant-like interband transitions.



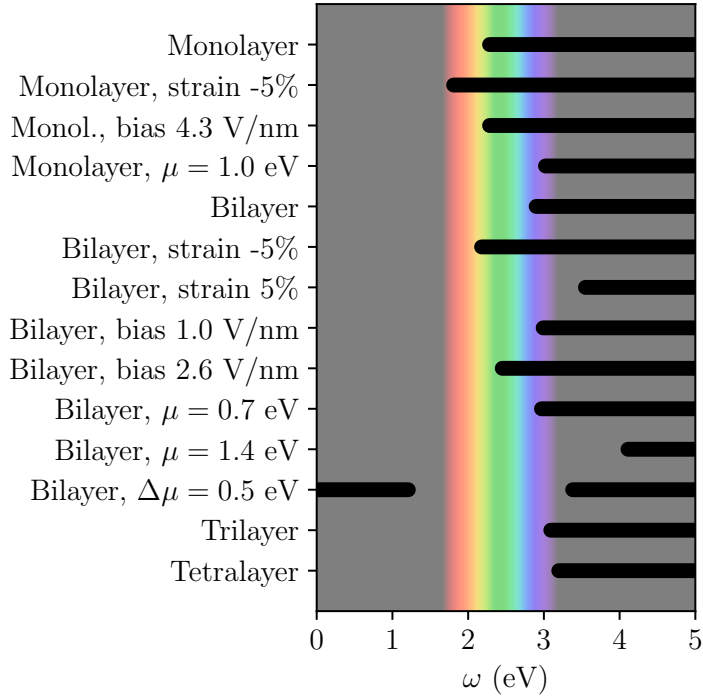


Figure 4.2: The hyperbolic region (indicated in black lines) for different tuning parameters. The visual spectrum is indicated in color.

Since the origin of the hyperbolicity is related to the strong resonant-like anisotropic interband absorption between the largest conduction and valence subband indices, one expects that the spectral range of hyperbolicity can be tuned with band structure engineering. Indeed, the onset of the hyperbolic region  $\omega_h$  can be tuned with the number of layers, strain, bias and doping (Fig. 4.2). Under compressive strain (Fig. 4.3(cd)) the band gap of bilayer black phosphorus becomes smaller. As a result, the optical peaks shift to lower frequencies and  $\omega_h$  goes down. The introduction of bias breaks the mirror symmetry in the  $z$ -direction, which allows for new hybrid

transitions [79], as indicated in the band structure (Fig. 4.3(e)). Moreover, the bands closest to the Fermi energy get pulled closer together, but the next pair of bands get pushed away from one another. This causes the hyperbolic region to go up at first, and then move to lower frequencies as the new peak in the middle gains amplitude. Moreover,  $\omega_h$  goes up for an increasing number of layers, because extra layers add peaks to the optical conductivity in the armchair direction, and the hyperbolic region appears after the last peak. Finally, for increased doping,  $\omega_h$  moves further up, as the first peak becomes less prominent due to Pauli blocking.

If we introduce population inversion (Eq. 4.2, Fig. 4.4), however, the situation becomes qualitatively different: a new hyperbolic region appears in the infrared range. Here, we assume that the quasi-Fermi levels are equal for electrons and holes, and that the electron and hole baths can be described by a common temperature (see Fig. 4.4(c)). Optical pumping [80, 81], where electrons and holes are generated in pairs, in a charge neutral system with particle-hole symmetry, would fit such scenario. The optical gain causes  $\text{Re}(\sigma_{yy})$  to become negative. The spectral window where  $\text{Re}(\sigma_{yy}) < 0$  roughly coincides with  $E_g < \omega < E_g + 2\Delta\mu$ , where there optical transitions between the population inverted electron and hole bands are allowed. In the region up to  $\omega = 1.27$  eV, we find that  $\text{Im}(\sigma_{yy}) > 0$ . In the zigzag direction, the real part of the conductivity also flips sign between  $E_g < \omega < E_g + 2\Delta\mu$ . The imaginary part in this direction, on the other hand, remains negative throughout the entire frequency range, causing a new hyperbolic region in the infrared.

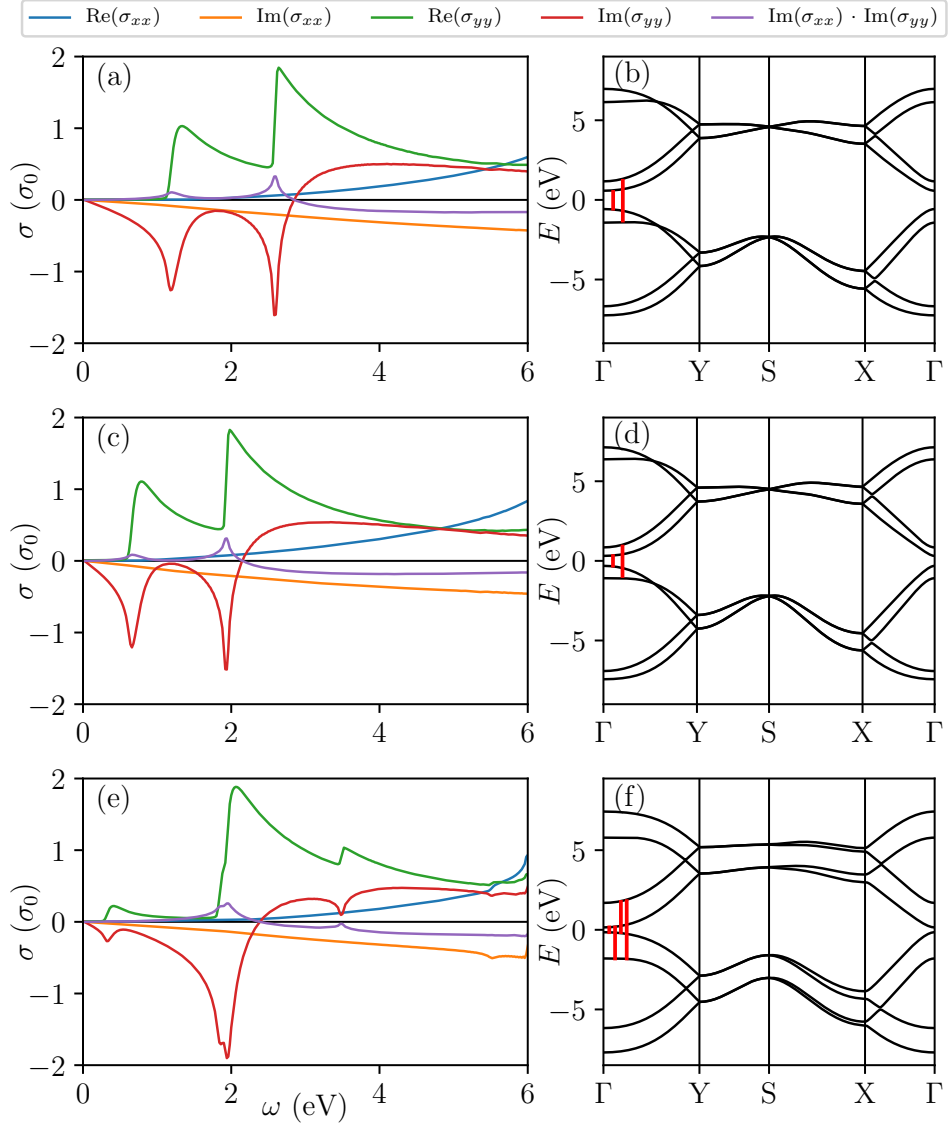


Figure 4.3: The optical conductivity and band structure of bilayer black phosphorus (ab) without strain or bias; (cd) with strain  $\epsilon_{yy} = -5\%$ ; (ef) with a bias of 2.6 V/nm. Optical excitations are indicated in red.

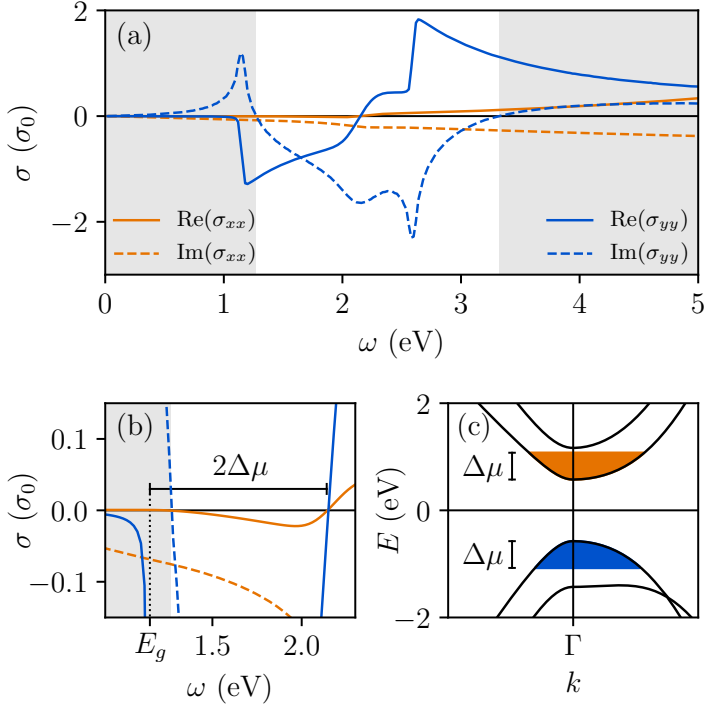


Figure 4.4: (a) The optical conductivity of bilayer black phosphorus with photo-doping  $\Delta\mu = 0.5$  eV. (b) A close-up of the region where  $\text{Re}(\sigma_{yy}) < 0$ , showing a new hyperbolic region (shaded) for  $\omega < 1.27$  eV. (c) The corresponding band structure around the  $\Gamma$ -point, with the population-inverted pockets shown in blue and orange.

## 4.4 Hyperbolic Plasmons.

Finally, let us consider characteristics of plasmons that can be supported by a hyperbolic material. We assume that the plasmon propagates at an angle  $\chi$  with respect to the  $x$ -axis, where the plasmon wavevector takes the form  $\mathbf{q} = q_x \mathbf{e}_x + q_y \mathbf{e}_y + i \mathbf{e}_z \gamma$ , where  $q_x = q_{\parallel} \cos \chi$ ,  $q_y = q_{\parallel} \sin \chi$ ,  $q_{\parallel} = \sqrt{q_x^2 + q_y^2}$ . The dispersion relation for the hyperbolic plasmon takes the form [65, 63]

$$q_{\parallel}^2 = \gamma^2 + k_0^2, \quad (4.5)$$

where

$$\begin{aligned} \gamma = & \frac{ik_0}{2\sigma_{\mathbf{q}\mathbf{q}}} \left[ \left( \frac{2}{\eta_0} + \frac{\eta_0}{2} \sigma_{xx} \sigma_{yy} \right) \right. \\ & \left. + \sqrt{\left( \frac{2}{\eta_0} + \frac{\eta_0}{2} \sigma_{xx} \sigma_{yy} \right)^2 - 4\sigma_{\mathbf{q}\mathbf{q}} \sigma_{\perp\perp}} \right], \end{aligned} \quad (4.6)$$

$k_0^2 = \omega^2 \mu_0 \varepsilon_0$ ,  $\eta_0 = \sqrt{\frac{\mu_0}{\varepsilon_0}}$  is the impedance of free space, and

$$\sigma_{\mathbf{q}\mathbf{q}}(\chi) = \sigma_{xx} \cos^2 \chi + \sigma_{yy} \sin^2 \chi, \quad (4.7)$$

$$\sigma_{\perp\perp}(\chi) = \sigma_{xx} \sin^2 \chi + \sigma_{yy} \cos^2 \chi. \quad (4.8)$$

The iso-frequency contours ( $\omega(q_x, q_y) = \text{constant}$ ), calculated using Eq. (4.5), are presented in Fig. 4.5. We consider the cases of BP with gain ( $\sigma_{xx} = (0.07 - i6.4) \times 10^{-2} \sigma_0$ ,  $\sigma_{yy} = (-0.03 + i0.60) \sigma_0$ ) and BP under strain ( $\sigma_{xx} = (0.20 - i0.31) \sigma_0$ ,  $\sigma_{yy} = (0.20 + i0.54) \sigma_0$ ). It can be seen from Figs. 4.5(a,b) that only in the case of BP with gain the iso-frequency contour resembles a hyperbola with the asymptotes defined as

$$\tan \chi_0 = \sqrt{\left| \frac{\text{Im}(\sigma_{xx})}{\text{Im}(\sigma_{yy})} \right|}. \quad (4.9)$$

For BP under strain, the iso-frequency contour resembles a figure eight shape, even though the hyperbolicity condition (4.3) is met.

This behavior stems from the fact that the hyperbolic shape of the iso-frequency contour is related to the poles of the denominator in Eq. (4.6), defined by zeros of  $\sigma_{\mathbf{q}\mathbf{q}}$  (i.e. when  $\sigma_{\mathbf{q}\mathbf{q}} \rightarrow 0$ , then  $|\gamma| \rightarrow \infty$  and  $|q_{\parallel}| \rightarrow \infty$ ). In particular, it is straightforward to demonstrate that in the case of a purely imaginary conductivity tensor (i.e. no losses or gain) the condition  $\sigma_{\mathbf{q}\mathbf{q}} = 0$  leads to Eq. (4.9) for hyperbola asymptotes.

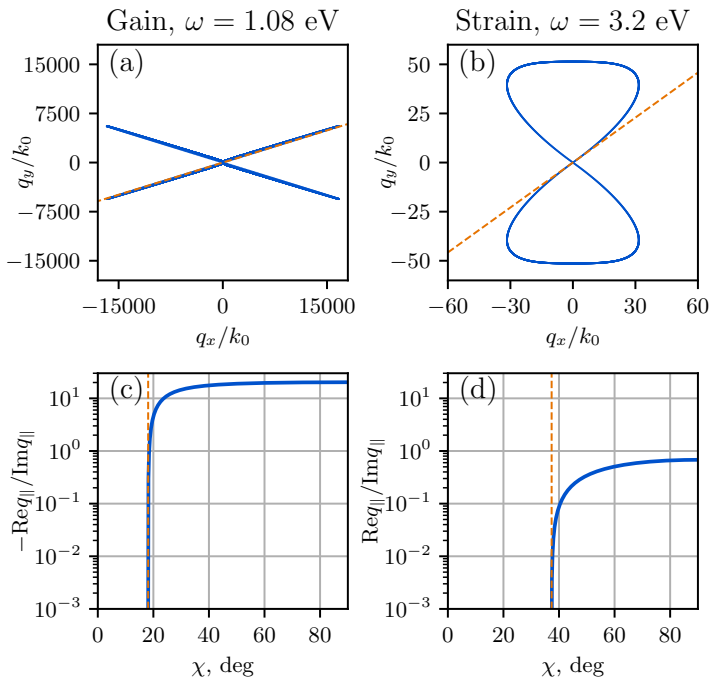


Figure 4.5: Iso-frequency contours and figures of merit for hyperbolic materials with gain ( $\Delta\mu = 0.5$  eV) and strain ( $\epsilon_{yy} = -5\%$ ), calculated using Eq. (4.5). The hyperbola asymptotes (orange dashed lines) are defined using Eq. (4.9).

If the components of the conductivity tensor are both lossy

( $\text{Re}(\sigma_{xx,yy}) > 0$ ) or both have gain ( $\text{Re}(\sigma_{xx,yy}) < 0$ ), the module of the conductivity,  $|\sigma_{\mathbf{q}\mathbf{q}}|$ , is never zero. In fact, for the hyperbola asymptote angle  $\chi_0$ ,  $|\sigma_{\mathbf{q}\mathbf{q}}(\chi_0)| = |\text{Re}(\sigma_{xx})| \cos^2 \chi_0 + |\text{Re}(\sigma_{yy})| \sin^2 \chi_0$ . Thus,  $|\sigma_{\mathbf{q}\mathbf{q}}(\chi_0)|$  increases with the increase of  $|\text{Re}(\sigma_{xx,yy})|$  both for the lossy material and the material with gain. This leads to the decrease of  $q_{\parallel}(\chi_0)$  and, eventually, destroys hyperbolicity when either losses or gain are too high. For example, this is the case in BP with strain presented in Figs. 4.5(b,d). The high losses of the material in the hyperbolic regime lead to the hyperbola folding into a figure eight shape iso-frequency contour. Moreover, the plasmons itself are very lossy in this case as is quantified by ratio  $\text{Re}q_{\parallel}/\text{Im}q_{\parallel}$  in Fig. 4.5d.

The case where one of the components of the conductivity tensor is lossy ( $\text{Re}(\sigma_{xx}) > 0$ , while the other has gain ( $\text{Re}(\sigma_{yy}) < 0$ ), requires separate consideration. In this case,  $\sigma_{\mathbf{q}\mathbf{q}}(\chi_0) = |\text{Re}(\sigma_{xx})| \cos^2 \chi_0 - |\text{Re}(\sigma_{yy})| \sin^2 \chi_0$ . When both the losses and the gain are small, then  $|\sigma_{\mathbf{q}\mathbf{q}}(\chi_0)|$  is small as well which allows for the iso-frequency contour to preserve the hyperbolic shape, as is the case for BP with gain presented in Fig. 4.5(a,c). This is, however, a rather trivial case which can be observed in pure lossy materials when the losses are small [65]. A non-trivial property of a material with gain is that  $\sigma_{\mathbf{q}\mathbf{q}} = 0$ , when  $\tan \chi_0 = \sqrt{|\text{Re}(\sigma_{xx})|/|\text{Re}(\sigma_{yy})|}$ . That condition, together with Eq. (4.9), indicates that the iso-frequency contour preserves its hyperbolic shape for arbitrary large losses and gain, as long as the following holds true,

$$\sigma_{xx} = -\sigma_{yy} \tan \chi_0. \quad (4.10)$$

This criterion can be verified through its iso-frequencies contours. To illustrate this, we choose BP under strain, and assume that a gain was added to the  $y$ -component of the BP conductivity, with the gain values ( $\text{Re}(\sigma_{yy})$ ) indicated in the legend of Fig. 4.6. Due to high losses, the iso-frequency contour of BP under strain does not resemble a hyperbola. Countering the high losses with high gain is not beneficial for restoring the hyperbolic plasmons (see Fig. 4.6(a)) as this leads to a high magnitude of  $\sigma_{\mathbf{q}\mathbf{q}}$ . However, we can recover the hyperbolic mode by matching  $\sigma_{xx}$  to  $\sigma_{yy}$  using Eq. (4.10), as can be see from Fig. 4.6(b) ( $\text{Re}(\sigma_{yy}) = -0.33\sigma_0$ ). A

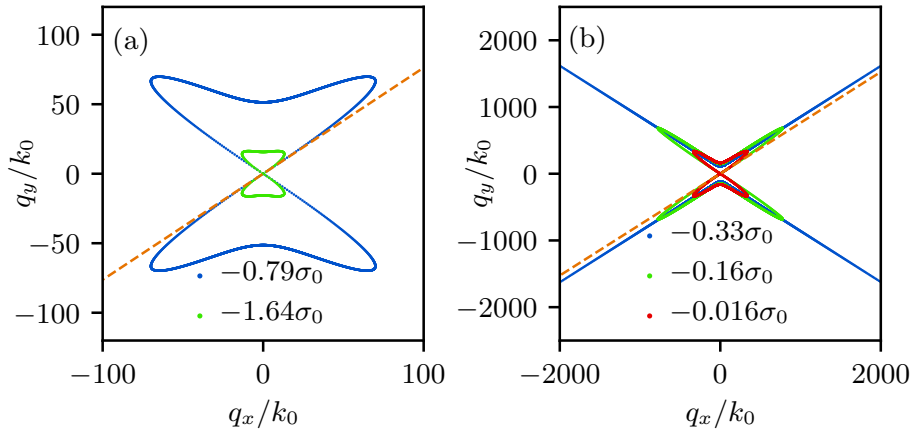


Figure 4.6: Iso-frequency contours for hyperbolic materials with different values of gain.  $\sigma_{xx} = 0.20 - i0.31\sigma_0$ ,  $\sigma_{yy} = \text{Re}(\sigma_{yy}) + i0.54\sigma_0$ .  $\text{Re}(\sigma_{yy})$  is indicated in the legend on the panels (a), (b).

further decrease of gain breaks the resonance condition (4.10) and leads to distortion of the hyperbola ( $-0.16\sigma_0$  and  $-0.016\sigma_0$  in Fig. 4.6(b)).

## 4.5 Conclusion

In conclusion, we showed how black phosphorus can be made hyperbolic across a broad spectral range, in particular in the visible wavelengths. We have shown how the spectral location of these hyperbolic regions can be tuned via electrostatic bias and strain. We also studied the influence of optical gain on the hyperbolic plasmons and showed the appearance of a new hyperbolic region in the infrared. The ease with which these plasmons can be tuned opens up new opportunities for 2D nanophotonics.





## CHAPTER 5

# QUANTUM TRANSPORT IN SIERPINSKI CARPETS

Recent progress in the design and fabrication of artificial 2D materials paves the way for the experiments on electron systems moving on complex geometries, such as plane fractals. In this chapter, we calculate the quantum conductance of a 2D electron gas roaming on a Sierpinski carpet – a plane fractal with Hausdorff dimension intermediate between one and two. We find that the fluctuations of the quantum conductance as a function of energy are a fractal graph. Its dimension can be chosen by changing the geometry of the Sierpinski carpet. This behavior is independent of the underlying lattice geometry.

*This chapter is published as: E. van Veen, S. Yuan, M.I. Katsnelson, M. Polini, A. Tomadin “Quantum transport in Sierpinski carpets,” Physical Review B 93, 115428 (2016).*

## 5.1 Introduction

Recently a variety of experimental protocols have become available, that can be used to create artificial 2D lattices for electrons, atoms, and photons. For example, schemes for creating artificial hexagonal lattices [82] allowed to observe a wealth of interesting phenomena, such as Mott-Hubbard split bands [83], massless Dirac fermion behavior modified by pseudo-electric and pseudo-magnetic fields [84], and photonic Floquet topological insulating states [85]. In the case of ultracold atomic gases loaded in hexagonal optical lattices, recent progress has even led to an experimental study [86] of the Haldane model [87].

More generally, in the context of solid-state implementations, a combination of e-beam nanolithography, etching, and metallic gate deposition [88, 89, 90, 91, 92, 93, 94] can yield high-quality 2D patterns with arbitrary, non-periodic shape in semiconductor heterostructures (such as GaAs/AlGaAs) hosting ultra-high mobility 2D electron gases (EGs). Ultimately, these procedures yield an external potential landscape with the desired geometry that acts as a potential well to trap electrons. Synthetic solid-state quantum materials can also be created by utilizing scanning probe methods [84].

Most notably, recently a Sierpinski gasket was made on the nanometer scale by controlled positioning of CO molecules on a copper surface using scanning tunneling microscopy [95].

Another way to improve spatial resolution is by using bottom-up nanofabrication methods such as nanocrystal self-assembly [96]. Both the local electronic structure [97] and the geometry of the system [98] can be designed by careful choices of precursor molecules and reaction parameters. In particular, usage of building blocks with chiral bondings on a substrate with a compatible symmetry allowed the assembly of molecular Sierpinski gasket (SG) fractals [98]. These experimental achievements motivate the theoretical investigation of complex 2D structures, with the aim of discovering novel transport and optical features which could enable or improve technological applications.

In this chapter, we present a theoretical study of the transport prop-

erties of a 2D electron gas (2DEG) in a Sierpinski carpet (SC), which is a 2D self-similar structure [99]. Macroscopically, the self-similarity of the SC is quantified by the fact that its Hausdorff dimension [99]  $d_H$  (i.e. a generalization of the topological dimension) is between one (a line) and two (a plane), which makes the SC a fractal [100]. By varying the parameters  $\mathcal{N}$  and  $\mathcal{L}$  of the geometrical construction of the fractal, a family of SCs with different dimensions can be generated. At a microscopic level, any physical realization of a 2DEG in a SC will involve electrons hopping on a lattice. Here, we have considered three different underlying lattice structures, i.e. triangular, square, and hexagonal lattices. The latter case is particularly relevant, since it models a top-down nanofabricated SC obtained by etching a graphene sheet.

Contrary to electrons hopping on Bloch translationally-invariant lattices, the SC hosts both extended and localized electronic states in narrow energy ranges. Phase-coherent electronic transport through the SC, thus, depends on the carrier energy and on the geometric matching between lead positions and profiles of the extended electronic states, depending on the lead positions and their widths, and displays fractal fluctuations [101, 102, 103, 104, 105] as a function of energy, in the absence of a magnetic field. We will also find that extended states, which are responsible for large conductance values, are quite robust to elastic disorder.

Whereas the vast majority of the literature on fractal conductance fluctuations (CFs) considers geometrically simple structures such as billiards, here we find that, in a SC, the fractal dimension of the sample determines the fractal dimension of the CFs.

While brownian motion and the heat diffusion equation on fractal geometries have been extensively studied in the literature [106, 107, 108], the transport properties of electrons roaming on such complicated geometrical structures have comparatively received less attention. More precisely, some analytical [109, 110] and numerical [111, 112, 113, 114] studies of the conductance of electrons in Sierpinski fractals have appeared in the literature. We stress that the problem of quantum particles moving in a SC is very different from that of a quantum particle displaying a self-similar spectrum. Such problems are very well studied in physics, a paradigmatic

example being that of the Hofstadter butterfly spectrum [115] displayed by an electron moving in 2D under the combined effect of a periodic potential and a perpendicular magnetic field. Finally, we are not interested in the statistical distribution of eigenvalues and the nature of the corresponding eigenstates of electrons in plane fractals, which have been studied in detail [116, 117, 118, 119, 120]. Rather, our aim is to unveil fundamental dc transport characteristics, which can be measured in artificially-fabricated SCs with current technology.

## 5.2 Method

We model a 2DEG in a SC by means of a single-orbital tight-binding Hamiltonian:

$$H = -t \sum_{\langle i,j \rangle, \sigma} c_{i,\sigma}^\dagger c_{j,\sigma}. \quad (5.1)$$

This Hamiltonian describes electrons with spin  $\sigma = \uparrow, \downarrow$  hopping between the nearest-neighbor sites  $\langle i, j \rangle$  of a SC. Nanopatterning a SC on the surface of a semiconductor hosting a high mobility 2DEG is expected [83, 88, 89] to yield  $t$  of the order of a few meV, while protocols based on STM manipulation [84] are expected to yield  $t \sim 100$  meV. For the sake of simplicity, we ignore magnetic fields and electron-electron interactions, which are expected to lead to very interesting quantitative and qualitative effects. Conductance and wave function calculations are performed using KWANT [6].

## 5.3 Fractal geometry

Fractals are made using an iterative process. We can either take a top-down approach (which corresponds to using etching techniques) or a bottom-up approach (corresponding to for example self-assembly). Taking the bottom-up approach, to make a standard SC, a previous iteration is copied  $\mathcal{N} = 8$  times to make a next iteration that is  $\mathcal{L} = 3$  times wider (Fig. 5.2). The Hausdorff dimension is then given by  $d_H = \log_{\mathcal{L}} \mathcal{N}$ . It describes the scaling behavior of the fractal, and gives a measure of how space-filling it is.

Each discretized SC is characterized by the iteration step  $I$ , its underlying lattice structure (square, triangular, or hexagonal), the lattice constant  $a$ , and either its total width in unit cells  $W$  (in the case of top-down construction – see Fig. 5.1) or the size of its starting square  $S$  (in the case of bottom-up construction – see Fig. 5.2). For the square lattice SC, these last two numbers are related with  $W = S \times 3^I$ .

For comparison, we will also consider fractals other than the SC, namely the Sierpinski gasket (SG) and Vicsek fractals [117, 121], as shown in Fig. 5.2. For the standard carpet  $d_H \approx 1.89$ , for the gasket  $d_H \approx 1.58$  and for the Vicsek fractal  $d_H \approx 1.46$ .

Fig. 5.3 shows the different lead configurations. The leads always have the same width as the starting cell  $S$ , or on the top-down case, the same width as the narrowest channel in the scattering region itself.

Fig. 5.4 shows how to generate SCs with different dimensions. Panel (a) corresponds to  $\mathcal{N} = 8$  and  $\mathcal{L} = 3$  with dimension  $d_H \approx 1.89$ . (b) corresponds to  $\mathcal{N} = 12$  and  $\mathcal{L} = 4$  with dimension  $d_H \approx 1.79$ .

We have calculated the energy dependence of the two-terminal conductance  $G(E)$  of the tight-binding model (5.1) for a configuration with centered leads and with diagonal leads. We first focus on the simplest case of the square lattice SC. Then we present results on the triangular and hexagonal lattices, and finally we move on to the SG and Vicsek fractal.

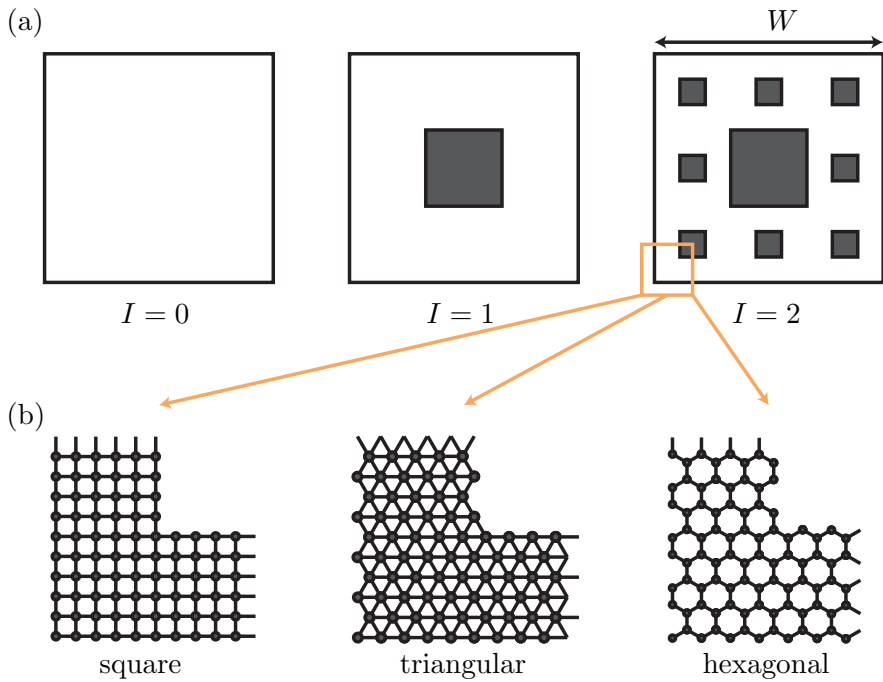


Figure 5.1: (a) Top-down construction of a SC. The black squares represent regions that are *removed* from the white sample at iteration  $I = 0$ . At the  $I$ -th iteration we remove  $\mathcal{N}$  copies of the regions removed at the  $(I - 1)$ -th iteration, after scaling them down in linear size by a factor  $\mathcal{L}$  (here  $\mathcal{N} = 8$  and  $\mathcal{L} = 3$ ). For a number of iterations  $I \gg 1$  we obtain an approximation of the SC. (b) The square, triangular and hexagonal underlying lattices considered in this chapter. The width of the sample is  $W$  unit cells.

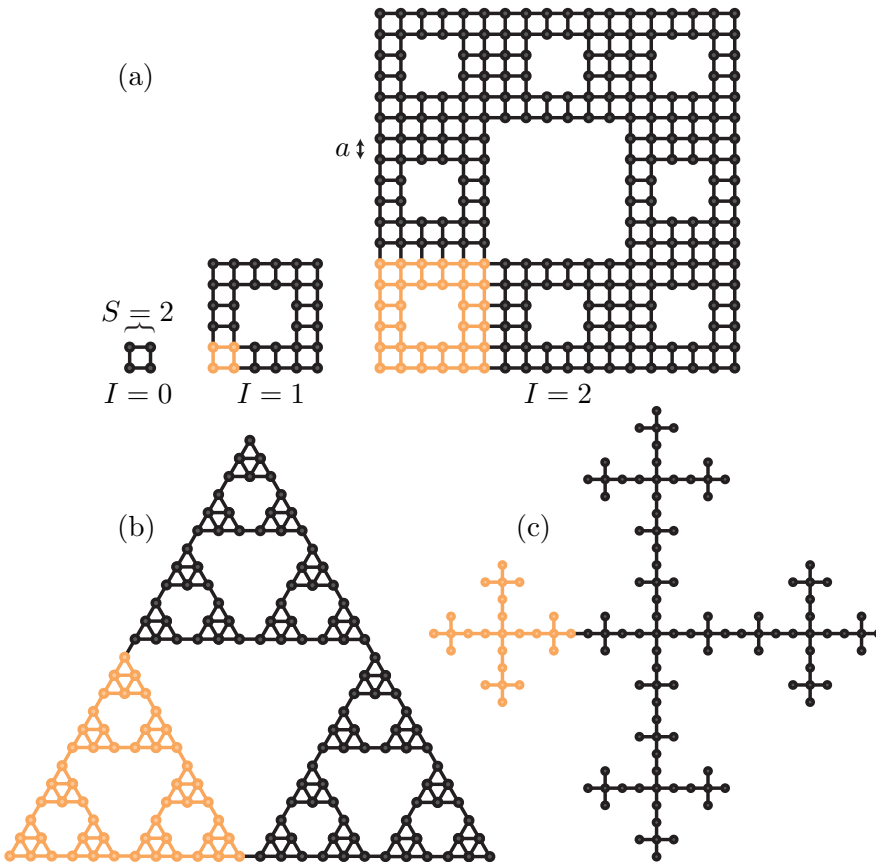


Figure 5.2: (a) Bottom-up construction of a SC with base size  $S = 2$ . (b) Iteration  $I = 3$  of the Sierpinski gasket with base size  $S = 3$  and (c) iteration  $I = 3$  of the Vicsek fractal with base size  $S = 1$ . For each iteration  $I$ , the previous iteration  $I - 1$  is shown in orange; the lattice constant is  $a$ .



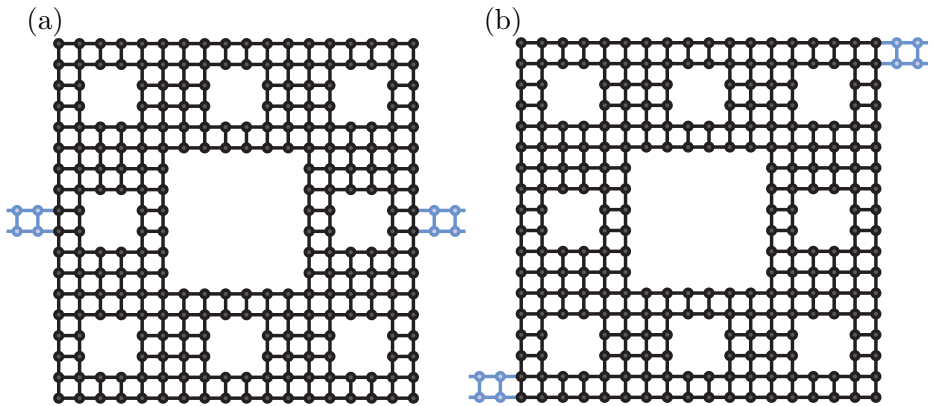


Figure 5.3: SCs with (a) centered and (b) diagonal leads (shown in blue).

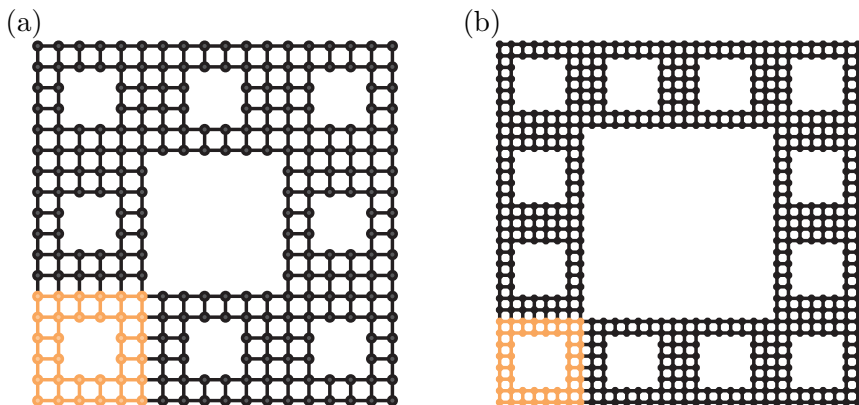


Figure 5.4: Construction of SCs with different Hausdorff dimensions: (a)  $d_H \approx 1.89$  and (b)  $d_H \approx 1.79$ .

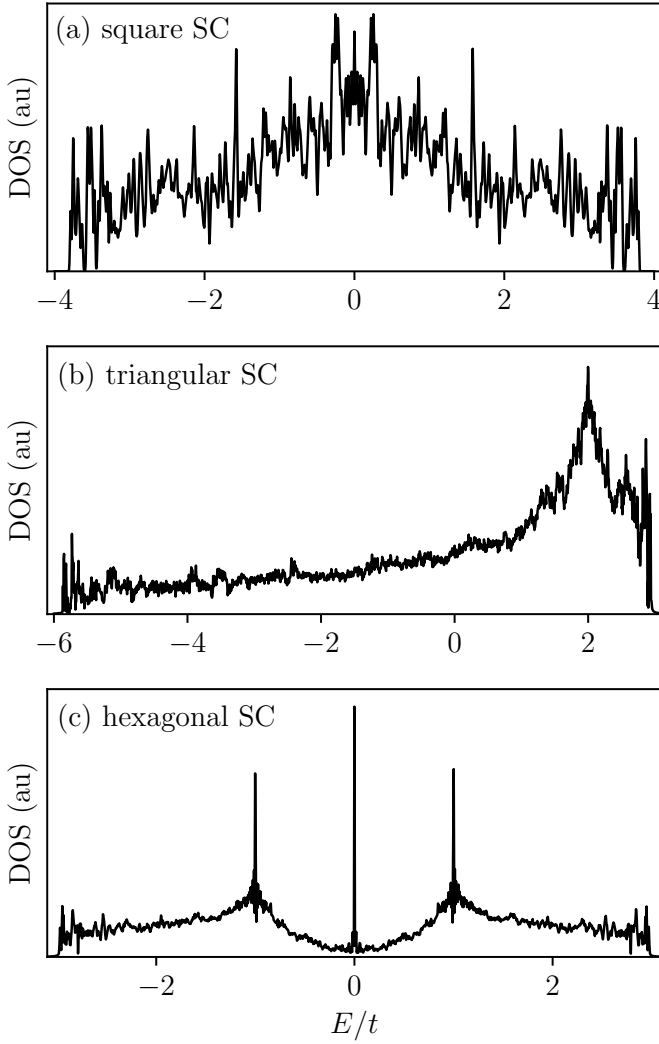


Figure 5.5: density of states of SCs with different underlying lattices for an SC with  $\mathcal{N} = 8$  and  $\mathcal{L} = 3$ . (a) Square  $I = 4, W = 162$ , (b) triangular,  $I = 4, W = 284$  and (c) hexagonal with  $I = 4, W = 284$ .

## 5.4 Results

### 5.4.1 Density of states

For small systems, the density of states is obtained by exactly calculating the Hamiltonian eigenvalues. For large systems with more than  $10^5$  sites, we use the tight-binding propagation method (Eq. 2.35).

Fig. 5.5 shows the density of states of SCs for different lattice geometries. Because of the absence of translational invariance, it is not possible to represent the eigenvalues of the Hamiltonian in terms of a conventional band structure diagram. A few general observations can still be made on the spectrum of the Hamiltonian. On the square lattice, the Hamiltonian is particle-hole symmetric and the spectrum of eigenvalues extends from  $-4t$  to  $4t$  for a bandwidth equal to  $8t$ . The Hamiltonian on the honeycomb lattice is also particle-hole symmetric, and its eigenvalues range from  $-3t$  to  $3t$ . Notably, the density of states does *not* display a gap in this case, but instead a edge state peak at  $E = 0$ . This is at odds with the case of antidot lattices created by piercing a hexagonal lattice with regularly spaced holes [122], where a gap is opened up in the well-known graphene-like density of states. On the triangular lattice, eigenenergies range from  $-6t$  to  $3t$ .

### 5.4.2 Conductance

The quantum conductance  $G$  of a square-lattice SC as a function of energy  $E$  is shown in Fig. 5.6. We show an energy range smaller than the whole bandwidth to distinguish the single peaks in the profile. In an experimental situation, the energy  $E$  is determined by the gate potential. In panel (a) we clearly see that the two-terminal conductance  $G(E)$  is equal to  $4e^2/h$  for  $E = 0$ , where a conductive extended state is present [109]. This is because, with central lead positions, electrons of a given spin injected on the left side of the SC can reach the right side by following two equivalent paths, Fig. 5.7(a), each carrying a conductance quantum, without being backscattered by the inner holes of the SC. On the other hand, as we can

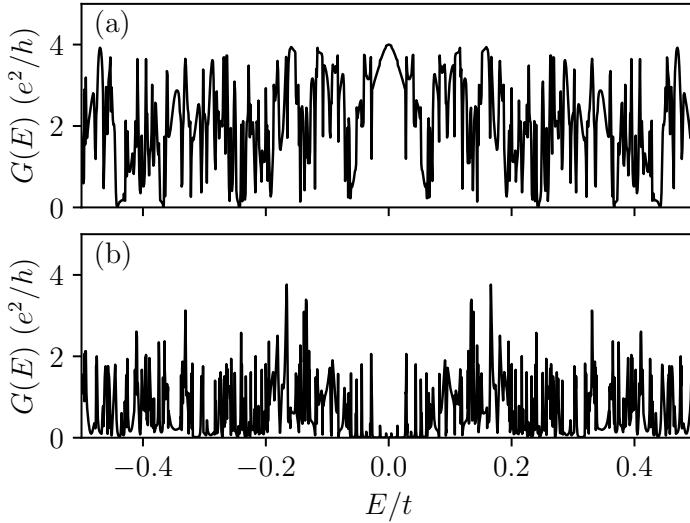


Figure 5.6: Energy dependence of the conductance  $G(E)$  of a square-lattice SC with  $\mathcal{N} = 8$ ,  $\mathcal{L} = 3$ ,  $I = 3$ , and  $W = 54$  for (a) central and (b) diagonal lead positions.

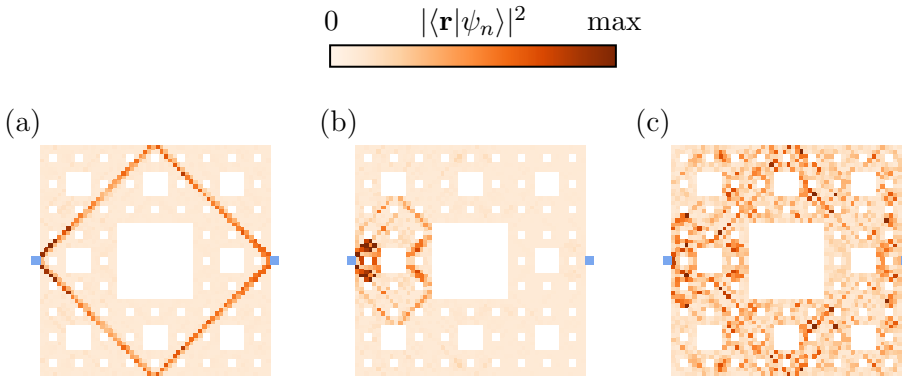


Figure 5.7: Three examples of scattering wave functions in the SC at (a)  $E=0.02t$ , (b)  $E=0.06t$  and (c)  $E=0.08t$ .

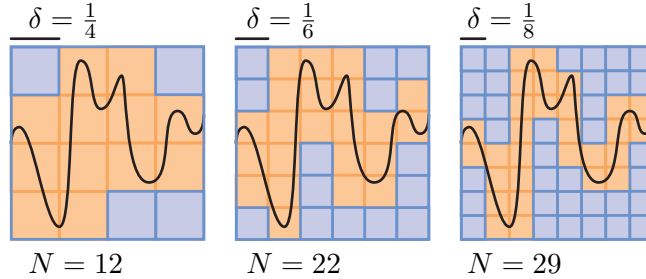


Figure 5.8: An illustration of the box-counting algorithm.

see from Fig. 5.6(b), the SC can be insulating (i.e.  $G = 0$ ) at the same energy, when probed with leads in a diagonal configuration, which do not couple to the conducting state.

### 5.4.3 Box-counting algorithm

The roughness of the CF graph increases with the iteration step  $I$  of the construction of the SC. As  $I$  is increased, finer and finer CFs appear, at progressively smaller energy scales. This suggests that the CF graph is actually a fractal, with a dimension larger than its topological dimension (one). The dimension of the CF graph can be quantified by using a box-counting (BC) algorithm [103]. This algorithm counts the number  $N$  of squares of size  $\delta$ , which are necessary to continuously cover the graph of  $G(E)$  (in units of  $e^2/h$ ) rescaled to a unit square (see Fig. 5.8). In general, points in the plane  $(\log N, -\log \delta)$  are expected to fall in *three* distinct regions. For large values of  $\delta$ , the squares are too large to distinguish the features of the graph and  $N$  grows slowly as  $\delta$  decreases. For very small values of  $\delta$ , the squares are so small that they resolve the single points in the set of data belonging to the CF graph: in this case  $N$  is expected to saturate to the number  $N_s$  of points in the energy mesh where  $G(E)$  is evaluated. Finally, there is an intermediate region (usually called “scaling region”) where scaling is linear in a log-log plot, i.e. where  $N \sim \delta^{-d}$ . The

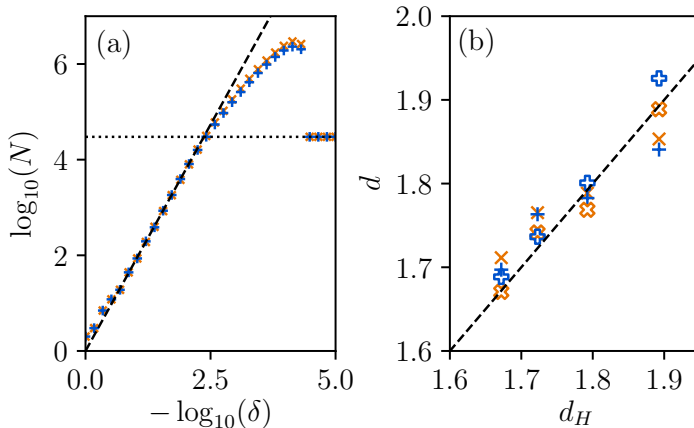


Figure 5.9: (a) BC algorithm analysis of the conductance fluctuations for SCs with  $I = 4$ , and  $W = 162$ , for central (blue, +) and diagonal (orange,  $\times$ ) leads. The horizontal dotted lines represent the saturation value  $N = N_s$ , with  $N_s = 3 \times 10^4$ . The slope of the dashed line has been set equal to the Hausdorff dimension  $d_H \approx 1.89$  of the SC. (b) BC dimension  $d$  of the conductance fluctuations for square-lattice SCs with different dimensions for  $I = 3$ ,  $S = 2$  (solid markers) and  $I = 4$ ,  $S = 2$  (outlined markers), for central (blue, +) and diagonal (orange,  $\times$ ) leads. The dashed line represents  $d = d_H$ .

slope  $d$  in the scaling region is the BC estimate of the dimension of the CF.

In Fig. 5.9, we show the results of the BC algorithm for the CFs of a square-lattice SC with  $\mathcal{N} = 8$  and  $\mathcal{L} = 3$ . The analyzed CFs clearly show a fractal dimension  $1 < d < 2$  over a scaling region of more than two orders of magnitude. The fractal nature of the CF graph stems from the coexistence of extended and localized electron wavefunctions in narrow energy ranges [101, 103]. We stress that localized electron wavefunctions emerge in our SC, and even in the much simpler Sierpinski gasket [117] (see below), in the absence of elastic disorder, because of scattering of electrons

against the inner holes of the SC. Most importantly, we find that the results of the BC algorithm are independent of the lead positions. This allows us to claim that the dimension of the CF graph is an *intrinsic* property of the sample geometry.

In Fig. 5.9(b), we show the BC algorithm estimate of the fractal dimension  $d$  for SCs with different dimensions. BC algorithm analyses for  $I = 3$  or  $I = 4$ , or for different lead configurations, yield values of  $d$  which differ by a few percent. However,  $d$  substantially depends on the Hausdorff dimension  $d_H$  of the SC. A reasonable conjecture, supported by our numerical results, is that  $d = d_H$  for  $I \gg 1$ . It is remarkable that the analysis of CFs carries information on the SC geometry, down to very small length scales. Conversely, these results show that it is possible to fix the fluctuation spectrum of the quantum conductance by choosing an appropriate SC. This evidence that the fractal dimension of the sample determines the fractal dimension of the CF graph is the main result of this chapter.

Fig. 5.10 details how the data from the BC algorithm is used to calculate the BC dimension. Our estimate for the BC dimension is obtained by a best-fit procedure to the set of points  $(-\log_{10}(\delta), \log_{10}(N))$  given by the BC algorithm. Here,  $N$  is the number of boxes of size  $\delta$  needed to cover the graph of a conductance fluctuation curve. We point out that we always rescale the conductance curves to the unit square  $[0, 1] \times [0, 1]$  before the analysis is applied.

The linear fit to the data is performed in an interval centered in the scaling region. The extent  $\Delta \log_{10}(\delta)$  of the fitting interval is then changed to provide several different best-fit results. The whole scaling region has an extent  $\Delta \log_{10}(\delta) \simeq 2.5$ .

The results presented in Fig. 5.9 correspond to the average of the values  $d$  as the extent of the fitting interval is changed. Panel (a) shows the BC dimension  $d$  as a function of the extent  $\Delta \log_{10}(\delta)$  of the interval where the linear fit is calculated. Panel (b) shows the relative difference between the calculated BC dimension  $d$  and the expected value  $d_H$ . In both panels, orange (blue) data corresponds to  $\mathcal{N} = 8$  and  $\mathcal{L} = 3$  ( $\mathcal{N} = 12$  and  $\mathcal{L} = 4$ ) with  $I = 4$  and  $W = 162$  ( $W = 512$ ). The result of the linear fit is very robust as we change the extent of the fitting interval to cover the entire

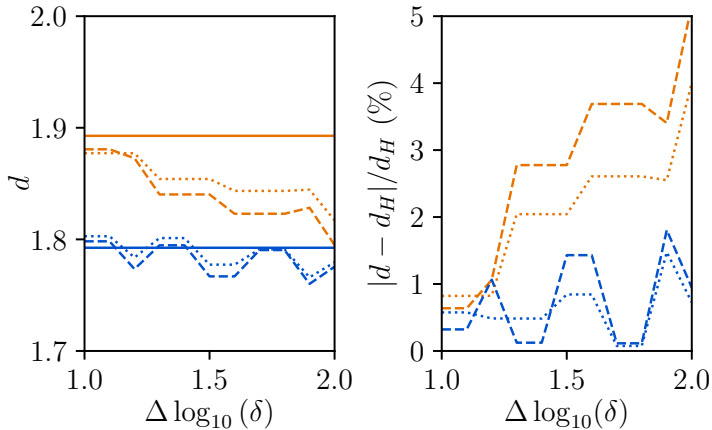


Figure 5.10: Estimation of the fractal dimension from the BC analysis for square SCs with  $d_H \approx 1.89$  (blue) and  $d_H \approx 1.79$  (orange). The results for central leads are shown in dashed lines, dotted lines correspond to diagonal leads. (a) BC dimension  $d$  as a function of the extent  $\Delta \log_{10}(\delta)$  of the interval where the linear fit to the BC data is calculated. The orange (blue) solid line corresponds to the conjectured value  $d_H = 1.89$  ( $d_H = 1.79$ ). (b) Relative difference between the calculated BC dimension  $d$  and the expected value  $d_H$ .

scaling region, over more than two orders of magnitude. The estimate of the dimension obtained with the linear fit matches the expected value  $d_H$  (i.e. the dimension of the SC) with an accuracy of a few percent in the whole scaling region.

In Fig. 5.11, we test the generality of our findings by extending our numerical analysis to SCs with underlying triangular and hexagonal lattices. From Figs. 5.11(a) and (b) we clearly see that the conductance graphs of triangular- and hexagonal-lattice SCs are strikingly different from each other and from the conductance graph of square-lattice SCs. A gap appears in the conductance spectrum  $G(E)$  of the hexagonal-lattice SC, where the



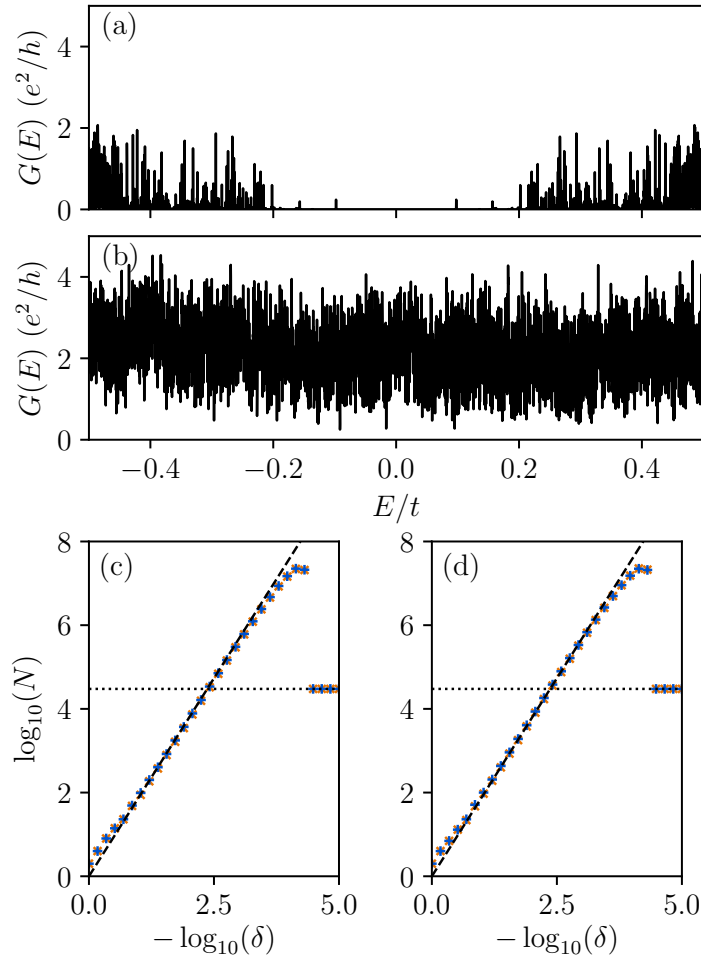


Figure 5.11: Conductance graphs for a center-lead configuration (a) hexagonal-lattice SC with  $\mathcal{N} = 8$ ,  $\mathcal{L} = 3$ ,  $I = 4$ , and  $W = 284$ ; (b) triangular-lattice SC with  $\mathcal{N} = 8$ ,  $\mathcal{L} = 3$ ,  $I = 4$ , and  $W = 284$ . Also shown, the corresponding BC algorithm analyses for (c) the hexagonal-lattice SC and (d) the triangular-lattice SC. Results for both center (blue, +) and diagonal (orange,  $\times$ ) leads are shown.

conductance vanishes entirely. We point out, however, that the corresponding density of states of the hexagonal-lattice SC does not display a gap.

It is remarkable that, despite the different appearances, the conductance fluctuations in all three cases yield very similar BC algorithm results. In particular, the estimated BC dimension of triangular- and hexagonal-lattice SCs is compatible with our conjecture  $d = d_H$ .

#### 5.4.4 Persistence of conductive states in disordered SCs

Fig. 5.12(a) shows the energy dependence of the conductance  $G(E)$  of a square-lattice SC in the presence of localized elastic disorder. A single-site vacancy is created along the path of the conductive state shown in Fig. 5.7(a). We see that, despite such a strong, localized disorder source,  $G(E)$  still reaches its maximum value  $G(E) = 4e^2/h$  at  $E = 0$ .

Fig. 5.12(b) shows  $G(E)$  in the presence of smooth elastic disorder. The following potential term has been added to the Hamiltonian:

$$V = \sum_{i,\sigma} \mu(\mathbf{r}_i) c_{i,\sigma}^\dagger c_{i,\sigma} . \quad (5.2)$$

The profile  $\mu(\mathbf{r}_i)$ , shown in Fig. 5.12(c), varies on a substantial energy scale, fixed to 20% of the hopping amplitude. When compared to the conductive bulk path in the absence of disorder, shown in Fig. 5.7, we see that the profile of the eigenstate is surprisingly robust. More precisely, we notice a weak hybridization with localized wavefunctions at the corners of the SC, but the main bulk paths of the unperturbed conductive wavefunction are clearly visible and connect the left and right side of the SC, where the leads are located. This explains why the conductance around  $E = -0.063t$  almost reaches its maximum value. We conclude that the conductance of the 2DEG in a SC is robust with respect to both localized and smooth elastic disorder.

For a geometry with a smooth disorder potential varying on an energy scale up to 20% of the hopping amplitude, we have verified that the conductance fluctuations display a fractal dimension which is comparable to that in the clean SC and is weakly dependent on the strength of the potential.

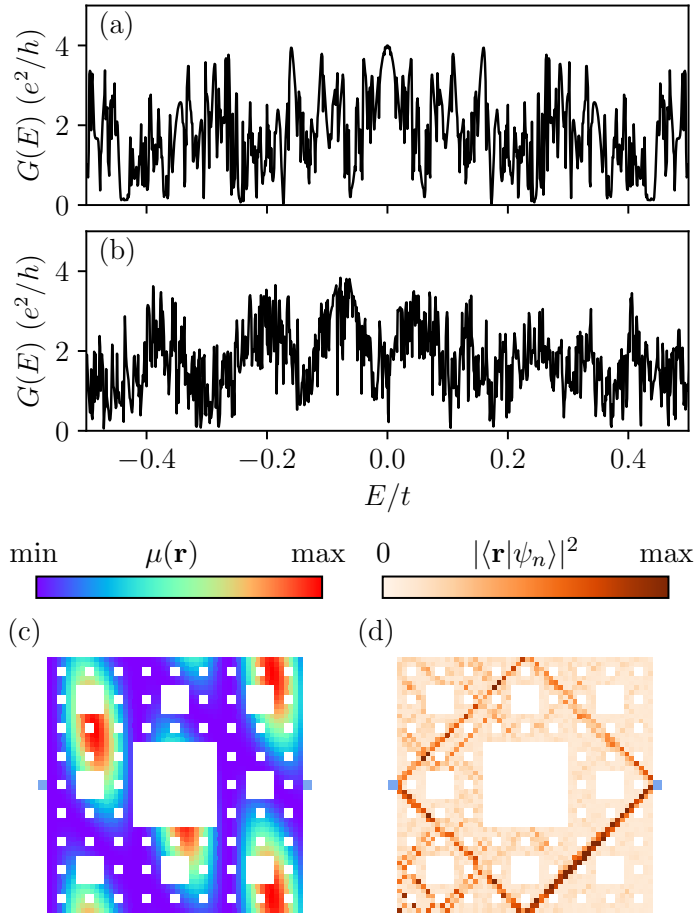


Figure 5.12: (a) Conductance of a square-lattice SC, with a single-site vacancy with spatial coordinates  $\mathbf{r}_i = (10a, 18a)$ . (b)  $G(E)$  in the presence of the smooth elastic potential  $\mu(\mathbf{r}_i)$  shown in (c). The colorscale in (c) varies from  $-0.1t$  (blue) to  $+0.1t$  (red). (d) conductive eigenstate at energy  $E = -0.063t$  in the presence of the smooth elastic potential.

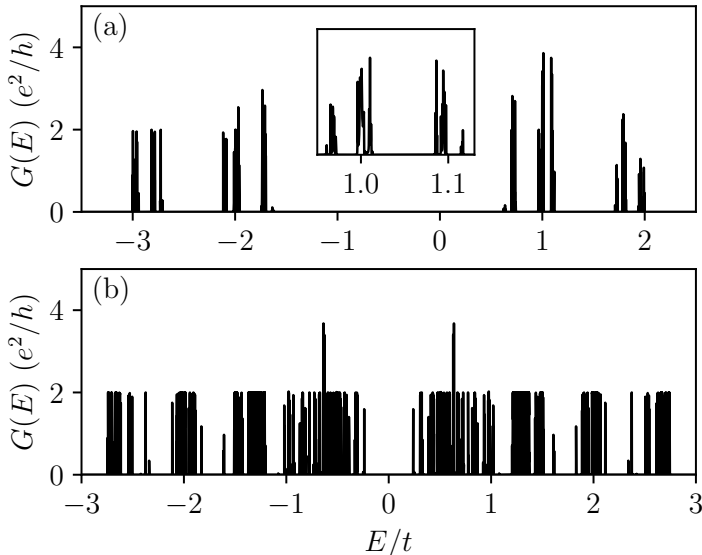


Figure 5.13: Energy dependence of the conductance  $G(E)$  (in units of  $e^2/h$ ) for: (a) the Sierpinski gasket with  $I = 8$  and  $W = 256$  and (b) the Vicsek fractal with  $I = 6$  and  $W = 1458$ . The inset in (a) shows a magnification of the cluster of peaks around  $E/t \sim 1$ .

### 5.4.5 Other fractals

Finally, to shed further light on the origin of the fractal CFs, we calculate the quantum conductance of two fractals which do not belong to the family of SCs. The BC algorithm analysis applied to the CFs of the gasket and Vicsek fractal as shown in Fig. 5.2(b,c). We see that both geometries feature fractal CFs, but the difference between  $d$  and  $d_H$  in the case of the gasket and Vicsek fractal is sizable contrary to the case of a SC. For increasing  $I$ , the box counting dimension of the conductance fluctuations of the gasket converges to  $d = 1.22$  ( $d_H = 1.58$ ), and for the Vicsek fractal to  $d = 1.69$  ( $d_H = 1.46$ ). Moreover, the gasket and Vicsek fractals show

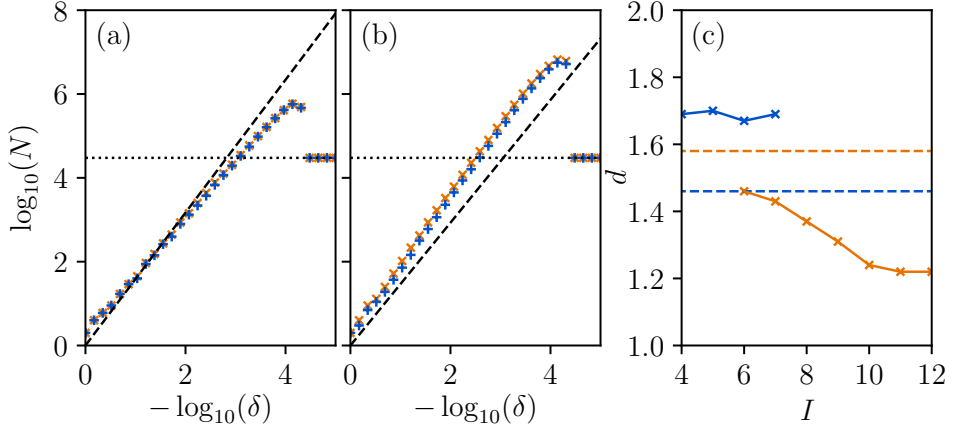


Figure 5.14: BC analysis for (a) a gasket with  $I = 8$  and  $W = 256$  and (b) a Vicsek fractal with  $I = 6$  and  $W = 1458$ . The slope of the dashed line has been set equal to the Hausdorff dimension of the samples. Results for two different lead locations are shown with different symbols. (c) Finite-size scaling of the fractal dimension for the Sierpinski gasket and the Vicsek fractal. The symbols show the BC dimension  $d$  of the gasket (orange) and Vicsek fractal (blue) as the number  $I$  of iterations in the generation of the fractal is increased. The dashed lines mark the values of the Hausdorff dimension  $d_H = 1.58$  and  $d_H = 1.46$  of the gasket and Vicsek fractal, respectively.

multiple extended regions where the conductance is zero, whereas for the carpets the conductance fluctuates heavily over the entire energy range, except around  $E = 0$  for the hexagonal-lattice case.

Fig. 5.13 shows the energy dependence of the conductance  $G(E)$  for the Sierpinski gasket and the Vicsek fractal. For these structures the profile of the conductance is characterized by many intervals where the conductance vanishes. This behavior is different from the conductance of the SC, which is non-zero in a broad energy interval. The intervals of vanishing conductance

appear to have a self-similar geometry, as suggested by the inset of (a), where it is seen that the conductance in the interval  $0.9 < E/t < 1.2$  features four cluster of peaks, just like in the whole interval  $-3 < E/t < 2$ . This is further demonstrated by applying the BC algorithm, which yields a non-integer dimension  $d$ .

Fig. 5.14(c) shows the BC dimension  $d$  for the conductance fluctuations of the gasket (orange) and Vicsek fractal (blue) as the number  $I$  of iterations in the generation of the fractal is increased. The crosses show the result of the BC analyses, the dotted lines are a guide to the eye, and the arrows mark the values of the Hausdorff dimension  $d_H = 1.58$  and  $d_H = 1.46$  of the gasket and Vicsek fractal, respectively. The figure shows that the estimate of  $d$  for the gasket is largely independent of  $I$ , and that convergence is achieved for the Vicsek fractal when  $I \gtrsim 10$ . In both cases, the estimated BC dimension  $d$  is substantially different than the Hausdorff dimension  $d_H$ . More precisely  $|d - d_H| \gtrsim 10\%$  for the gasket and Vicsek fractal, while  $|d - d_H| \lesssim 2\%$  for the SCs.

A qualitative difference between the SC and the gasket/Vicsek fractal is the value of their ramification number [123], i.e. the number of bonds that must be cut in order to isolate different iterations of the lattice. This number gives a measure of how connected the fractal is. For the gasket and Vicsek fractal, the ramification is *finite*, while for the SC it is infinite. For fractals with finite ramification it is possible to give analytical solutions to the Schrödinger equation [117], while general fractals with infinite ramification are not amenable to analytical treatments. These two types of fractals can have widely different properties. For example, it has been found that infinitely ramified fractals exhibit phase transitions not present in finitely ramified fractals [123]. The relation between the dimensions of the samples in the SC family and of the corresponding CFs is possibly a consequence of the infinite ramification of the SC. Intuitively, electrons in a SC explore a larger portion of the available phase space, and thus their conduction properties are more closely related to those of the sample.

## 5.5 Summary

We have studied the conductance of self-similar samples. Using a box-counting algorithm on the conductance graph, we found that its fractal dimension is approximately equal to the geometric Hausdorff dimension of the sample. This result holds for SCs with different lead positions, different underlying lattices, different  $d_H$  and with a vacancy or smooth disorder. However, for the SG and Vicsek fractals we found that these dimensions do not match. A probable explanation is that the SC is infinitely ramified, meaning that the lattice is very well connected and the electrons can probe the entire sample, whereas the other two fractals are finitely ramified making it harder for the electrons to travel far. Although more work is necessary to establish this connection at a formal level, we believe that our results motivate careful transport studies of planar fractal devices.

## CHAPTER 6

# OPTICAL AND PLASMONIC PROPERTIES OF SIERPINSKI FRACTALS

The optoelectronic and plasmonic properties of fractal quantum electron systems are largely unexplored. In this chapter, we calculate the optical conductivity of a two-dimensional electron gas in a Sierpinski carpet (SC). We show that the optical conductivity converges as a function of the fractal iteration. The calculated optical spectrum features sharp peaks at frequencies determined by the smallest geometric details at a given fractal iteration. Each peak is due to excitations within sets of electronic state-pairs, whose wave functions are characterized by quantum confinement in the SC at specific length scales, related to the frequency of the peak. Moreover, we calculate the full dielectric functions of the Sierpinski carpet and gasket. We show that the Sierpinski gasket features highly localized plasmon modes with a flat dispersion. This strong plasmon confinement can provide a novel setting for manipulating light at the quantum level.

*This chapter is published as: E. van Veen, A. Tomadin, M. Polini, M.I. Katsnelson, S. Yuan “Optical conductivity of a quantum electron gas in a Sierpinski carpet,” *Physical Review B* 96, 235438 (2017), and as T. Westerhout, E. van Veen, M.I. Katsnelson, S. Yuan “Plasmon confinement in fractal quantum systems,” *Physical Review B* 97, 205434 (2018).*



## 6.1 Introduction

As discussed in the previous chapter, recent advances in nanofabrication methods have made it possible to create multi-scale two-dimensional (2D) structures, which are geometrically defined down to the nanometer scale, and yet feature excellent electronic quantum conduction properties on micrometer length scales.

However, to the best of our knowledge, no theoretical study has ever addressed the optical and plasmonic properties of quantum electron systems in a fractal structure. From an optoelectronic perspective, the theory is challenging because these systems are extended and cannot be easily treated as single emitters coupled to radiation, yet they are not periodic, so that a classification of electronic states based on the Bloch theorem is not possible either.

Historically, in most plasmonic devices, the Fermi wavelength of the electrons was much smaller than the plasmon wavelength which is of the order of the geometric size of the system for standing waves. In other words, the characteristic plasmon wave vector  $q \ll k_F$ , where  $k_F$  is the Fermi wave vector. In this regime, plasmons can be described classically and there is no need to use a quantum mechanical approach [124, 125, 3, 2].

Recently, due to the progress in nanodevice fabrication, the quantum regime for plasmons has been reached [126, 127]. In this regime, localized surface plasmons make it possible to confine light to scales much smaller than the scales of conventional optics, and as such provide a unique way for light manipulation on scales below the diffraction limit. Surface plasmons have found applications in surface-enhanced spectroscopy [128, 129], biological and chemical sensing [130], lithographic fabrication [131], and photonics [132].

However, the theory of inhomogeneous quantum electron plasma, even in the simplest random-phase approximation (RPA) [124, 125, 3, 2], is quite complicated due to the essential nonlocality of the dielectric function [3]. Recently, a rigorous scattering theory of plasmons by obstacles was built [133], but finding plasmon eigenmodes of inhomogeneous quantum systems still remains a challenge. As a matter of fact, this problem is very old,

starting with the early considerations [134, 135] of “atomic plasmons” [136, 137, 138, 139, 140] which eventually turned out to not exist [141, 142]. Previous attempts use additional uncontrollable approximations such as truncation of quantum states [140], semi-classical [136, 139, 142] or even classical [138] approaches.

In the first section, we discuss the specific models and methods used for our calculations.

In the second section we show that the optical conductivity as a function of frequency (i.e. the optical spectrum) converges to a definite profile as the fractal iteration increases, and we investigate the converged optical spectrum for different model parameters, highlighting the unexpected appearance of sharp peaks. We also explain the origin of these peaks by analyzing the contribution to the optical conductivity of sets of specific electronic state-pairs in SCs of reduced size, which are amenable to exact diagonalization.

In the third section we discuss the results of calculations of plasmonic properties of fractal systems. We compare the plasmon dispersions of the Sierpinski carpet and gasket to those of a square and triangle, respectively.

## 6.2 Model and methods

### 6.2.1 Hamiltonian

We consider the bottom-up models for the SC and SG from the previous chapter (Fig. 5.2).

For the calculations on plasmonics, we need to define the hopping parameter and lattice constant. We use  $t = 2.8 \text{ eV}$  and  $a = 0.246 \text{ nm}$ . These are the parameters for graphene, and they are representative for 2D systems in general. Choosing a different lattice constant will lead to a different plasmon spectrum, but the same qualitative behavior.

### 6.2.2 Optical conductivity

To compute the optical spectrum (Eqs. 2.18 - 2.21) of the Hamiltonian (Eq. 5.1) on a SC, we can use exact diagonalization, provided the sample is small enough.

For larger systems, we use the tight-binding propagation method (Eq. 2.41). The TBPM is very efficient for large quantum systems without translational invariance, such as fractals, because it performs calculations in real space and does not require exact diagonalization. The density of states  $D(E)$  can be calculated with TBPM as well, using Eq. 2.35.

### 6.2.3 Dielectric function

For the calculation of the dielectric function we use Eq. 2.23. We set the temperature  $T = 300$  K, an inverse relaxation time  $\delta = 6$  meV/ $\hbar$ , chemical potential  $\mu = 0.4$  eV and a self-interaction potential of 15.78 eV.

To visualise the plasmon modes in a quantum mechanical system Wang et al [143] introduced the following method. Consider the dielectric function in its spectral decomposition:

$$\varepsilon(\omega) = \sum_n \epsilon_n(\omega) |\phi_n(\omega)\rangle \langle \phi_n(\omega)| . \quad (6.1)$$

In this method, for each  $\omega$  we consider only the eigenvalue  $\epsilon_{n_1(\omega)}(\omega)$  that has the highest value of  $-\text{Im}[1/\epsilon_n(\omega)]$ , which gives us the plasmon eigenmode  $|\phi_{n_1(\omega)}(\omega)\rangle$  that contributes most to the loss function.

However, it is not clear how to access these plasmon modes experimentally. Currently, the standard way of probing plasmon properties of small quantum mechanical systems is electron energy loss spectroscopy (EELS). The fact that we calculate the *full* dielectric function gives us the possibility to calculate the following Fourier transform, which distinguishes this study from others:

$$\langle \mathbf{q} | \varepsilon(\omega) | \mathbf{q} \rangle = \frac{1}{(2\pi)^2} \int d\mathbf{r} \int d\mathbf{r}' \langle \mathbf{r} | \varepsilon(\omega) | \mathbf{r}' \rangle e^{-i\mathbf{q}(\mathbf{r}-\mathbf{r}')} . \quad (6.2)$$

The loss function  $-\text{Im}[1/\langle \mathbf{q} | \varepsilon(\omega) | \mathbf{q} \rangle]$  is then directly measurable using EELS techniques [124, 125, 3, 2, 144].

Formally, there are two ways of identifying plasmons. A plasmon frequency is either given by a local maximum of the loss function  $-\text{Im}[1/\varepsilon_{n_1(\omega)}(\omega)]$ , or by a frequency at which  $\text{Re}[\varepsilon_{n_1(\omega)}(\omega)] = 0$ . These frequencies are not exactly equal due to Landau damping, which is quantified by  $\delta$  [145].

## 6.3 Optical conductivity of Sierpinski carpets

### 6.3.1 Convergence and parameter dependence of the spectrum

In Fig. 6.1 we show the optical spectrum at different fractal iterations  $I$ . It is remarkable that, as the total width  $W$  of the SC increases, the optical spectrum maintains its overall profile. Indeed, by comparing the results at  $I = 7$  and  $I = 8$ , we conclude that, for any practical purpose, the optical spectrum has converged by iteration  $I = 7$ .

Focusing on  $I = 7$ , we present in Fig. 6.2 the optical spectrum and the DOS for different sizes  $S$  of the initial  $I = 0$  square. Both quantities are markedly different for  $S = 1$  and  $S = 2$ . Interestingly, this shows that the finest geometric structures of the SC play a substantial role in its optical response, even in the limit of very large carpets, when such structures are negligible in size. For both investigated values of  $S$ , the optical spectrum is characterized by sharp peaks at low frequencies  $\hbar\omega \lesssim t$ .

In Fig. 6.3 we show the optical spectrum at different fractal iterations  $I$ , keeping fixed the sample size  $W$  and decreasing the size  $S$  of the  $I = 0$  square consequently. This top-down or algorithm represents more faithfully a physical fabrication process based on etching more and more details into a solid-state sample. From Fig. 6.3 it is apparent that increasing the detail in the sample leads to higher-frequency peaks in the optical spectrum.

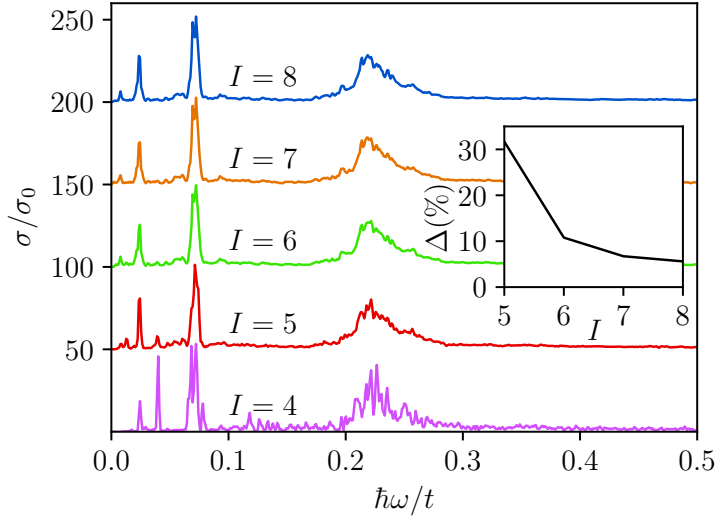


Figure 6.1: Optical spectrum at  $S = 1$  and increasing fractal iteration  $I$ . (Graphs are progressively offset by  $50\sigma_0$  for clarity.) The three highest peaks for  $I = 5$  are already very close to the converged result for  $I = 7$ . The inset shows the relative difference between the conductivities at subsequent iterations,  $\Delta(I) = \int |\sigma^{(I)}(\omega) - \sigma^{(I-1)}(\omega)| d\omega / \int \sigma^{(I)}(\omega) d\omega$ . This quantity decreases with  $I$  to  $\Delta(I) \lesssim 5\%$  for  $I \geq 8$ . We expect a residual nonzero difference partly due to the fact that the limit of a perfect fractal has not been reached yet, and partly because we are using a finite number of random states for the TBPM calculations, resulting in some statistical fluctuations.

### 6.3.2 Origin of the peaks in the optical spectrum

While the TBPM method allows us to calculate the optical spectrum and the DOS of SCs up to fractal iteration  $I = 8$ , smaller systems up to  $I = 5$  are amenable to exact diagonalization. Although the optical spectrum is not converged for  $I = 5$ , it already features well-defined low-frequency sharp peaks (at  $\hbar\omega \simeq 0.023t$ ,  $0.071t$ , and  $0.22t$ ) that do not shift appreciably as  $I$

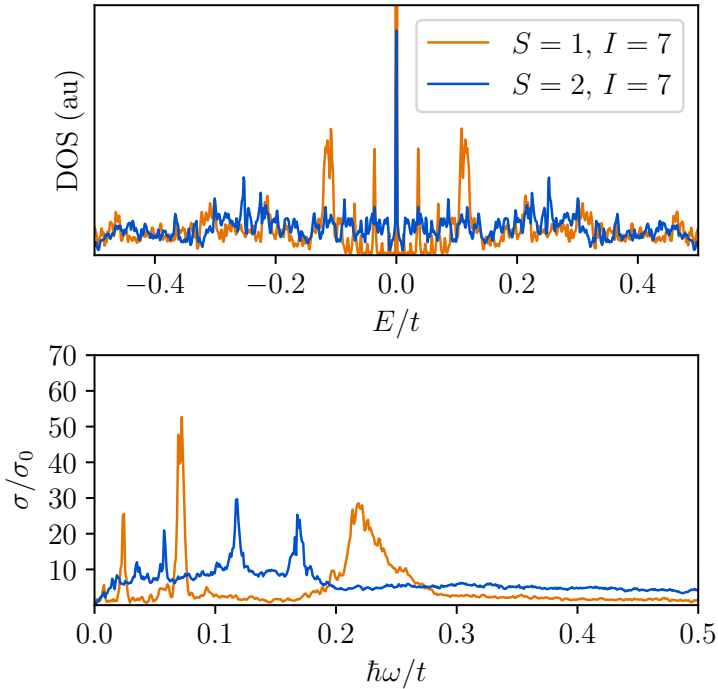


Figure 6.2: Converged DOS (top) and optical spectrum (bottom) for SCs with  $S = 1$  (orange),  $S = 2$  (blue), and  $I = 7$ .

is increased further. For this reason, we reckon that exact diagonalization of the SC at fractal iteration  $I = 5$  can give us reliable information on the origin of the spectral peaks.

We first show that the spectral peaks cannot be understood as van-Hove-like singularities, i.e. an enhancement of the optical response at those frequencies matching a very large set of electronic transitions. To do so, we compare the optical spectrum and the conductivity-like JDOS extracted from Eq. (2.17) in Fig. 6.4 in the specific case  $S = 1$  and  $I = 5$ . We clearly see that there is no substantial correlation between these two functions.

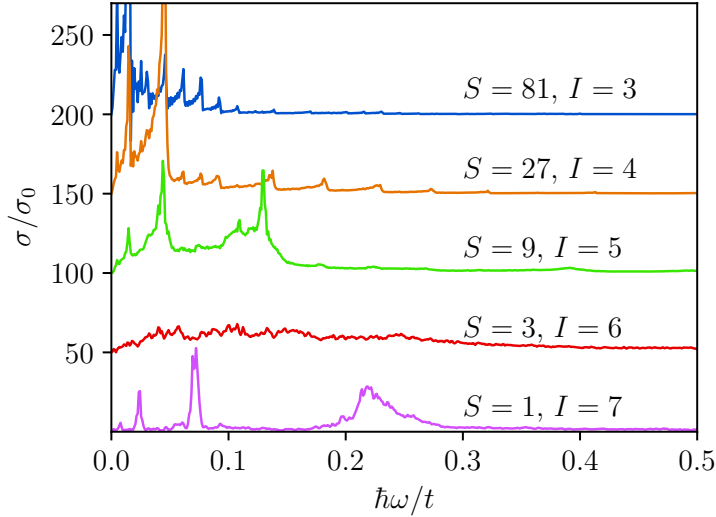


Figure 6.3: Optical spectrum for fixed SC width  $W = 2187$  and different fractal iteration  $I$ . (Graphs are progressively offset by  $70\sigma_0$  for clarity.) To keep the width  $W$  fixed, the size  $S$  of the  $I = 0$  square decreases as  $I$  increases. Finer geometric structure generated at higher  $I$  generally introduces higher frequency peaks.

The contributions of excitations between the two peaks in the DOS at  $E = -0.11t$  and  $E = 0.11t$  (see Fig. 6.2) could be expected to account for the optical conductivity peak at  $\hbar\omega = 0.22t$ , but these contributions are washed out by those of state-pairs in which one state is around  $E = 0$ .

To show that the spectral peaks are also not due to few, particularly effective, electronic transitions between single state-pairs, we use the current-current response function (Eq. 2.18). For each matrix element,  $(j_\alpha)_{mn}$ , we calculate the quantity  $|(P_m - P_n)(J_x)_{mn}^2|$ , which is a measure of the strength of an electronic transition, independent of the frequency of the field which drives the transition itself. Fig. 6.5 shows the distribution of the magnitude of this quantity. If the peaks in the optical spectrum were due to a

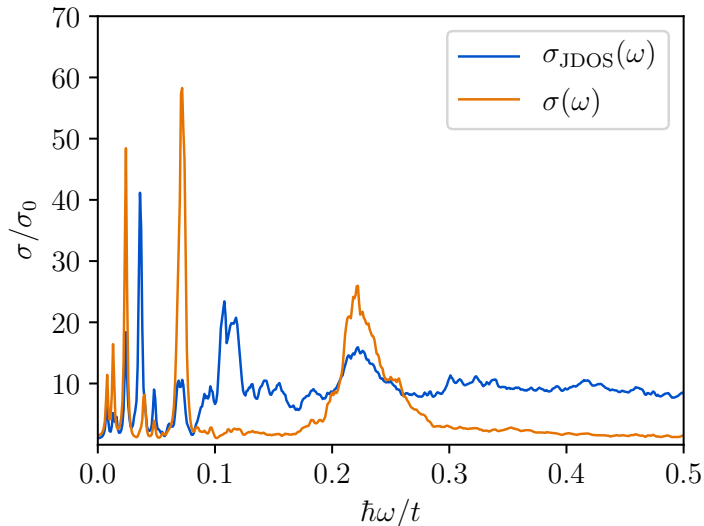


Figure 6.4: Comparison of the optical spectrum (orange) and the conductivity-like JDOS defined in Eq. 2.17 (blue) for  $S = 1$  and  $I = 5$ .

few electronic transitions, the distribution should have a few large values with a small number of occurrences – which is clearly not the case.

Summarizing the analysis above, we have ruled out that sharp peaks in the optical spectrum arise from dense, energy-localized sets of transitions, or from sparse, isolated transitions between state-pairs. We are then left with the option that the origin of the spectral peaks are transitions between large and non-trivial sets of state-pairs, uncorrelated with the JDOS. In the following, we characterize these sets, by directly looking at the probability density of the wave functions on the SC. For example, the large peak in  $\text{Re}\sigma(\omega)$  at  $\hbar\omega = 0.071t$  in Fig. 6.4 for a SC with  $S = 1$  and  $I = 5$  is due to a collection of hundreds of state-pairs, two of which are shown in Fig. 6.6. These state-pairs have all nearly the same contribution to that peak in the optical spectrum and display very similar heart-shaped spatial features on the scale of the geometric details introduced by the third ( $I = 3$ ) fractal



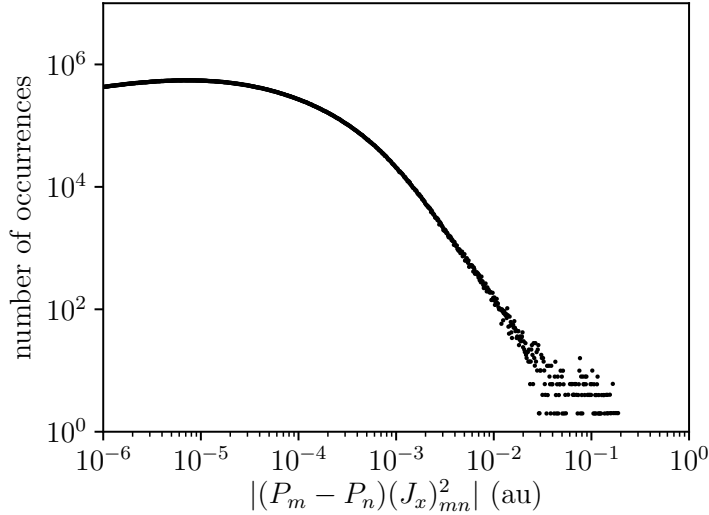


Figure 6.5: Number of occurrences of the quantity  $|(P_m - P_n)(J_x)_{mn}^2|$ , using logarithmically distributed bins, calculated from the electronic spectrum in a SC with  $S = 1$  and  $I = 5$ .

iteration. Similarly, in Fig. 6.7 we display the state-pairs contributing most to the peak at  $\hbar\omega = 0.22t$  in a SC with  $S = 1$  and  $I = 5$ , which display similar heart-shaped profiles, but with length scales that are  $\mathcal{L} = 3$  times shorter, on the order of the second ( $I = 2$ ) fractal iteration. All these wave functions show very similar profiles, corresponding to confinement at a specific fractal iteration, with higher peak frequencies being related to shorter length scales within the SC. This behavior agrees with the results shown in Fig. 6.3, i.e. “etching” an extra iteration into the sample generally introduces higher frequency optical peaks.

To make a more quantitative connection between the peak frequencies in the optical spectrum and the characteristic “confinement lengths” appearing in the electronic wave functions, we calculate the sum of probability densities, weighted by their contribution to the optical conductivity, as a

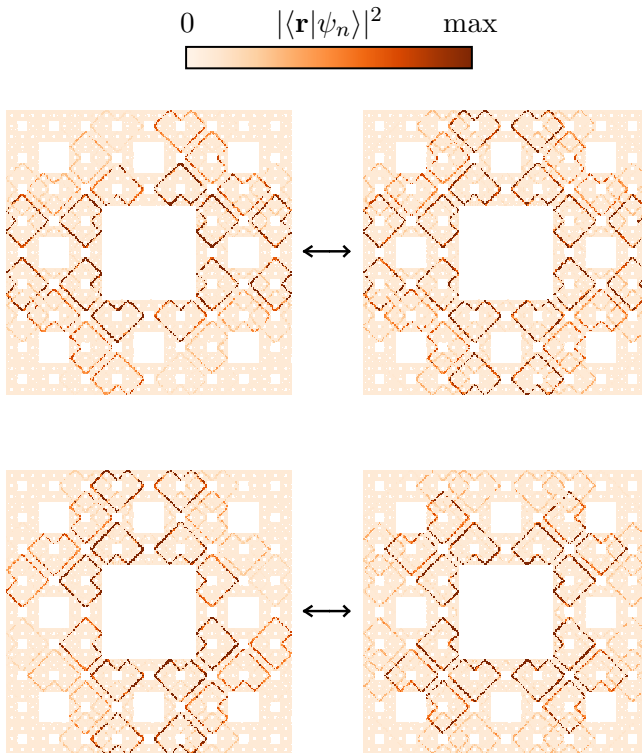


Figure 6.6: Two sets of top-contributing state-pairs for the peak at  $\hbar\omega = 0.071t$ , in a SC with  $S = 1$  and  $I = 5$ .

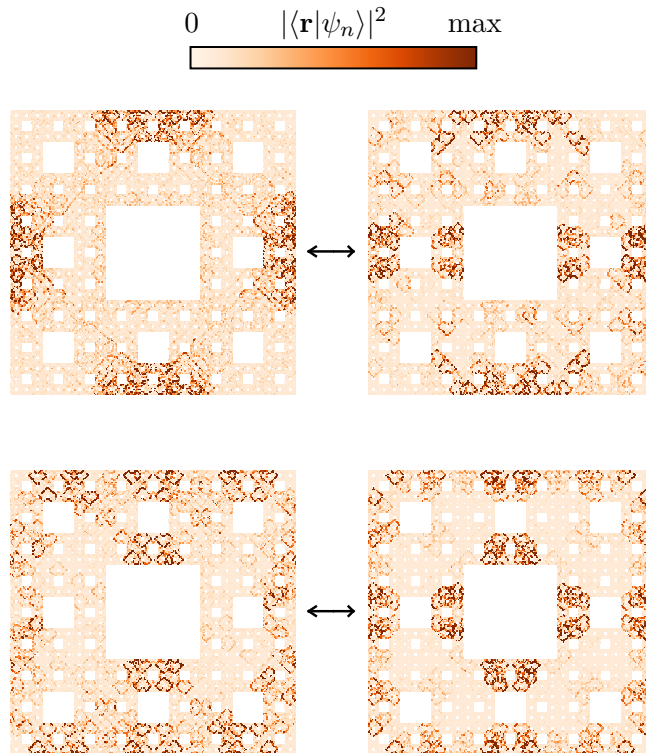


Figure 6.7: Two sets of top-contributing state-pairs for the peak at  $\hbar\omega = 0.220t$ , in a SC with  $S = 1$  and  $I = 5$ .

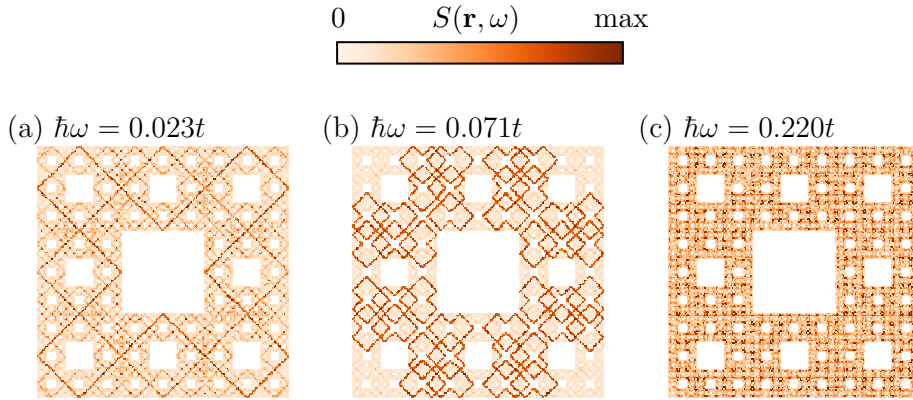


Figure 6.8: Cumulative probability distributions  $S(\mathbf{r}, \omega)$  of state-pairs contributing to the peaks at (a)  $\hbar\omega = 0.023t$ ; (b)  $\hbar\omega = 0.071t$ ; and (c)  $\hbar\omega = 0.22t$ , in a SC with  $S = 1$  and  $I = 5$ .

function of  $\omega$ :

$$S(\mathbf{r}, \omega) = - \sum_{mn} \frac{1}{\omega} \text{Im} [Q_{mn}(\omega)] |\langle \mathbf{r} | \psi_n \rangle|^2. \quad (6.3)$$

The sum is restricted to states  $m$  and  $n$  such that their energy difference falls within the window  $\hbar(\omega - \delta\omega) < |E_m - E_n| < \hbar(\omega + \delta\omega)$ , with  $\hbar\delta\omega = 0.01t$ . Due to particle-hole symmetry, the result is the same for taking the probability distributions  $|\langle \mathbf{r} | \psi_n \rangle|^2$  over the index  $m$ .

Fig. 6.8 shows the spatial profile of the quantity  $S(\mathbf{r}, \omega)$  in a SC, for three values of  $\omega$  corresponding to peaks in the optical spectrum. The plots demonstrate a clear distinction in the characteristic length scale of the probability density for different frequencies.

The substantial numerical effort needed to exactly diagonalize the Hamiltonian (5.1) on a SC hinders a more precise characterization of the state-pairs sets. We note that the heart-shaped features of the probability density are distorted at  $\hbar\omega = 0.023t$ , where the confinement length scale

is on the order of the geometric details introduced by the fourth ( $I = 4$ ) fractal iteration. This is an artefact of the final size of the SC that we can diagonalize exactly, and we reckon that at the sixth ( $I = 6$ ) fractal iteration the heart-shaped features would fit the SC geometry. Moreover, for  $S = 2$  a similarly thorough analysis is too expensive numerically to cover in this work. At  $I = 4$ , there is already some connection between length scale and optical peak frequency, and there appears to be some extra splitting, causing two peaks per length scale. However, the optical conductivity is not yet close enough to its converged result to make any conclusive statements.

## 6.4 Plasmon confinement in fractal quantum systems

The real-space loss function of the highest contributing plasmon mode is shown in Fig. 6.9. It shows that there is a large number of plasmon frequencies, and that the associated losses increase with increasing frequency. At each discontinuity in  $\text{Re}[\epsilon_{n_1(\omega)}(\omega)]$  a different mode is found to be the highest contributor to the loss function. Such a discontinuity is not associated with a plasmon, even though  $\text{Re}[\epsilon_{n_1(\omega)}(\omega)]$  switches sign.

The real part of the highest contributing plasmon eigenmodes for both the carpet and gasket are shown in Fig. 6.10. For further analysis, the inverse participation ratio  $\text{IPR}(\omega) = \int d^d r |\langle \mathbf{r} | \phi_{n_1(\omega)} \rangle|^4$  can give us a measure of localization. The average IPR of  $|\phi_{n_1(\omega)}\rangle$  was found to be an order of magnitude higher for the gasket than for the carpet. This can be seen as a consequence of the finite ramification of the gasket, i.e. the fact that it is less connected, and therefore the electrons are more confined and exhibit more localized plasmon eigenmodes. Fig. 6.10(d) shows an example of such a highly localized mode.

We now turn to the Fourier transform of the real-space loss function in order to make a comparison to EELS experiments. Fig. 6.11 shows the loss function as function of both  $q$  and  $\omega$ .

There is a close resemblance between the carpet (Fig. 6.11(a)) and a square sample (Fig. 6.11(b)). The dispersion of the carpet has extra

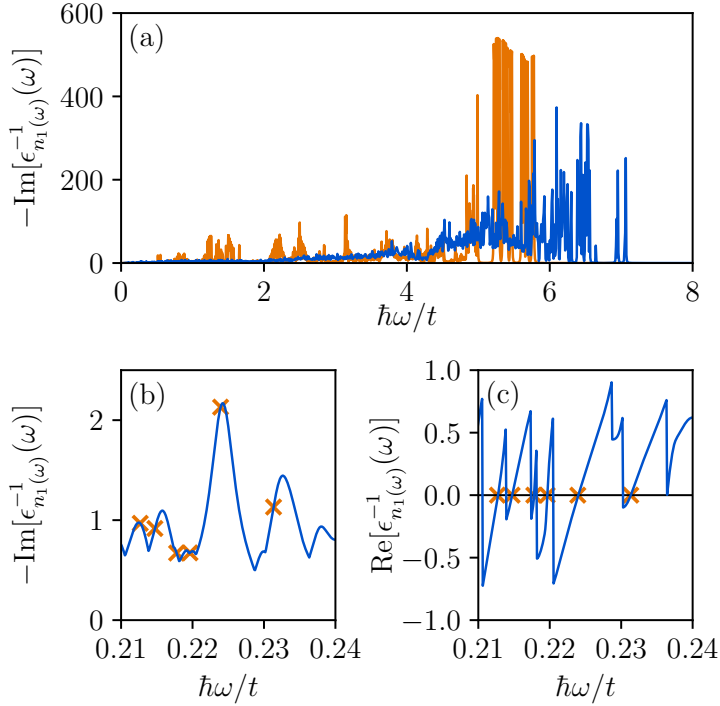


Figure 6.9: The highest contribution to the loss function  $-\text{Im}[\epsilon_{n_1(\omega)}^{-1}(\omega)]$ . (a) The loss function for the entire range of frequencies, in the case of (blue) a third iteration Sierpinski carpet and (orange) a sixth iteration Sierpinski gasket. (b) The loss function of a third iteration Sierpinski carpet for a frequency interval  $0.21t < \hbar\omega < 0.24t$ . (c)  $\text{Re}[\epsilon_{n_1(\omega)}^{-1}(\omega)]$  for a frequency interval  $0.21t < \hbar\omega < 0.24t$ , showing discontinuities. Orange crosses indicate pairs of points between which  $\text{Re}[\epsilon_{n_1(\omega)}^{-1}(\omega)]$  crosses zero in a continuous manner.

broadening, similar to the broadening found in systems with disorder [146]. However, generally speaking, both curves look like a regular  $\varepsilon(\omega) \propto \sqrt{q}$  dispersion relation for surface plasmons [2]. The carpet exhibits no trans-

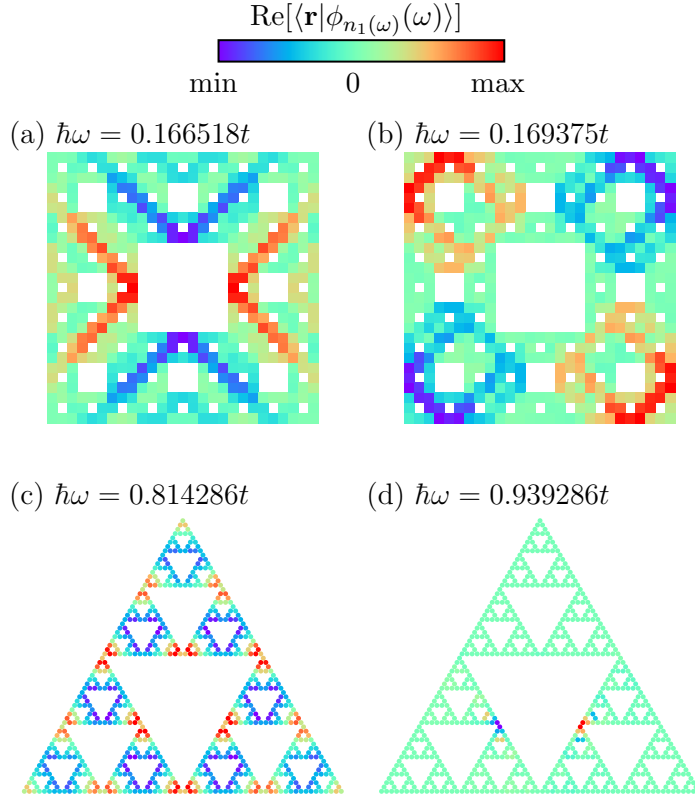


Figure 6.10: The highest contributing plasmon eigenmodes in real space. A few examples of the real space distribution  $\text{Re}[\langle \mathbf{r} | \phi_{n_1(\omega)}(\omega) \rangle]$  of plasmon modes, where red represents a positive value and blue represents a negative value, for (a),(b) a third iteration Sierpinski carpet and (c),(d) a sixth iteration Sierpinski gasket. Eigenmodes exhibiting different characteristic length scales are shown.

lational invariance, i.e.  $q$  is not actually a good quantum number, so this behavior is quite remarkable. The dispersion of the fourth iteration Sierpinski carpet is already very close to the third iteration dispersion. This convergence indicates that the result is representative for the real fractal at infinite iteration.

For the Sierpinski gasket (Fig. 6.11(c)), we observe different behavior. This fractal does not closely follow the dispersion relation of a triangle built out of a triangular lattice (Fig. 6.11(d)). Instead, we can clearly see the formation of modes with a nearly flat dispersion, which means that they are localized, as the Fourier transform of the dielectric function is only weakly dependent on  $q$ . Again, this result is reasonably converged.



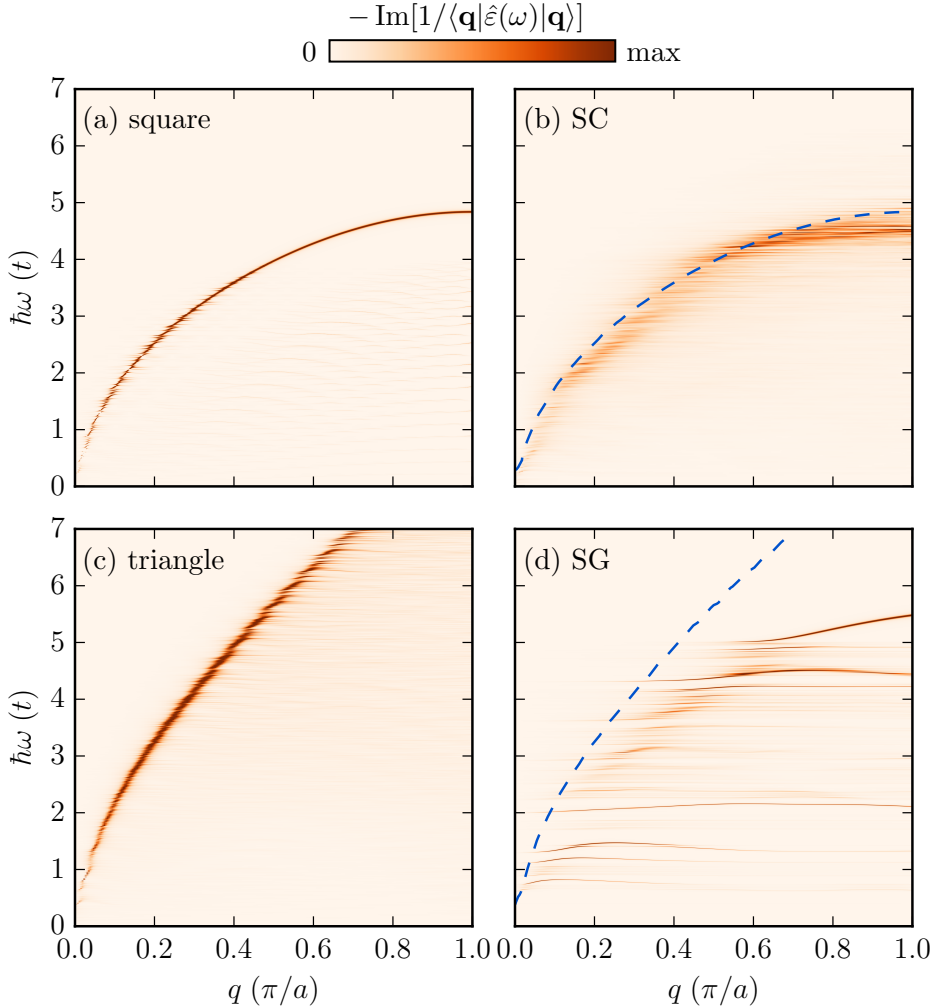


Figure 6.11: Dispersion relation  $-\text{Im}[1/\langle \mathbf{q} | \hat{\epsilon}(\omega) | \mathbf{q} \rangle]$ , showing the frequency and momentum dependency of the loss function. (a) A square built out of square lattice as compared to (b) the fourth iteration Sierpinski carpet. Similarly, (c) a triangle built out of triangular lattice as compared to (d) a sixth iteration Sierpinski gasket. The maximum of the left hand side is plotted as a dashed blue line on the right hand side.

## 6.5 Summary

In this chapter we have calculated the optical spectrum of a quantum electron gas roaming in a Sierpinski carpet. We have shown that the optical spectrum converges to a definite profile as the fractal iteration increases. The optical spectrum displays sharp peaks, which blue-shift as finer geometric structures are produced at higher fractal iterations. We have pinned down the origin of these peaks to electronic transitions between set of specific state-pairs whose wave functions experience quantum confinement in the Sierpinski carpet at specific length scales.

Moreover, we have calculated the plasmon dispersion for the Sierpinski carpet and Sierpinski gasket. The Sierpinski carpet has a plasmon dispersion comparable to the dispersion of a square lattice, whereas the gasket exhibits highly localized plasmon modes. More generally, a finitely ramified fractal can exhibit strong plasmon confinement, providing a novel setting for the manipulation of light at the quantum scale. With current experimental techniques, these results can be probed experimentally. Moreover, we have presented a rigorous approach for calculating plasmonic properties of generic tight-binding systems, published as an open source software project [4]. We believe that this code can be very useful for future projects relating to plasmonic properties of non-translationally invariant systems.



# APPENDIX: TIPSİ – A TIGHT-BINDING PROPAGATION PACKAGE FOR PYTHON

The tight-binding propagation method provides a numerically cheap way to calculate electronic, transport and optical properties of large tight-binding systems. In this chapter, we present Tipsi (Tight-binding propagation simulator): an open-source Python package for applying this method to any tight-binding Hamiltonian.

Tipsi is available on <https://gitlab.science.ru.nl/tcm/tipsi>.

## 7.1 Installation

You will need Python 3 with numpy and scipy. Optional modules for input and output are h5py and matplotlib. Moreover, you will need a FORTRAN compiler.

To get the Tipsi files, type in a terminal:

```
git clone https://gitlab.science.ru.nl/tcm/tipsi
```

Then, install it using:

```
python setup.py install
```

in the main Tipsi directory. For information about how to manually install the package, or set the compiler configuration, we refer to the documentation.

Now, we can get started. Create a new .py file and type:

```
import tipsi
```

## 7.2 Sample building

### 7.2.1 Lattices

A Lattice object contains the geometrical information of a material. It is initiated with a list of lattice vectors and a list of orbital coordinates. E.g., for graphene:

```
a = 0.24 # lattice constant in nm
b = a / sqrt(3.) # carbon-carbon distance in nm
vectors      = [[1.5 * b, -0.5 * a, 0.],
                [1.5 * b, 0.5 * a, 0.]]
orbital_coords = [[-b / 2., 0., 0.],
                  [b / 2., 0., 0.]]
lat = tipsi.Lattice(vectors, orbital_coords)
```

If you are working with multiple orbitals per site, each orbital must be listed separately in the second argument. In Tipsi, you should always use nanometers as distance unit.

## 7.2.2 SiteSets

A SiteSet object contains sites, that are added by unit cell coordinate and orbital index. E.g., for graphene:

```
W = 10 # width
H = 10 # height
site_set = tipsi.SiteSet()
for i in range(W):
    for j in range(H):
        unit_cell_coors = (i, j, 0)
        site_set.add_site(unit_cell_coors, 0)
        site_set.add_site(unit_cell_coors, 1)
```

At each unit cell coordinate, we add two sites, generating 10 by 10 unit cells in total.

## 7.2.3 HopDicts

A HopDict object contains the electronic information of a material. It is given by a list of hopping matrices corresponding to relative unit cell coordinates. E.g., for graphene:

```
t = 2.7 # hopping constant in eV
e = 0.0 # on-site potential in eV
A_0 = [[e, t],
        [t, e]]
A_nn0 = [[0., 0.],
          [t, 0.]]
A_nn1 = [[0., t],
          [0., 0.]]

hop_dict = tipsi.HopDict()
hop_dict.set((0, 0, 0), A_0)
hop_dict.set((1, 0, 0), A_nn0)
hop_dict.set((-1, 0, 0), A_nn1)
hop_dict.set((0, 1, 0), A_nn0)
hop_dict.set((0, -1, 0), A_nn1)
```

In Tipsi, you should always use the energy unit electronvolts.

### 7.2.4 Periodic boundary conditions

We need to tell Tipsi how to treat the boundary of the sample. Hence, we define a function that takes a site coordinate outside the sample, and returns a coordinate that falls within the sample. E.g., for graphene:

```
def pbc_func(unit_cell_coords, orbital):
    x, y, z = unit_cell_coords
    return (x % W, y % H, z), orbital
```

This gives periodic boundary conditions along  $x$  and  $y$  directions. Of course, we could also define periodic boundary conditions in only one direction, to create a ribbon sample:

```
def pbc_func_ribbon(unit_cell_coords, orbital):
    x, y, z = unit_cell_coords
    return (x % W, y, z), orbital
```

### 7.2.5 Samples

We now have all the ingredients to create a sample. A Sample object generates the full tight-binding Hamiltonian, given a Lattice, SiteSet, HopDict, and boundary conditions. Also, keep in mind the Hamiltonian will have to be rescaled, to fulfill the requirement that all eigenvalues must be in the range  $[-1, 1]$ .

```
sample = tipsi.Sample(lat, site_set, pbc_func)
sample.add_hop_dict(hop_dict) # apply HopDict
sample.rescale_H(9.) # rescale Hamiltonian
sample.plot() # plot sample
```

The resulting plot looks like Fig. 7.12. As you can see, there are hoppings between the outer sites of the sample, indicating that there are periodic boundary conditions in both directions.

### 7.2.6 Adding disorder

We can introduce many types of disorder to our tight-binding model.

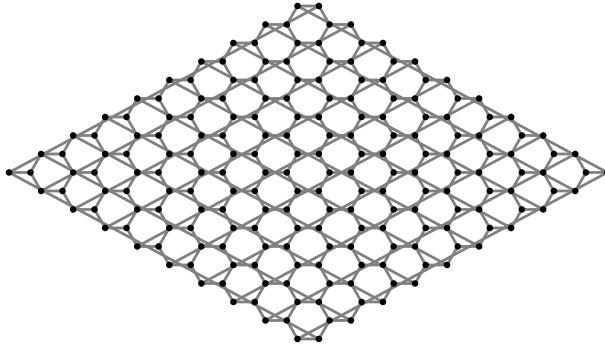


Figure 7.12: A 10 by 10 graphene sample with nearest neighbor hopping and periodic boundary conditions.

Vacancies can be made by deleting a site from the SiteSet, before initializing the Sample object:

```
site_set.delete_site(unit_cell_coords, orbital)
```

After adding a HopDict, we can add or change individual hoppings with:

```
sample.set_hopping(hop, unit_cell_coord0, \
    unit_cell_coord1, orbital0, orbital1)
```

Moreover, Tipsi has some convenience functions for common types of external fields.

We can uniformly strain the Lattice, HopDict pair with (for black phosphorus [74])

```
strain = 5      # strain in percent
beta = 4.5     # strain coefficient
strain_tensor = 0.01 * strain * np.diag([-0.2, 1, -0.2])
lattice, hop_dict = tipsi.uniform_strain(lattice, \
    hop_dict, strain_tensor, beta)
```

If we have a HopDict with interlayer hoppings, we can create a multi-layer sample and add bias by using



```

n_layers = 2    # number of layers
bias = 1.0     # bias in eV/nm
n_orbitals = 2 # number of orbitals

# extend unit cell in z-direction
lattice, hop_dict = \
    tipsi.extend_unit_cell(lattice, hop_dict, 2, n_layers)

# add bias
for i in range(n_orbitals * n_layers):
    z = lat.site_pos((0, 0, 0), i)[2]
    onsite_pot = z * bias
    hops.set_element((0, 0, 0), (i, i), onsite_pot)

# remove redundant z-direction hoppings
hops.remove_z_hoppings()

```

Finally, a magnetic field can be introduced using a Peierls substitution, using units of Tesla, with:

```
sample.set_magnetic_field(B)
```

## 7.2.7 Material library

Tipsi contains a material library with functions returning Lattice, HopDict, SiteSet, PBC and Sample objects for a small selection of materials. These can be accessed using import statements:

```

# import graphene material library
from tipsi.materials import graphene

# make 1000*1000 unit cell sample
sample = graphene.sample(1000, 1000)

```

In the current version (0.9), the following materials are available:

- single layer graphene with nearest neighbor hoppings
- single layer antimonene [27]

- multilayer black phosphorus [72]
- single layer MoS<sub>2</sub> and WS<sub>2</sub> [147]

### 7.2.8 Interface with Wannier90

It is easy to create a Lattice, HopDict pair using Wannier90 output files. To this end, we use the function

```
lattice, hop_dict = \
    read_wannier90(lat_file, coord_file, ham_file[, corr_file])
```

Here, *lat\_file* contains lattice vectors and atom numbers, usually named “\*.win”. *coord\_file* contains orbital coordinates, usually named “\*\_centres.xyz”. *ham\_file* contains all the hoppings, usually named “\*\_hr.dat”. *corr\_file* contains correction terms for hoppings, usually named “\*\_wsvec.dat”.

### 7.2.9 *k*-space functions

To check the Lattice and HopDict objects, we can calculate the band structure that they produce, provided a list of points in *k*-space:

```
bands = tipsi.band_structure(hop_dict, lat, kpoints)
for band in bands.swapaxes(0, 1):
    plt.plot(kvals, band)
```

We can also calculate band structures for entire Sample objects, although this is of course not feasible for larger systems:

```
bands = sample.band_structure(kpoints)
```

## 7.3 Configuration

Before we can run a simulation we need to set the parameters for the TBPM calculations. For example, if we want to use 1024 time steps, 4 random samples, an energy range from -10 to 10 eV and we want to correct for spin in the final result:

```
config = tipsi.Config(sample)
config.generic['nr_time_steps'] = 1024
config.generic['nr_random_samples'] = 4
config.generic['energy_range'] = 20.
config.generic['correct_spin'] = True
config.save()
```

The last line ensures that the configuration object is saved to file, with the same timestamp prefix as the correlation files.

Each correlation function calculation has its own set of configuration parameters. Moreover, the Config object also contains output options. You can find the full list of parameters in the online documentation.

## 7.4 Calculating and analyzing correlation functions

Now that we have created a Sample, and defined the simulation configuration parameters, we are ready to perform an actual calculation by calling the FORTRAN subroutines. The resulting correlation functions are automatically written to file.

The subsequent analysis of the correlation functions is done in Python. We can get the correlation functions directly from FORTRAN:

```
# DOS correlation, FORTRAN call
corr_DOS = tipsi.corr_DOS(sample, config)

# DOS correlation analysis
energies_DOS, DOS = tipsi.analyze_corr_DOS(config, corr_DOS)

# AC conductivity correlation, FORTRAN call
corr_AC = tipsi.corr_AC(sample, config)

# AC conductivity correlation analysis
omegas_AC, AC = tipsi.analyze_corr_AC(config, corr_AC)
```

Alternatively, we can read the correlation functions from file in a separate Python script:

```
ts = "1522172330" # set to output timestamp

# read Config object
config = tipsi.read_config("sim_data/" + ts + "config.pkl")

# get DOS
corr_DOS = tipsi.read_corr_DOS("sim_data/" + ts + "corr_DOS.dat")
energies_DOS, DOS = tipsi.analyze_corr_DOS(config, corr_DOS)
```

In the current version (0.9), the following quantities can be calculated:

- DOS
- LDOS
- quasi-eigenstates
- DC conductivity
- AC conductivity
- dynamical polarization and dielectric function

For more details on how to call each of these functions, and which configuration parameters to set to use them, we refer to the documentation.



# BIBLIOGRAPHY

- [1] H. Suzuura and T. Ando, “Phonons and electron-phonon scattering in carbon nanotubes,” *Phys. Rev. B*, vol. 65, p. 235412, May 2002.
- [2] G. Giuliani and G. Vignale, *Quantum theory of the electron liquid*. Cambridge University Press, 2005.
- [3] S. V. Vonsovsky and M. I. Katsnelson, *Quantum solid-state physics*. Springer-Verlag Berlin, Heidelberg, New York, 1989.
- [4] T. Westerhout, “Tools to calculate quantities related to plasmons in materials with no translational symmetry.” <https://github.com/twesterhout/plasmon-cpp>, 2017.
- [5] R. Landauer, “Spatial variation of currents and fields due to localized scatterers in metallic conduction,” *IBM Journal of Research and Development*, vol. 1, no. 3, pp. 223–231, 1957.
- [6] C. W. Groth, M. Wimmer, A. R. Akhmerov, and X. Waintal, “Kwant: a software package for quantum transport,” *New Journal of Physics*, vol. 16, no. 6, p. 063065, 2014.
- [7] S. Yuan, H. De Raedt, and M. I. Katsnelson, “Modeling electronic structure and transport properties of graphene with resonant scattering centers,” *Physical Review B*, vol. 82, no. 11, p. 115448, 2010.
- [8] A. Hams and H. De Raedt, “Fast algorithm for finding the eigenvalue distribution of very large matrices,” *Phys. Rev. E*, vol. 62, pp. 4365–4377, Sep 2000.
- [9] R. Kubo, “Statistical-mechanical theory of irreversible processes. i. general theory and simple applications to magnetic and conduction problems,” *Journal of the Physical Society of Japan*, vol. 12, no. 6, pp. 570–586, 1957.
- [10] A. Ishihara, *Statistical Physics*. Academic Press, New York, 1971.

- 
- [11] S. Yuan, R. Roldán, and M. I. Katsnelson, “Excitation spectrum and high-energy plasmons in single-layer and multilayer graphene,” *Physical Review B*, vol. 84, no. 3, p. 035439, 2011.
- [12] K. Novoselov, D. Jiang, F. Schedin, T. Booth, V. Khotkevich, S. Morozov, and A. Geim, “Two-dimensional atomic crystals,” *PNAS*, vol. 102, no. 30, pp. 10451–10453, 2005.
- [13] R. Roldán, L. Chirulli, E. Prada, J. A. Silva-Guillén, P. San-Jose, and F. Guinea, “Theory of 2d crystals: graphene and beyond,” *Chem. Soc. Rev.*, vol. 46, no. 15, pp. 4387–4399, 2017.
- [14] J. Yu, M. I. Katsnelson, and S. Yuan, “Tunable electronic and magneto-optical properties of monolayer arsenene from gw0 approximation to large-scale tight-binding simulations,” *Physical Review B*, vol. 98, p. 115117, 2018.
- [15] S. Zhang, S. Guo, Z. Chen, Y. Wang, H. Gao, J. Gómez-Herrero, P. Ares, F. Zamora, Z. Zhu, and H. Zeng, “Recent progress in 2d group-va semiconductors: from theory to experiment,” *Chem. Soc. Rev.*, vol. 47, pp. 982–1021, 2018.
- [16] S. Zhang, Z. Yan, Y. Li, Z. Chen, and H. Zeng, “Atomically thin arsenene and antimonene: semimetal–semiconductor and indirect–direct band-gap transitions,” *Angew. Chem., Int. Ed.*, vol. 127, no. 10, pp. 3155–3158, 2015.
- [17] J. Ji, X. Song, J. Liu, Z. Yan, C. Huo, S. Zhang, M. Su, L. Liao, W. Wang, Z. Ni, Y. Hao, and H. Zeng, “Two-dimensional antimonene single crystals grown by van der waals epitaxy,” *Nat. Commun.*, vol. 7, p. 13352, 2016.
- [18] P. Ares, F. Aguilar-Galindo, D. Rodríguez-San-Miguel, D. A. Aldave, S. Díaz-Tendero, M. Alcamí, F. Martín, J. Gómez-Herrero, and F. Zamora, “Mechanical isolation of highly stable antimonene under ambient conditions,” *Adv. Mater.*, vol. 28, no. 30, pp. 6332–6336, 2016.

- [19] C. Gibaja, D. Rodriguez-San-Miguel, P. Ares, J. Gómez-Herrero, M. Varela, R. Gillen, J. Maultzsch, F. Hauke, A. Hirsch, G. Abellán, and F. Zamora, “Few-layer antimonene by liquid-phase exfoliation,” *Angew. Chem., Int. Ed.*, vol. 55, no. 46, pp. 14345–14349, 2016.
- [20] X. Wu, Y. Shao, H. Liu, Z. Feng, Y.-L. Wang, J.-T. Sun, C. Liu, J.-O. Wang, Z.-L. Liu, S.-Y. Zhu, Y. Wang, S. Du, Y. Shi, K. Ibrahim, and H. Gao, “Epitaxial growth and air-stability of monolayer antimonene on pdte2,” *Adv. Mater.*, vol. 29, no. 11, 2017.
- [21] L. Lu, X. Tang, R. Cao, L. Wu, Z. Li, G. Jing, B. Dong, S. Lu, Y. Li, Y. Xiang, J. Li, D. Fan, and H. Zhang, “Broadband nonlinear optical response in few-layer antimonene and antimonene quantum dots: A promising optical kerr media with enhanced stability,” *Adv. Opt. Mater.*, vol. 5, no. 17, 2017.
- [22] G. Wang, R. Pandey, and S. P. Karna, “Atomically thin group v elemental films: theoretical investigations of antimonene allotropes,” *ACS Appl. Mater. Interfaces*, vol. 7, no. 21, pp. 11490–11496, 2015.
- [23] O. U. Aktürk, V. O. Özçelik, and S. Ciraci, “Single-layer crystalline phases of antimony: Antimonenes,” *Phys. Rev. B*, vol. 91, p. 235446, Jun 2015.
- [24] D. Singh, S. K. Gupta, Y. Sonvane, and I. Lukačević, “Antimonene: a monolayer material for ultraviolet optical nanodevices,” *Journal of Materials Chemistry C*, vol. 4, no. 26, pp. 6386–6390, 2016.
- [25] G. Pizzi, M. Gibertini, E. Dib, N. Marzari, G. Iannaccone, and G. Fiori, “Performance of arsenene and antimonene double-gate mosfets from first principles,” *Nat. Commun.*, vol. 7, p. 12585, 2016.
- [26] Y. Xu, B. Peng, H. Zhang, H. Shao, R. Zhang, and H. Zhu, “First-principle calculations of optical properties of monolayer arsenene and antimonene allotropes,” *Ann. Phys. (Berlin)*, vol. 529, p. 1600152, Apr. 2017.



- [27] A. Rudenko, M. Katsnelson, and R. Roldán, “Electronic properties of single-layer antimony: Tight-binding model, spin-orbit coupling, and the strength of effective coulomb interactions,” *Physical Review B*, vol. 95, no. 8, p. 081407, 2017.
- [28] Y. Wang, P. Huang, M. Ye, R. Quhe, Y. Pan, H. Zhang, H. Zhong, J. Shi, and J. Lu, “Many-body effect, carrier mobility, and device performance of hexagonal arsenene and antimonene,” *Chem. Mater.*, vol. 29, no. 5, pp. 2191–2201, 2017.
- [29] H. Guo, N. Lu, J. Dai, X. Wu, and X. C. Zeng, “Phosphorene nanoribbons, phosphorus nanotubes, and van der waals multilayers,” *J. Phys. Chem. C*, vol. 118, no. 25, pp. 14051–14059, 2014.
- [30] E. Taghizadeh Sisakht, M. H. Zare, and F. Fazileh, “Scaling laws of band gaps of phosphorene nanoribbons: A tight-binding calculation,” *Phys. Rev. B*, vol. 91, p. 085409, Feb 2015.
- [31] Y. Wang and Y. Ding, “Electronic structure and carrier mobilities of arsenene and antimonene nanoribbons: a first-principle study,” *Nanoscale Research Letters*, vol. 10, no. 1, p. 254, 2015.
- [32] M. M. Grujić, M. Ezawa, M. Z. Tadić, and F. M. Peeters, “Tunable skewed edges in puckered structures,” *Phys. Rev. B*, vol. 93, p. 245413, Jun 2016.
- [33] Y. Song, X. Wang, and W. Mi, “Spin splitting and electric field modulated electron-hole pockets in antimonene nanoribbons,” *npj Quantum Materials*, vol. 2, no. 1, p. 15, 2017.
- [34] H.-S. Tsai, C.-W. Chen, C.-H. Hsiao, H. Ouyang, and J.-H. Liang, “The advent of multilayer antimonene nanoribbons with room temperature orange light emission,” *Chem. Commun.*, vol. 52, no. 54, pp. 8409–8412, 2016.

- 
- [35] L. Brey and H. A. Fertig, “Electronic states of graphene nanoribbons studied with the dirac equation,” *Phys. Rev. B*, vol. 73, p. 235411, Jun 2006.
- [36] D. Gunlycke, J. Li, J. Mintmire, and C. White, “Altering low-bias transport in zigzag-edge graphene nanostrips with edge chemistry,” *Applied Physics Letters*, vol. 91, no. 11, p. 112108, 2007.
- [37] G. Kresse and J. Furthmüller, “Efficient iterative schemes for ab initio total-energy calculations using a plane-wave basis set,” *Physical review B*, vol. 54, no. 16, p. 11169, 1996.
- [38] G. Kresse and J. Furthmüller, “Efficiency of ab-initio total energy calculations for metals and semiconductors using a plane-wave basis set,” *Computational materials science*, vol. 6, no. 1, pp. 15–50, 1996.
- [39] P. E. Blöchl, “Projector augmented-wave method,” *Physical review B*, vol. 50, no. 24, p. 17953, 1994.
- [40] R. Roldán and A. Castellanos-Gomez, “Black phosphorus: A new bandgap tuning knob,” *Nat. Photon.*, vol. 11, no. 7, p. 407, 2017.
- [41] S. Yuan, E. van Veen, M. I. Katsnelson, and R. Roldán, “Quantum hall effect and semiconductor-to-semimetal transition in biased black phosphorus,” *Phys. Rev. B*, vol. 93, p. 245433, Jun 2016.
- [42] C. R. Ast, D. Pacilé, L. Moreschini, M. C. Falub, M. Papagno, K. Kern, M. Grioni, J. Henk, A. Ernst, S. Ostanin, and P. Bruno, “Spin-orbit split two-dimensional electron gas with tunable rashba and fermi energy,” *Phys. Rev. B*, vol. 77, p. 081407, Feb 2008.
- [43] V. Brosco, L. Benfatto, E. Cappelluti, and C. Grimaldi, “Unconventional dc transport in rashba electron gases,” *Phys. Rev. Lett.*, vol. 116, p. 166602, Apr 2016.
- [44] H. Rostami, R. Asgari, and F. Guinea, “Edge modes in zigzag and armchair ribbons of monolayer mos 2,” *J. Phys.: Condens. Matter*, vol. 28, no. 49, p. 495001, 2016.

- [45] P. Avouris, T. F. Heinz, and T. Low, eds., *2D Materials: Properties and Devices*. Cambridge University Press, 2017.
- [46] L. Li, Y. Yu, G. J. Ye, Q. Ge, X. Ou, H. Wu, D. Feng, X. H. Chen, and Y. Zhang, “Black phosphorus field-effect transistors,” *Nat. Nano.*, vol. 9, no. 5, pp. 372–377, 2014.
- [47] H. Liu, A. T. Neal, Z. Zhu, Z. Luo, X. Xu, D. Tománek, and P. D. Ye, “Phosphorene: an unexplored 2d semiconductor with a high hole mobility,” *ACS nano*, vol. 8, no. 4, pp. 4033–4041, 2014.
- [48] A. Castellanos-Gomez, L. Vicarelli, E. Prada, J. O. Island, K. L. Narasimha-Acharya, S. I. Blanter, D. J. Groenendijk, M. Buscema, G. A. Steele, J. V. Alvarez, H. W. Zandbergen, J. J. Palacios, and H. S. J. van der Zant, “Isolation and characterization of few-layer black phosphorus,” *2D Mater.*, vol. 1, no. 2, p. 025001, 2014.
- [49] F. Xia, H. Wang, and Y. Jia, “Rediscovering black phosphorus as an anisotropic layered material for optoelectronics and electronics,” *Nat. Comm.*, vol. 5, p. 4458, 2014.
- [50] C. Lin, R. Grassi, T. Low, and A. S. Helmy, “Multilayer black phosphorus as a versatile mid-infrared electro-optic material,” *Nano letters*, vol. 16, no. 3, pp. 1683–1689, 2016.
- [51] R. Peng, K. Khaliji, N. Youngblood, R. Grassi, T. Low, and M. Li, “Midinfrared electro-optic modulation in few-layer black phosphorus,” *Nano letters*, vol. 17, no. 10, pp. 6315–6320, 2017.
- [52] W. S. Whitney, M. C. Sherrott, D. Jariwala, W.-H. Lin, H. A. Bechtel, G. R. Rossman, and H. A. Atwater, “Field effect optoelectronic modulation of quantum-confined carriers in black phosphorus,” *Nano letters*, vol. 17, no. 1, pp. 78–84, 2016.
- [53] B. Deng, V. Tran, Y. Xie, H. Jiang, C. Li, Q. Guo, X. Wang, H. Tian, S. J. Koester, H. Wang, J. J. Cha, Q. Xia, L. Yang, and F. Xia,

- “Efficient electrical control of thin-film black phosphorus bandgap,” *Nat. Comm.*, vol. 8, p. 14474, 2017.
- [54] Y. Liu, Z. Qiu, A. Carvalho, Y. Bao, H. Xu, S. J. Tan, W. Liu, A. Castro Neto, K. P. Loh, and J. Lu, “Gate-tunable giant stark effect in few-layer black phosphorus,” *Nano Lett.*, vol. 17, no. 3, pp. 1970–1977, 2017.
- [55] J. Kim, S. S. Baik, S. H. Ryu, Y. Sohn, S. Park, B.-G. Park, J. Denlinger, Y. Yi, H. J. Choi, and K. S. Kim, “Observation of tunable band gap and anisotropic dirac semimetal state in black phosphorus,” *Science*, vol. 349, no. 6249, pp. 723–726, 2015.
- [56] J. Yang, R. Xu, J. Pei, Y. W. Myint, F. Wang, Z. Wang, S. Zhang, Z. Yu, and Y. Lu, “Optical tuning of exciton and trion emissions in monolayer phosphorene,” *Light Sci. Appl.*, vol. 4, no. 7, p. e312, 2015.
- [57] J. Quereda, P. San-Jose, V. Parente, L. Vaquero-Garzon, A. J. Molina-Mendoza, N. Agraït, G. Rubio-Bollinger, F. Guinea, R. Roldán, and A. Castellanos-Gomez, “Strong modulation of optical properties in black phosphorus through strain-engineered rippling,” *Nano letters*, vol. 16, no. 5, pp. 2931–2937, 2016.
- [58] A. S. Rodin, A. Carvalho, and A. H. Castro Neto, “Strain-induced gap modification in black phosphorus,” *Phys. Rev. Lett.*, vol. 112, p. 176801, May 2014.
- [59] Z. J. Xiang, G. J. Ye, C. Shang, B. Lei, N. Z. Wang, K. S. Yang, D. Y. Liu, F. B. Meng, X. G. Luo, L. J. Zou, Z. Sun, Y. Zhang, and X. H. Chen, “Pressure-induced electronic transition in black phosphorus,” *Phys. Rev. Lett.*, vol. 115, p. 186403, Oct 2015.
- [60] T. Low, A. Chaves, J. Caldwell, A. Kumar, N. Fang, P. Avouris, T. Heinz, F. Guinea, L. Martin-Moreno, and F. Koppens, “Polaritons in layered two-dimensional materials,” *Nat. Mater.*, vol. 16, no. 2, pp. 182–194, 2017.

- 
- [61] R. W. Keyes, “The electrical properties of black phosphorus,” *Physical Review*, vol. 92, no. 3, p. 580, 1953.
- [62] A. Poddubny, I. Iorsh, P. Belov, and Y. Kivshar, “Hyperbolic metamaterials,” *Nat. Photon.*, vol. 7, no. 12, pp. 948–957, 2013.
- [63] O. Yermakov, A. Ovcharenko, M. Song, A. Bogdanov, I. Iorsh, and Y. S. Kivshar, “Hybrid waves localized at hyperbolic metasurfaces,” *Physical Review B*, vol. 91, no. 23, p. 235423, 2015.
- [64] J. S. Gomez-Diaz, M. Tymchenko, and A. Alu, “Hyperbolic plasmons and topological transitions over uniaxial metasurfaces,” *Physical review letters*, vol. 114, no. 23, p. 233901, 2015.
- [65] A. Nemilentsau, T. Low, and G. Hanson, “Anisotropic 2d materials for tunable hyperbolic plasmonics,” *Phys. Rev. Lett.*, vol. 116, p. 066804, Feb 2016.
- [66] Y. Yermakov, A. A. Hurshkainen, D. A. Dobrykh, P. V. Kapitanova, I. V. Iorsh, S. B. Glybovski, and A. A. Bogdanov, “Experimental observation of hybrid te-tm polarized surface waves supported by a hyperbolic metasurface,” *Physical Review B*, vol. 98, no. 19, p. 195404, 2018.
- [67] W. Ma, P. Alonso-González, S. Li, A. Y. Nikitin, J. Yuan, J. Martín-Sánchez, J. Taboada-Gutiérrez, I. Amenabar, P. Li, S. Vélez, *et al.*, “In-plane anisotropic and ultra-low-loss polaritons in a natural van der waals crystal,” *Nature*, vol. 562, no. 7728, p. 557, 2018.
- [68] Z. Zheng, N. Xu, S. L. Oscurato, M. Tamagnone, F. Sun, Y. Jiang, Y. Ke, J. Chen, W. Huang, W. L. Wilson, *et al.*, “A mid-infrared biaxial hyperbolic van der waals crystal,” *arXiv preprint arXiv:1809.03432*, 2018.
- [69] D. Correas-Serrano, J. Gomez-Diaz, A. A. Melcon, and A. Alù, “Black phosphorus plasmonics: anisotropic elliptical propagation and

- nonlocality-induced canalization,” *J. Opt.*, vol. 18, no. 10, p. 104006, 2016.
- [70] J. Shang, C. Cong, Z. Wang, N. Peimyoo, L. Wu, C. Zou, Y. Chen, X. Y. Chin, J. Wang, C. Soci, *et al.*, “Room-temperature 2d semiconductor activated vertical-cavity surface-emitting lasers,” *Nature communications*, vol. 8, no. 1, p. 543, 2017.
- [71] S. Wu, S. Buckley, J. R. Schaibley, L. Feng, J. Yan, D. G. Mandrus, F. Hatami, W. Yao, J. Vučković, A. Majumdar, *et al.*, “Monolayer semiconductor nanocavity lasers with ultralow thresholds,” *Nature*, vol. 520, no. 7545, p. 69, 2015.
- [72] A. N. Rudenko and M. I. Katsnelson, “Quasiparticle band structure and tight-binding model for single-and bilayer black phosphorus,” *Physical Review B*, vol. 89, no. 20, p. 201408, 2014.
- [73] A. Rudenko, S. Yuan, and M. Katsnelson, “Toward a realistic description of multilayer black phosphorus: From g w approximation to large-scale tight-binding simulations,” *Physical Review B*, vol. 92, no. 8, p. 085419, 2015.
- [74] P. San-Jose, V. Parente, F. Guinea, R. Roldán, and E. Prada, “Inverse funnel effect of excitons in strained black phosphorus,” *Physical Review X*, vol. 6, no. 3, p. 031046, 2016.
- [75] Q. Wei and X. Peng, “Superior mechanical flexibility of phosphorene and few-layer black phosphorus,” *Appl. Phys. Lett.*, vol. 104, no. 25, p. 251915, 2014.
- [76] T. Low, P.-Y. Chen, and D. Basov, “Superluminal plasmons with resonant gain in population inverted bilayer graphene,” *Physical Review B*, vol. 98, no. 4, p. 041403, 2018.
- [77] A. F. Page, F. Ballout, O. Hess, and J. M. Hamm, “Nonequilibrium plasmons with gain in graphene,” *Physical Review B*, vol. 91, no. 7, p. 075404, 2015.

- 
- [78] T. Low, A. S. Rodin, A. Carvalho, Y. Jiang, H. Wang, F. Xia, and A. H. Castro Neto, “Tunable optical properties of multilayer black phosphorus thin films,” *Phys. Rev. B*, vol. 90, p. 075434, Aug 2014.
- [79] G. Zhang, S. Huang, A. Chaves, C. Song, V. O. Özçelik, T. Low, and H. Yan, “Infrared fingerprints of few-layer black phosphorus,” *Nature communications*, vol. 8, p. 14071, 2017.
- [80] G. Ni, L. Wang, M. Goldflam, M. Wagner, Z. Fei, A. McLeod, M. Liu, F. Keilmann, B. Özyilmaz, A. C. Neto, *et al.*, “Ultrafast optical switching of infrared plasmon polaritons in high-mobility graphene,” *Nature Photonics*, vol. 10, no. 4, p. 244, 2016.
- [81] C. H. Lui, K. F. Mak, J. Shan, T. F. Heinz, *et al.*, “Ultrafast photoluminescence from graphene,” *Physical review letters*, vol. 105, no. 12, p. 127404, 2010.
- [82] M. Polini, F. Guinea, M. Lewenstein, H. Manoharan, and V. Pellegrini, “Artificial honeycomb lattices for electrons, atoms and photons,” *Nature Nanotech.*, vol. 8, no. 9, pp. 625–633, 2013.
- [83] A. Singha, M. Gibertini, B. Karmakar, S. Yuan, M. Polini, G. Vignale, M. Katsnelson, A. Pinczuk, L. Pfeiffer, K. West, *et al.*, “Two-dimensional mott-hubbard electrons in an artificial honeycomb lattice,” *Science*, vol. 332, no. 6034, pp. 1176–1179, 2011.
- [84] K. K. Gomes, W. Mar, W. Ko, F. Guinea, and H. C. Manoharan, “Designer dirac fermions and topological phases in molecular graphene,” *Nature*, vol. 483, no. 7389, p. 306, 2012.
- [85] M. C. Rechtsman, J. M. Zeuner, Y. Plotnik, Y. Lumer, D. Podolsky, F. Dreisow, S. Nolte, M. Segev, and A. Szameit, “Photonic floquet topological insulators,” *Nature*, vol. 496, no. 7444, p. 196, 2013.
- [86] G. Jotzu, M. Messer, R. Desbuquois, M. Lebrat, T. Uehlinger, D. Greif, and T. Esslinger, “Experimental realization of the topo-

- logical haldane model with ultracold fermions,” *Nature*, vol. 515, no. 7526, p. 237, 2014.
- [87] F. D. M. Haldane, “Model for a quantum hall effect without landau levels: Condensed-matter realization of the” parity anomaly”,” *Physical Review Letters*, vol. 61, no. 18, p. 2015, 1988.
- [88] M. Gibertini, A. Singha, V. Pellegrini, M. Polini, G. Vignale, A. Pinczuk, L. N. Pfeiffer, and K. W. West, “Engineering artificial graphene in a two-dimensional electron gas,” *Physical Review B*, vol. 79, no. 24, p. 241406, 2009.
- [89] G. De Simoni, A. Singha, M. Gibertini, B. Karmakar, M. Polini, V. Piazza, L. Pfeiffer, K. West, F. Beltram, and V. Pellegrini, “Delocalized-localized transition in a semiconductor two-dimensional honeycomb lattice,” *Applied Physics Letters*, vol. 97, no. 13, p. 132113, 2010.
- [90] C.-H. Park and S. G. Louie, “Making massless dirac fermions from a patterned two-dimensional electron gas,” *Nano letters*, vol. 9, no. 5, pp. 1793–1797, 2009.
- [91] E. Räsänen, C. Rozzi, S. Pittalis, and G. Vignale, “Electron-electron interactions in artificial graphene,” *Physical review letters*, vol. 108, no. 24, p. 246803, 2012.
- [92] L. Nadvornik, M. Orlita, N. Goncharuk, L. Smrčka, V. Novák, V. Jurka, K. Hruška, Z. Vybourný, Z. Wasilewski, M. Potemski, *et al.*, “From laterally modulated two-dimensional electron gas towards artificial graphene,” *New Journal of Physics*, vol. 14, no. 5, p. 053002, 2012.
- [93] S. Goswami, M. Aamir, C. Siegert, M. Pepper, I. Farrer, D. A. Ritchie, and A. Ghosh, “Transport through an electrostatically defined quantum dot lattice in a two-dimensional electron gas,” *Physical Review B*, vol. 85, no. 7, p. 075427, 2012.



- [94] D. Scarabelli, S. Wang, A. Pinczuk, S. J. Wind, Y. Y. Kuznetsova, L. N. Pfeiffer, K. West, G. C. Gardner, M. J. Manfra, and V. Pellegrini, "Fabrication of artificial graphene in a gaas quantum heterostructure," *Journal of Vacuum Science & Technology B, Nanotechnology and Microelectronics: Materials, Processing, Measurement, and Phenomena*, vol. 33, no. 6, p. 06FG03, 2015.
- [95] S. Kempkes, M. Slot, S. Freeney, S. Zevenhuizen, D. Vanmaekelbergh, I. Swart, and C. M. Smith, "Design and characterization of electrons in a fractal geometry," *Nature Physics*, p. 1, 2018.
- [96] W. H. Evers, B. Goris, S. Bals, M. Casavola, J. de Graaf, R. van Roij, M. Dijkstra, and D. Vanmaekelbergh, "Low-dimensional semiconductor superlattices formed by geometric control over nanocrystal attachment," *Nano letters*, vol. 13, no. 6, pp. 2317–2323, 2012.
- [97] Y.-C. Chen, T. Cao, C. Chen, Z. Pedramrazi, D. Haberer, D. G. De Oteyza, F. R. Fischer, S. G. Louie, and M. F. Crommie, "Molecular bandgap engineering of bottom-up synthesized graphene nanoribbon heterojunctions," *Nature nanotechnology*, vol. 10, no. 2, p. 156, 2015.
- [98] J. Shang, Y. Wang, M. Chen, J. Dai, X. Zhou, J. Kuttner, G. Hilt, X. Shao, J. Gottfried, and K. Wu, "Assembling molecular sierpiński triangle fractals," *Nature Chem.*, vol. 7, no. 5, pp. 389–393, 2015.
- [99] K. J. Falconer, *The geometry of fractal sets*, vol. 85. Cambridge university press, 1986.
- [100] B. Mandelbrot, *The fractal geometry of nature*. W.H. Freeman and Co., New York, 1983.
- [101] R. Ketzmerick, "Fractal conductance fluctuations in generic chaotic cavities," *Physical Review B*, vol. 54, no. 15, p. 10841, 1996.
- [102] A. Sachrajda, R. Ketzmerick, C. Gould, Y. Feng, P. Kelly, A. Delage, and Z. Wasilewski, "Fractal conductance fluctuations in a soft-wall

- stadium and a sinai billiard,” *Physical review letters*, vol. 80, no. 9, p. 1948, 1998.
- [103] I. Guarneri and M. Terraneo, “Fractal fluctuations in quantum integrable scattering,” *Physical Review E*, vol. 65, no. 1, p. 015203, 2001.
- [104] R. Taylor, R. Newbury, A. Micolich, M. Fromhold, H. Linke, G. Davies, T. Martin, and C. Marlow, “A review of fractal conductance fluctuations in ballistic semiconductor devices,” in *Electron Transport in Quantum Dots*, pp. 277–316, Springer, 2003.
- [105] V. Kotimäki, E. Räsänen, H. Hennig, and E. J. Heller, “Fractal dynamics in chaotic quantum transport,” *Physical Review E*, vol. 88, no. 2, p. 022913, 2013.
- [106] S. Havlin and D. Ben-Avraham, “Diffusion in disordered media,” *Advances in Physics*, vol. 36, no. 6, pp. 695–798, 1987.
- [107] M. B. Isichenko, “Percolation, statistical topography, and transport in random media,” *Reviews of modern physics*, vol. 64, no. 4, p. 961, 1992.
- [108] S. Kusuoka, “Lecture on diffusion processes on nested fractals,” in *Statistical mechanics and fractals*, pp. 39–98, Springer, 1993.
- [109] A. Chakrabarti, “Exact results for infinite and finite sierpinski gasket fractals: extended electron states and transmission properties,” *Journal of Physics: Condensed Matter*, vol. 8, no. 50, p. 10951, 1996.
- [110] C. Groth, J. Tworzydło, and C. Beenakker, “Electronic shot noise in fractal conductors,” *Physical review letters*, vol. 100, no. 17, p. 176804, 2008.
- [111] Y. Liu, Z. Hou, P. Hui, and W. Sritrakool, “Electronic transport properties of sierpinski lattices,” *Phys. Rev. B*, vol. 60, pp. 13444–13452, Nov 1999.

- 
- [112] Z. Lin, Y. Cao, Y. Liu, and P. Hui, “Electronic transport properties of sierpinski lattices in a magnetic field,” *Physical Review B*, vol. 66, no. 4, p. 045311, 2002.
- [113] S. Jana, A. Chakrabarti, and S. Chattopadhyay, “Electronic transport in an anisotropic sierpinski gasket,” *Physica B: Condensed Matter*, vol. 405, no. 17, pp. 3735–3740, 2010.
- [114] Z.-G. Song, Y.-Y. Zhang, and S.-S. Li, “The topological insulator in a fractal space,” *Applied Physics Letters*, vol. 104, no. 23, p. 233106, 2014.
- [115] D. R. Hofstadter, “Energy levels and wave functions of bloch electrons in rational and irrational magnetic fields,” *Physical review B*, vol. 14, no. 6, p. 2239, 1976.
- [116] R. Rammal and G. Toulouse, “Spectrum of the schrödinger equation on a self-similar structure,” *Physical review letters*, vol. 49, no. 16, p. 1194, 1982.
- [117] E. Domany, S. Alexander, D. Bensimon, and L. P. Kadanoff, “Solutions to the schrödinger equation on some fractal lattices,” *Physical Review B*, vol. 28, no. 6, p. 3110, 1983.
- [118] R. Rammal, “Nature of eigenstates on fractal structures,” *Physical Review B*, vol. 28, no. 8, p. 4871, 1983.
- [119] X. R. Wang, “Localization in fractal spaces: exact results on the sierpinski gasket,” *Physical Review B*, vol. 51, no. 14, p. 9310, 1995.
- [120] A. Hernando, M. Sulc, and J. Vanicek, “Spectral properties of electrons in fractal nanowires,” *arXiv preprint arXiv:1503.07741*, 2015.
- [121] T. Vicsek, “Fractal models for diffusion controlled aggregation,” *Journal of Physics A: Mathematical and General*, vol. 16, no. 17, p. L647, 1983.

- 
- [122] T. G. Pedersen, C. Flindt, J. Pedersen, N. A. Mortensen, A.-P. Jauho, and K. Pedersen, “Graphene antidot lattices: designed defects and spin qubits,” *Physical Review Letters*, vol. 100, no. 13, p. 136804, 2008.
- [123] Y. Gefen, A. Aharony, and B. B. Mandelbrot, “Phase transitions on fractals. iii. infinitely ramified lattices,” *Journal of Physics A: Mathematical and General*, vol. 17, no. 6, p. 1277, 1984.
- [124] P. Nozieres and D. Pines, *The Theory of Quantum Liquids (Advanced Book Classics)*. Perseus Books, LLC, 1999.
- [125] P. M. Platzman and P. A. Wolff, *Waves and interactions in solid state plasmas*, vol. 13. Academic Press New York, 1973.
- [126] J. A. Scholl, A. L. Koh, and J. A. Dionne, “Quantum plasmon resonances of individual metallic nanoparticles,” *Nature*, vol. 483, no. 7390, p. 421, 2012.
- [127] M. S. Tame, K. McEnery, Ş. Özdemir, J. Lee, S. Maier, and M. Kim, “Quantum plasmonics,” *Nature Physics*, vol. 9, no. 6, p. 329, 2013.
- [128] C. L. Haynes, C. R. Yonzon, X. Zhang, and R. P. Van Duyne, “Surface-enhanced raman sensors: early history and the development of sensors for quantitative biowarfare agent and glucose detection,” *Journal of Raman Spectroscopy: An International Journal for Original Work in all Aspects of Raman Spectroscopy, Including Higher Order Processes, and also Brillouin and Rayleigh Scattering*, vol. 36, no. 6-7, pp. 471–484, 2005.
- [129] A. C. Pipino, G. C. Schatz, and R. P. Van Duyne, “Surface-enhanced second-harmonic diffraction: selective enhancement by spatial harmonics,” *Physical Review B*, vol. 49, no. 12, p. 8320, 1994.
- [130] C. R. Yonzon, D. A. Stuart, X. Zhang, A. D. McFarland, C. L. Haynes, and R. P. Van Duyne, “Towards advanced chemical and bio-

- logical nanosensorsan overview,” *Talanta*, vol. 67, no. 3, pp. 438–448, 2005.
- [131] W. Srituravanich, N. Fang, C. Sun, Q. Luo, and X. Zhang, “Plasmonic nanolithography,” *Nano letters*, vol. 4, no. 6, pp. 1085–1088, 2004.
- [132] M. L. Brongersma and P. G. Kik, *Surface plasmon nanophotonics*, vol. 131. Springer, 2007.
- [133] I. Torre, M. I. Katsnelson, A. Diaspro, V. Pellegrini, and M. Polini, “Lippmann-schwinger theory for two-dimensional plasmon scattering,” *Physical Review B*, vol. 96, no. 3, p. 035433, 2017.
- [134] F. Bloch, “Bremsvermögen von atomen mit mehreren elektronen,” *Zeitschrift für Physik A Hadrons and Nuclei*, vol. 81, no. 5, pp. 363–376, 1933.
- [135] H. Jensen, “Eigenschwingungen eines fermi-gases und anwendung auf die blochsche bremsformel für schnelle teilchen,” *Zeitschrift für Physik*, vol. 106, no. 9-10, pp. 620–632, 1937.
- [136] B. K. Ishmukhametov, “Bk ishmukhametov, phys. status solidi (b) 45, 669 (1971).,” *Phys. Status Solidi (b)*, vol. 45, p. 669, 1971.
- [137] A. Sen, “Spectrum of plasma oscillations in atoms,” *Lettere al Nuovo Cimento (1971-1985)*, vol. 8, no. 12, pp. 749–752, 1973.
- [138] G. Gadiyak, A. Kirzhnits, and E. Lozovik, “Collective excitations of a heavy atom,” *Zh. Eksp. Teor. Fiz.*, vol. 69, pp. 122–130, 1975.
- [139] B. Ishmukhametov and M. Katsnelson, “Collective oscillations of an inhomogeneous electron plasma in the quasi-classical approximation,” *Fiz. Met. Metalloved.*, vol. 40, no. 4, pp. 736–742, 1975.
- [140] M. Y. Amusia and V. Ivanov, “On the existence of a collective level in the xe-atom,” *Physics Letters A*, vol. 65, no. 3, pp. 217–219, 1978.

- 
- [141] E. Verkhovtseva, P. Pogrebnyak, and Y. M. Fogel, “Concerning the possibility of radiative decay of the collective levels of the argon atom,” *JETP LETTERS*, vol. 24, no. 8, pp. 425–428, 1976.
- [142] B. K. Ishmukhametov, V. Larionov, M. Katsnelson, and A. Ustjuzhanin, “On the existence of the atomic plasmon,” *Physics Letters. A*, vol. 82, no. 8, pp. 387–388, 1981.
- [143] W. Wang, T. Christensen, A.-P. Jauho, K. S. Thygesen, M. Wubs, and N. A. Mortensen, “Plasmonic eigenmodes in individual and bow-tie graphene nanotriangles,” *Scientific reports*, vol. 5, p. 9535, 2015.
- [144] J. Lu, K. P. Loh, H. Huang, W. Chen, and A. T. Wee, “Plasmon dispersion on epitaxial graphene studied using high-resolution electron energy-loss spectroscopy,” *Physical Review B*, vol. 80, no. 11, p. 113410, 2009.
- [145] K. Andersen, K. W. Jacobsen, and K. S. Thygesen, “Spatially resolved quantum plasmon modes in metallic nano-films from first-principles,” *Physical Review B*, vol. 86, no. 24, p. 245129, 2012.
- [146] F. Jin, R. Roldán, M. I. Katsnelson, and S. Yuan, “Screening and plasmons in pure and disordered single-and bilayer black phosphorus,” *Physical Review B*, vol. 92, no. 11, p. 115440, 2015.
- [147] E. Cappelluti, R. Roldán, J. Silva-Guillén, P. Ordejón, and F. Guinea, “Tight-binding model and direct-gap/indirect-gap transition in single-layer and multilayer mos 2,” *Physical Review B*, vol. 88, no. 7, p. 075409, 2013.



# SUMMARY

Two-dimensional materials have many possible applications in electronics and optics. To further explore these possibilities we need to do realistic modelling of large-scale two-dimensional systems. However, this is difficult with *ab initio* methods.

The tight-binding approximation provides a simple and intuitive way to model large-scale two-dimensional condensed matter systems. It also allows for the introduction of different types of external fields and disorder. We can study electronic, transport and optical properties using exact diagonalization of the Hamiltonian. When the number of atoms in the model becomes so large that exact diagonalization is no longer an option, we can use the tight-binding propagation method to calculate these properties. In chapter 2 we saw how exactly to do these computations.

In chapter 3 we saw a simple application of the tight-binding method: antimonene ribbons under bias. It turns out that we can move around the electronic bands of the system, by applying an electric field. An out-of-plane field increases the gap, and an in-plane electric field decreases the gap and causes band splitting.

Then we moved on to black phosphorus. In chapter 4, we studied the optical properties of this material, and showed how its hyperbolic spectrum can be tuned by applying strain and bias. Moreover, we showed that optical gain introduces a new hyperbolic region to the material.

In chapters 5 and 6 we studied fractal systems. These are systems that are self-similar, i.e., they exhibit patterns that repeat on different length scales.

We showed that the conductance of fractals in the Sierpinski carpet family is self-similar, just like the sample itself. Moreover, the box-counting dimension of this graph is approximately equal to the Hausdorff dimension of the sample, suggesting a relation between them. For other, less connected fractals, this is not the case.

Then, we investigated the optical and plasmonic properties of Sierpinski carpets and gaskets. We learned that the optical conductivity shows peaks



corresponding to each length scale present in the sample, as a result of the overlap of eigenstates at each of those scales. Moreover, we showed that the Sierpinski gasket features localized plasmon modes. This type of plasmon confinement could be interesting for light manipulation at the atomic level.

Finally, in the appendix we introduced Tipsi: a tight-binding propagation simulator for Python. With this library it is easy to make a large-scale Hamiltonian and apply the tight-binding propagation method to it.

# SAMENVATTING

Tweedimensionale materialen hebben vele mogelijke toepassingen in elektronica en optica. Om deze mogelijkheden verder te verkennen moeten we realistische modellen van grootschalige tweedimensionale systemen doorrekenen. Dit is echter lastig met *ab initio* methoden.

De tight-binding benadering geeft ons een simpele en intuïtieve manier om deze grootschalige vastestofmodellen te maken. Met deze benadering kunnen we bovendien verschillende soorten externe velden en wanorde aanbrengen. We kunnen de elektronische en optische eigenschappen van materialen bestuderen door middel van diagonalisatie van de Hamiltoniaan. Wanneer het aantal atomen in het model echter zo groot wordt dat diagonalisatie geen optie is, kunnen we de tight-binding propagatiemethode gebruiken. In hoofdstuk 2 zagen we hoe je zulke berekeningen precies uitvoert.

In hoofdstuk 3 zagen we een simpele toepassing van de tight-binding methode: antimoneen-nanoribbons met bias. Het blijkt dat we de elektronische bandstructuur van het systeem kunnen aanpassen door een elektrisch veld toe te passen. Een veld haaks op het materiaal maakt de band gap groter, en een veld in transversale richting maakt de band gap groter en veroorzaakt band splitting.

Daarna zijn we overgestapt naar fosforeen. In hoofdstuk 4 hebben we de optische eigenschappen van dit materiaal bestudeerd, en kwamen we erachter dat het hyperbolische spectrum kan worden aangepast door het materiaal uit te rekken en een elektrisch veld toe te passen. Daarnaast kunnen we een nieuwe hyperbolische regio introduceren door optische gain te gebruiken.

In hoofdstukken 5 en 6 hebben we fractale systemen bekeken. Dit zijn systemen die zelfgelijkvormig zijn. In andere woorden, het materiaal vertoont patronen die gelijk zijn op verschillende lengteschalen.

We hebben laten zien dat de geleidbaarheid van het tapijt van Sierpinski zelfgelijkvormig is, net zoals de geometrie van het systeem zelf. Daarbij is de box-counting dimensie van de geleidbaarheid ongeveer gelijk aan de

Hausdorff-dimensie van het sample, wat een relatie tussen deze twee suggereert. Voor andere, minder verbonden fractals is dit niet het geval.

Daarna hebben we de optische en plasmonische eigenschappen van tapijten en driehoeken van Sierpinski onderzocht. We hebben daar geleerd dat het optische spectrum pieken vertoont die overeenkomen met de lengteschalen in het systeem, tengevolge van de overlap tussen eigentstanden op die schalen. Daarnaast hebben we laten zien dat de driehoek van Sierpinski gelocaliseerde plasmon-modes heeft. Dat type confinement kan interessant zijn voor de manipulatie van licht op atomische schaal.

Ten slotte hebben we Tpsi geïntroduceerd: een Python library voor tight-binding propagatie. Hiermee is het gemakkelijk om grootschalige tight-binding Hamiltonianen te maken en daarop de propagatiemethode toe te passen.

# PUBLICATIONS

- B. Schuler, J.H. Lee, C. Kastl, K.A. Cochrane, C.T. Chen, S. Refaely-Abramson, S. Yuan, E. van Veen, R. Roldán, N.J. Borys, R.J. Koch, S. Aloni, A.M. Schwartzberg, D.F. Ogletree, J.B. Neaton, A. Weber-Bargioni, “How Substitutional Point Defects in Two-Dimensional WS<sub>2</sub> Induce Charge Localization, Spin-Orbit Splitting, and Strain” *ACS nano* (2019)
- H. Shi, Z. Zhan, Z. Qi, K. Huang, E. van Veen, J.A. Silva Guillén, R. Zhang, P. Li, K. Xie, H. Ji, M.I. Katsnelson, S. Yuan, S. Qin, Z. Zhang, “Large-area, periodic, and tunable pseudo-magnetic fields in low-angle twisted bilayer graphene,” *arXiv:1905.04515* (2019)
- E. van Veen, A. Nemilentsau, A. Kumar, R. Roldán, M.I. Katsnelson, T. Low, S. Yuan, “Tuning Two-Dimensional Hyperbolic Plasmons in Black Phosphorus,” *Physical Review Applied* 12(1), 014011 (2019)
- G. Slotman, A. Rudenko, E. van Veen, M.I. Katsnelson, R. Roldán, S. Yuan, “Plasmon spectrum of single-layer antimonene,” *Physical Review B* 98, 155411 (2018)
- E. van Veen, J. Yu, M.I. Katsnelson, R. Roldán, S. Yuan, “Electronic structure of monolayer antimonene nanoribbons under out-of-plane and transverse bias,” *Physical Review Materials* 2, 114011 (2018)
- G. Nicotra, E. van Veen, I. Deretzis, L. Wang, J. Hu, Z. Mao, V. Fabio, C. Spinella, G. Chiarello, A. Rudenko, S. Yuan, A. Politano, “Anisotropic ultraviolet-plasmon dispersion in black phosphorus,” *Nanoscale* (2018)
- J. Yu, E. van Veen, M.I. Katsnelson, S. Yuan, “Effective lattice Hamiltonian for monolayer tin disulfide: Tailoring electronic structure with electric and magnetic fields,” *Physical Review B* 97, 245410 (2018)

- T. Westerhout, E. van Veen, M.I. Katsnelson, S. Yuan, “Plasmon confinement in fractal quantum systems,” *Physical Review B* 97, 205434 (2018)
- E. van Veen, A. Tomadin, M. Polini, M.I. Katsnelson, S. Yuan, “Optical conductivity of a quantum electron gas in a Sierpinski carpet,” *Physical Review B* 96, 235438 (2017)
- J. Yu, L. Qu, E. van Veen, M.I. Katsnelson, S. Yuan, “Hyperhoneycomb boron nitride with anisotropic mechanical, electronic, and optical properties,” *Physical Review Materials* 1, 045001 (2017)
- S. Yuan, E. van Veen, M.I. Katsnelson, R. Roldán, “Quantum Hall effect and semiconductor-to-semimetal transition in biased black phosphorus,” *Physical Review B* 93, 245433 (2016)
- E. van Veen, S. Yuan, M.I. Katsnelson, M. Polini, A. Tomadin, “Quantum transport in Sierpinski carpets,” *Physical Review B* 93, 115428 (2016)

# CURRICULUM VITAE

Edo was born on 20 February 1990 in Eindhoven. He grew up in Waalre and attended gymnasium at the Christiaan Huygens College in Eindhoven. From 2008 to 2014 he studied physics at the Radboud University in Nijmegen. During that period he served as board member of the physics study association for two years. He did his master's internship on the history and philosophy of quantum physics at the University of Sydney. In 2014 he started his work as a doctoral student at the Theory of Condensed Matter group, under the supervision of Mikhail Katsnelson and Shengjun Yuan.



# ACKNOWLEDGEMENTS

This thesis is the result of four years of collaborative effort, for which I have a lot of people to thank.

Firstly I would like to thank my promotors Mikhail Katsnelson and Shengjun Yuan. Misha, thank you for the opportunity to do this work, for the scientific guidance, and for the interesting discussions on movies and TV shows at the coffee breaks. Shengjun, thank you for your commitment as my daily supervisor, the many discussions we had about physics and programming, and for the great time in China.

To Marco Polini and Andrea Tomadin, many thanks for our nice collaboration on fractal quantum systems. I thoroughly enjoyed visiting Pisa and working with you. Also many thanks to Rafael Roldán and Tony Low for our work together.

I had an amazing time at the TCM group in Nijmegen. Hylke, you were a great roomie. Robert and Marion, thanks for the dinners. Lennert and Guus, thanks for all the Seinfeld jokes. Tom, you were the best bachelor student ever and you basically supervised yourself. Erik, Koen, Linde, Merel, Jaap, Andrea, Andrey, Ivan, Zhenya, Clement, Allesandro, Peiliang, Jin, Achille and Belinda, thanks for making the department a great place to work.

I would also like to thank all the people at the computational physics group in Wuhan. Zewen, Guodong, Zhen, Hongxia, Sasha, José, Kaixiang and Kiki, thank you for all the badminton games and jianzi sessions.

And of course, there is life outside academia. Nick and Iris, thanks for making me feel at home in Utrecht. Bram and Lennart, thanks for all the games and movies. Gabe and Joshua, thanks for all the music. Pierre, thanks for all the wine and cheese.

Finally, I want to thank my parents and sisters for giving me all their support. And of course Wen, for always being there for me.